Winter 1995

Seasonal Variability of Heat and Mass Transport Process in the Upper Tropical Atlantic Ocean: A Numerical Model Study

Sang-Ki Lee
Old Dominion University

SEASONAL VARIABILITY OF HEAT AND MASS TRANSPORT PROCESS IN THE UPPER TROPICAL ATLANTIC OCEAN: A NUMERICAL MODEL STUDY

by

Sang-Ki Lee

Master of Science, December 1993
Old Dominion University, Norfolk, Virginia, USA.
Bachelor of Science, February 1991
Inha University, Incheon, Republic of Korea

A Dissertation submitted to the Faculty of
Old Dominion University in Partial Fulfillment of the
Requirements for the Degree of

Doctor of Philosophy

Oceanography

Old Dominion University
December, 1995

Approved by:

Dr. Gabriel T. Csanady (chairman)

Dr. Chester E. Grosch

Dr. A. D. Kirwan, Jr.

Dr. Paul S. Schopf

Abstract

SEASONAL VARIABILITY OF HEAT AND MASS TRANSPORT PROCESS
IN THE UPPER TROPICAL ATLANTIC OCEAN:
A NUMERICAL MODEL STUDY

Sang-Ki Lee

Old Dominion University, 1995
Director: Dr. Gabriel T. Csanady

A simple 2.5 layer numerical model was developed and used to illustrate the seasonal variability of heat and mass transports in the upper tropical Atlantic Ocean, associated with the seasonal movement of the Inter-Tropical Convergence Zone (ITCZ). The model ocean was forced by seasonally varying climatological wind and heat flux fields. The entrainment at the base of the mixed layer was scaled by wind stress and shear at the bottom of the mixed layer. On an annual average, the northward transport of the tropical warm water is about 11 Sv, with roughly 10 Sv associated with entrainment of upper thermocline water and the other 1 Sv executing a cross-equatorial path continuously from the South Atlantic. Out of the total 10 Sv of the needed upper thermocline water, 9 Sv enters the equatorial belt from the South Atlantic.

The seasonal response to the ITCZ movement was most striking in the entrainment rate and the warm water escape rate across the northern edge of the equatorial cell. The entrainment rate was found to be significant during May/December and ceased between January and April. The locally forced equilibrium response between

the interfacial shear and the zonal wind stress east of 30°W appears to be responsible for this cycle. The warm water escape toward the North Atlantic takes place mainly between December and May and stops during July/September. Further investigation suggested that the seasonal intensification of the North Equatorial Countercurrent (NECC) serves as a major obstacle to the warm water escape: during July/September the strong negative wind stress curl north of the equator intensifies the NECC, which requires a source of mass at its origin in the west. The North Brazil Current (NBC), therefore, veers offshore completely and provides the mass, terminating the warm water escape via the NBC-Guiana Current route. Strengthening of the NECC also steepens the mixed layer floor, forming a strong potential vorticity front along the northern edge of the NECC. The northward warm water escape via the eastern leg of the cyclonic gyre is therefore limited. In addition, the northward Ekman transport also reaches a minimum during this period. As a result of seasonal variations of the two key processes, namely the entrainment and the meridional transport across the northern edge of the equatorial cell, the tropical warm water pool experiences heat storage during May/October and heat escape in November/April.

The heat budget study of the equatorial mixed layer revealed that, on an annual average, heat gain at the sea surface between 8°S and 8°N is about 0.35 PW, and is used exclusively to warm up the cold water entrained from the upper thermocline layer. The heat-anomaly fluxes across the zonal boundaries are negligibly small. Further analysis showed that the sea surface temperature variation in the tropical Atlantic Ocean is determined by the local heat balance between the atmospheric heating and the entrainment cooling. The model results suggested that the ITCZ movement is the primary cause of the net northward heat transport and its seasonal variation observed in the upper tropical Atlantic Ocean.

This work is dedicated to my parents.

Acknowledgements

I am grateful to my advisor, Prof. Gabe Csanady for his guidance, inspiration and friendship during the last four and a half years. I am also grateful to his wife Joyce for taking me as a part of her family.

My thanks also goes to the other members of my committee, Dr. Chet Grosch, Dr. Denny Kirwan, Jr. A special thanks goes to Dr. Paul Schopf. I would also like to take the opportunity to thank Dr. John Klinck for providing a series of excellent courses. I am thankful to all the staff and my past and present fellow students at CCPO and the Oceanography Department, particularly, Drs. Jose Pelegri and Vittal Gudavalli. I express my gratitude to fellow Korean graduate students in ODU and their families. I am also indebted to my friends in Korea. Kuk-Jin Kim, in particular, helped me in various occasions.

Finally, I would like to thank my father, mother and brother for their love and support.

This work was supported by NOAA on Atlantic Climate Change Program, through a grant entitled "Air-Sea coupling in the North Atlantic", and by the Commonwealth Center for Coastal Physical Oceanography.

Contents

List of Tables

List of Figures

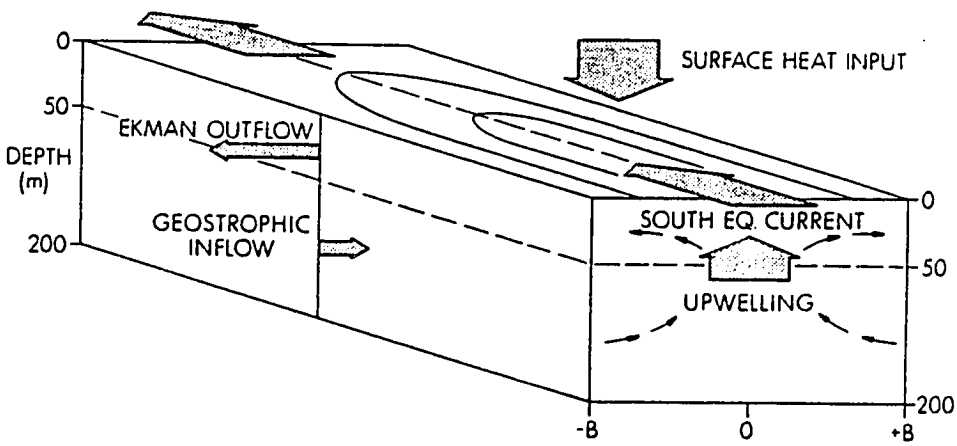

Figure 1: A schematic view that shows the major components of the mass and heat balance in the eastern Pacific Ocean. Reproduced from Wyrtki (1981)

Although subject to the same mechanisms, the meridional heat and mass transport in the tropical Atlantic is dramatically different from the Pacific, since there exists a net northward transport across the equator above the base of the thermocline layer (approximately 26.8 σ_t), which is balanced by a net southward flow in the deep Atlantic Ocean (Stommel, 1968). A number of processes can contribute to this net cross-equatorial transport. While the seasonal movement of the ITCZ appears to be the primary cause, Broecker (1991) introduced the great ocean conveyer belt concept and emphasized the link between the net cross-equatorial transport and the global scale thermohaline circulation. Whatever the exact explanation, since the role of the tropical oceans is to provide the heat deficit occurring in the higher latitude, it is reasonable to assume that the unique pattern of meridional heat transport in the tropical Atlantic is somehow linked to the global air-sea heat budget as well as to climate variability. As the global heat budget studies have revealed the importance of the poleward oceanic heat transport in the tropics and its magnitude well exceeding that of the atmosphere, the attention is focused toward the understanding of the mechanism responsible for the warm water mass formation and escape. However, our understanding on this subject is far from clear to be able to fully portray how the hydrodynamics of the tropical ocean fit into this global heat engine.

Therefore, the principal aim of this study is to establish a basis required for the understanding of the physics responsible for the warm water formation and escape process in the tropical Atlantic Ocean. In an attempt to achieve this objective, we approach this problem by examining the heat and mass transport in the upper tropical Atlantic Ocean, well above the bottom of the permanent thermoclines, using a simple isopycnal layer numerical model. In order to clarify the model results and also to avoid the unnecessary complications arising from the complexity of the numerical model, we attempt to develop a model with only the required physics.

The thesis is organized in the following manner. In chapter 2, some important results from the observational and General Circulation Model (GCM) studies on the mass and heat transport in the tropical Atlantic Ocean are reviewed. Following this is a review of studies involved in the physical explanation of the water formation and escape process. The entrainment parameterization for the tropical ocean is discussed in chapter 3. In chapter 4, before the development of a model suited to the aims of this study, the formulation of some previous tropical ocean models are reviewed, followed by a discussion on the model requirements. The model equations and the details of the numerical formulations are given in chapter 5. Chapter 6 presents the model results and discussion. A comparison between the model results and the observations is given in chapter 7. Finally, the model results are summarized and conclusions are drawn in chapter 8.

2 Background

2.1 Observational Studies

The spatial structure of the warm water mass (WWM) transport in the tropical Atlantic is very well documented in the heat transport calculations of Hastenrath (1982) and Hsiung (1985). Hsiung (1985) examined the annually averaged meridional heat transport for the world ocean, including the Atlantic, using the heat budget equation based on the data collected during the period of 1949-1979 as shown in Figure 2. The values in the figure are zonally integrated and annually averaged. The figure shows that a poleward transport is centered near the equator in the Pacific, while a northward transport is apparent at all latitudes in the Atlantic with a maximum of 9.6×10^{14}W at 20°N. It also indicates that a maximum divergence of the meridional heat transport occurs near the equator both in the Pacific and Atlantic Oceans -its implication being a net oceanic heat gain in these region. A similar study was previously made by Hastenrath (1982) and the results were compatible with those of Hsiung (1985).

The heat transport studies of Hastenrath (1982) and Hsiung (1985) are indirect calculations in which the heat transport values are obtained as a difference between the net oceanic heat gain and the heat storage rate. Therefore, the uncertainties involved in these calculations are potentially high. Direct estimation of the oceanic heat transport was attempted by several authors. However, it requires knowledge of the hydrodynamic field everywhere inside the study area. Therefore, it is usually

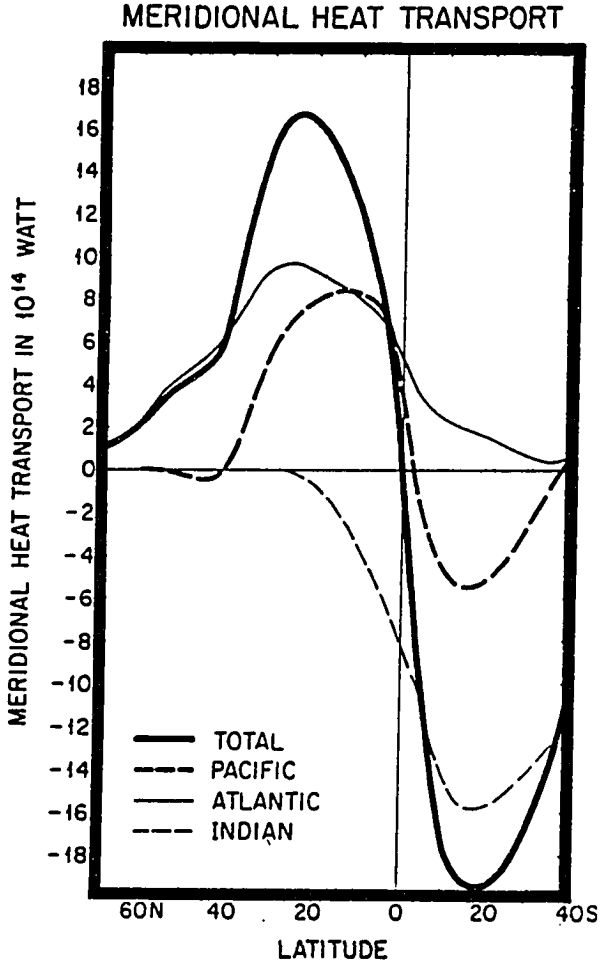

Figure 2: The meridional heat transport for each of the three oceans and for all oceans combined. Positive value indicates a northward transport. Reproduced from Hsiung (1985).

limited to only one or two latitude lines. Fu (1981), using the hydrographical data of IGY and METEOR expeditions, applied the inverse method of Wunsch (1978) to the South Atlantic Ocean to determine the meridional oceanic heat transport. In order to compute the total heat transport, the Ekman and geostrophic heat transports were estimated separately and added afterwards. The computed geostrophic heat transport was always equatorward, while the Ekman heat transport was directed toward south and generally smaller than 50% of the geostrophic heat transport. Consequently, the heat transport in the surface layer was very small and the direction of the total heat transport largely followed that of the thermocline layer (equatorward) with the total heat transport of 8×10^{14}W near 30°S and 4×10^{14}W near 8°S. It was also found that the major route of the heat transport is to be the Benguela Current, the South Equatorial Current (SEC) and the North Brazil Current (NBC).

Similar calculations were made by Wunsch (1980) and Roemmich (1980) in the North Atlantic Ocean. Both estimated northward heat transport of about 12×10^{14}W near 24°N; however, the tropical Atlantic Ocean was not included in their studies. A more extensive heat transport study of the tropical Atlantic was made later by Roemmich (1983). Using the inverse method of Wunsch (1978), Roemmich (1983) calculated the geostrophic transport of mass and heat at 24°N, 8°N, 8°S and 24°S in the Atlantic. These four latitude lines were divided into eight isopycnal layers defined by surfaces of different water masses, and and each of layer was examined individually. The geostrophic transport in each layer is shown in Figure 3(a). In the upper ocean, above the Antarctic Intermediate Water, the geostrophic mass transport is strongly northward across 8°S and southward across 8°N, forming a strong geostrophic mass convergence toward the equator. The total transport in the surface layer was obtained by combining the geostrophic and the Ekman components as shown in Figure 3(b). Considering continuity of mass, it indicates that, between 8°N and 8°S, there must be some entrainment of its rate at least 6 Sv from the thermocline

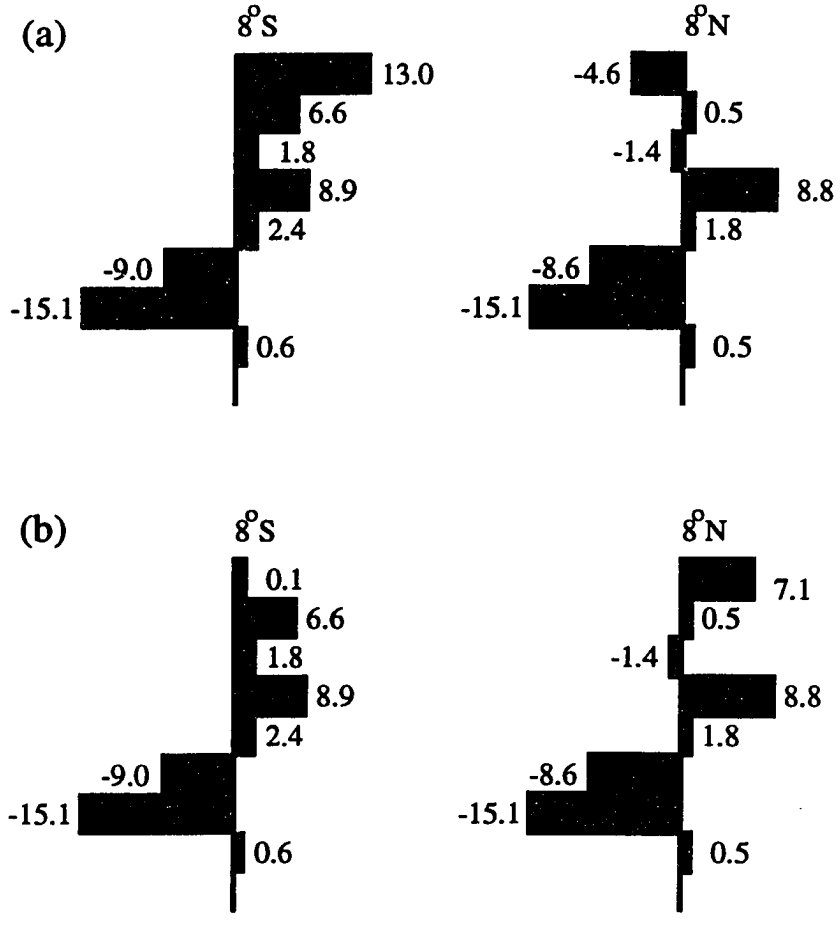

Figure 3: (a) Geostrophic layer transports (in unit of Sv), with northward transports to the right of zero line. (b) The sum of geostrophic and Ekman transports. Modified from Roemmich (1983)

waters to the surface water which in turn escapes northward; Broecker *et al.* (1978) and Wunsch (1984), based on the distribution of bomb radiocarbon in the Atlantic Ocean, estimated the entrainment rate of 17 Sv and 10 Sv individually. Roemmich also estimated the meridional heat flux for each of the four latitudes using the similar method, as shown in Table 1. It shows that the Ekman heat flux dominates over the geostrophic heat transport at 8°N, while the geostrophic heat transport dominates at 8°S, clearly explaining different mechanisms of the net northward heat transport in each hemisphere of the tropical Atlantic.

The inverse calculation of Roemmich (1983) provided a zonally and annually averaged picture of the meridional heat and mass transport in the tropical Atlantic Ocean. But a major question that arises from this study is which components of the equatorial circulation system are responsible for the cross-equatorial heat and mass transport. In an attempt to answer this question, Gouriou and Reverdin (1992) analyzed the data collected from their eight cruises in 1982-1984 to describe the meridional as well as zonal patterns of the mass and heat transport. Their result is summarized in Figure 4. The solid and dashed arrows represent the surface and thermocline mass transport, respectively. They estimated that 9.4 Sv of the EUC transport above 15°C, being fed by the recirculation of the subsurface NBC, originate from the South Atlantic, with the remaining 8.6 Sv originating from off-equatorial subsurface water (18 Sv in total). During the eastward equatorial route, approximately 11 Sv is entrained to surface mixed layer which in turn escapes the equatorial cell via the surface NBC (7 Sv; adopted from Schmitz and Richardson, 1991), suggesting the major route of mass transport in the tropical Atlantic Ocean to be the subsurface NBC, the EUC, the equatorial entrainment and the surface NBC. The remainder 7 Sv in the thermocline layer is transported out from the equator and joins the off-equatorial water when the EUC hits the African Coast. As discussed previously, Fu (1981) showed that the ultimate source of the subsurface NBC is the

Latitude	Geostrophic heat flux	Ekman heat flux	Total heat flux
24°S	112	-51	61
8°S	166	-92	74
8°N	-28	189	161
24°N	92	56	148

Table 1: Heat flux computed from geostrophic and Ekman fluxes. The unit is 10^{13}W. Reproduced from Roemmich (1983).

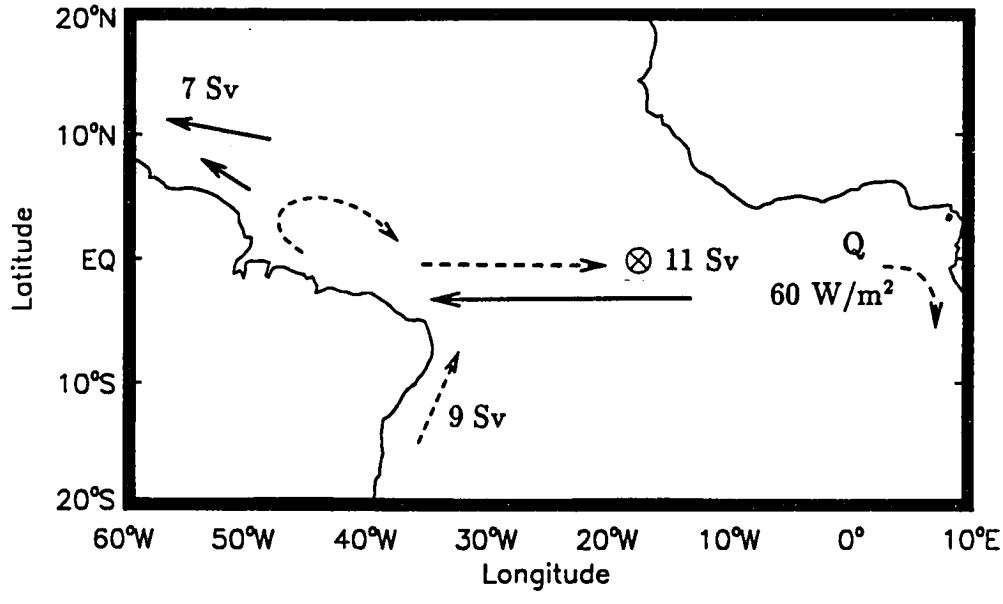

Figure 4: A sketch of equatorial circulation for surface layer and upper thermocline. Net upwelling, heat and fresh water budgets are also summerized. Reproduced from Gouriou and Reverdin (1992).

northwestward South Equatorial Current (SEC), which forms the northern leg of the subtropical gyre being fed by the northward Benguela Current off the coast of Africa.

Hastenrath and Merle (1985) further explored the temporal and spatial variations of heat transport in the tropical Atlantic Ocean between 20°S and 30°N. The data were collected from the subsurface temperature soundings compiled until 1978 and evaluations of the net heat gain from long-term ship observations between 1911 and 1970. The oceanic heat budget equation can be written as

$$Q_{SW} - Q_{LW} - Q_S - Q_E = Q_T + Q_V. \quad (1)$$

The left-hand terms are the net short wave (Q_{SW}), net long wave (Q_{LW}) radiation, sensible (Q_S) and latent heat (Q_E) flux at the sea surface, while the right-hand terms are the heat storage rate (Q_T) and lateral heat export (Q_V) where the sum of two right-hand terms (Q_T+Q_V) represents the net oceanic heat gain. The heat storage rate Q_T was obtained by integrating the subsurface temperature from the sea surface to the depth where the annual temperature variation vanished.

The net oceanic heat gain (Q_T+Q_V), the heat storage rate (Q_T) and the heat divergence (Q_V) are reproduced from Hastenrath and Merle (1985) in Figure 5. The divergence of oceanic heat transport (Q_V) exhibits patterns broadly inverse to that of the heat storage rate (Q_T). This indicates that the heat storage rate (Q_T) is determined entirely by the heat transport divergence caused by tropical ocean dynamics rather than the seasonal heat flux on the sea surface (Q_T+Q_V). Similar suggestions have been offered previously by Merle (1980) and Levitus (1984). On an average over the equatorial belt between 10°S and 10°N, heat escape (negative Q_T) is apparent during March/May and November/December while heat accumulation (positive Q_T) prevails in August/October. Figure 6(a) shows the annual march of Q_T in four different sectors in the equatorial Atlantic as indicated in Figure 6(b). A west-east seesaw variation is evident in the equatorial belt between 6°S and 6°N: the heat accumu-

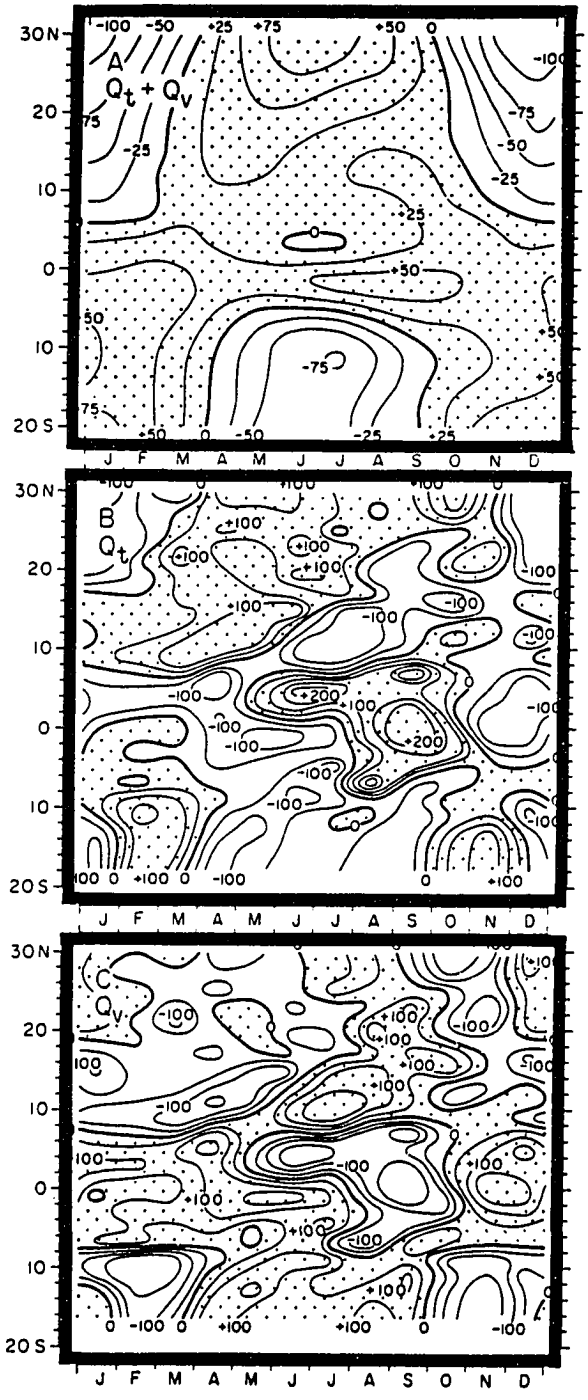

Figure 5: Latitudinal and annual variation of oceanic heat budget. (a) net surface heat gain (Q_T+Q_V). (b) heat storage rate (Q_T). (c) heat divergence (Q_V). Reproduced from Hastenrath and Merle (1986).

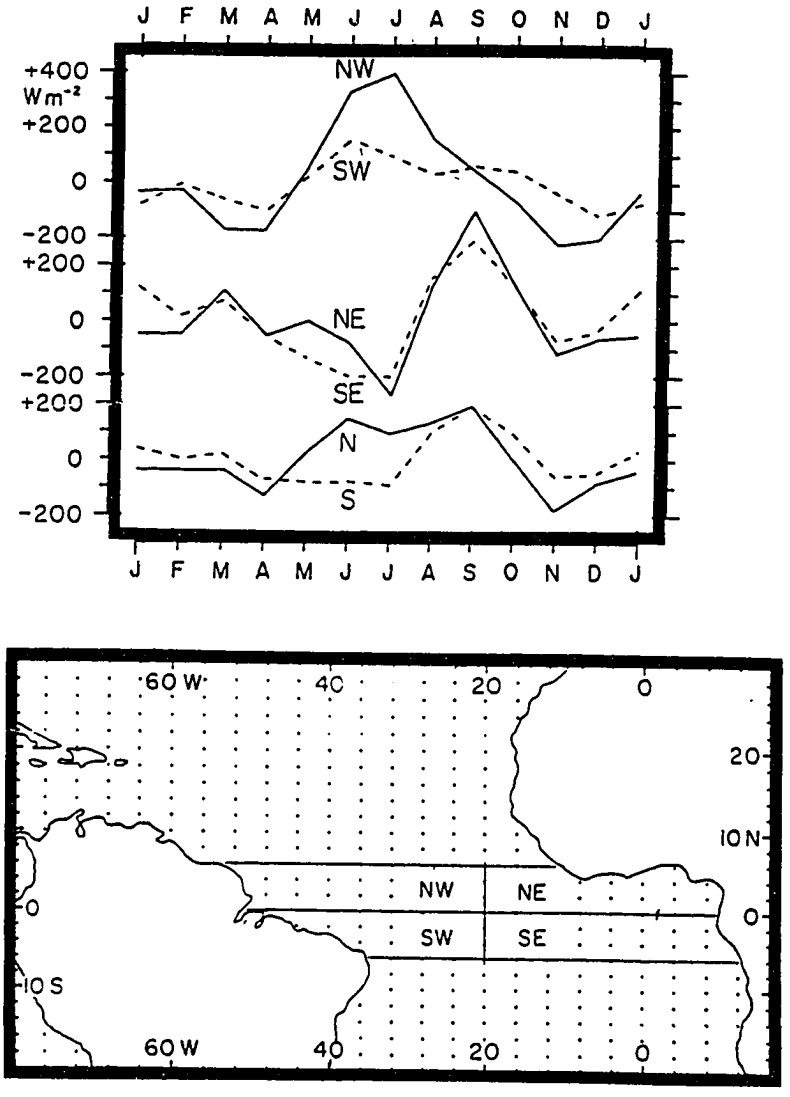

Figure 6: (a) Annual march of subsurface heat storage (Q_T) in the tropical Atlantic Ocean. (b) The symbols NW, SW, NE and NW used in (a) are explained here. Reproduced from Hastenrath and Merle (1986).

lation predominates in the western equatorial Atlantic during June/July, while the heat escape continues in the east. When the heat accumulation of the eastern basin goes to maximum in August/September, the western basin starts to experience the heat escape. This seesaw variation is consistent with the seasonal variation of the 23°C isotherm observed in the equatorial Atlantic (Figure 7); the heat accumulation in the west and the heat escape in the east during June/July largely agree with the deepening of upper layer in the west and shoaling in the east (Merle, 1980). Hastenrath and Merle (1985), therefore, concluded that this seasonal and spatial variation of heat storage in the tropical Atlantic Ocean is not governed by the upper layer temperature but by the upper layer depth change which is more or less in phase with the seasonal zonal wind stress cycle (Katz and collaborators, 1977).

Another interesting 180° out of phase relation was observed between the latitudinal bands between 5°S to 8°N and 8°N to 15°N as shown in Figure 5. Garzoli and Katz (1983) related this to the seasonal cycle of the thermocline displacements associated with the NECC and its relation to the meridional shifting of the ITCZ. This heat budget feature was further studied by the EOF analysis of Katz and Garzoli (1984) and the surface dynamic topography study of Merle and Arnault (1985).

2.2 General Circulation Model (GCM) Studies

The observational studies discussed above have many limitations which can be overcome with numerical models. Bryan and Lewis (1979) analyzed the seasonal heat budget of the world ocean by using a primitive equation numerical model of the type developed by Bryan (1969). The model had a very coarse resolution of about 5° in the horizontal and 12 levels in the vertical direction. Only the annual mean plus the first harmonic wind stress were used to drive the model ocean, and the linear damping forced the temperature and salinity of the surface cell toward

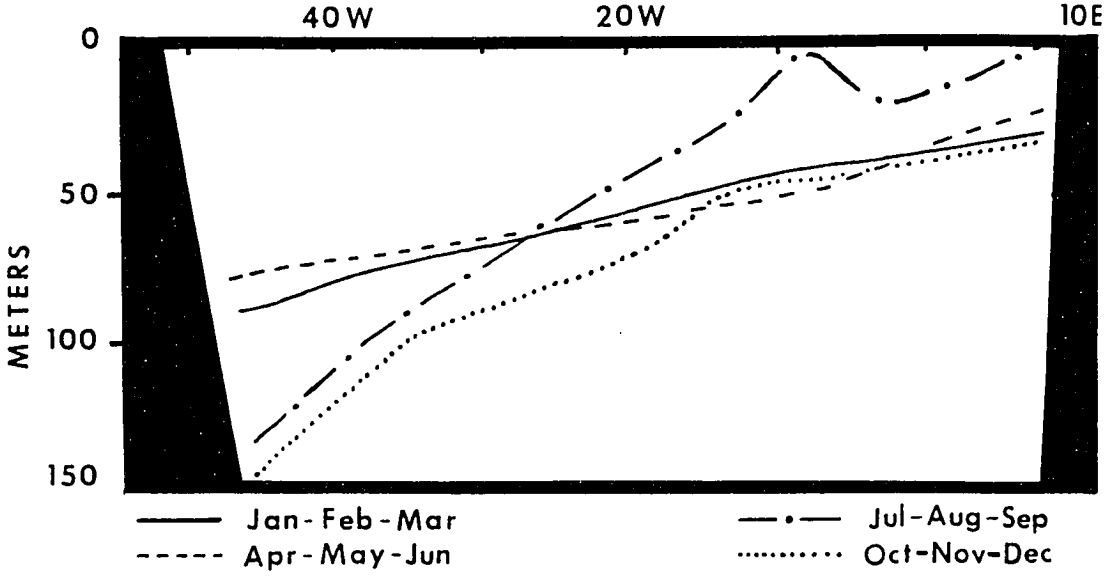

Figure 7: The depth (in meter) of the 23°C isotherm in the equatorial plane of the Atlantic Ocean in different seasons. Reproduced from Merle (1980).

observed values. The zonally averaged northward heat transports for the Pacific and the Atlantic Ocean from the model are reproduced in Figure 8. The seasonal changes in poleward heat transport of the Pacific are much larger than those shown for the Atlantic Ocean. In the tropical Pacific, the poleward heat transport varies approximately from 10×10^{14}W in January to -10×10^{14}W in July, while the model predicted a net northward heat transport of about 2.5×10^{14}W in July and 5×10^{14}W in January in the tropical Atlantic. Direct estimates of the heat transport by Bryden and Hall (1980), Wunsch (1980) and Roemmich (1980) all indicate that the heat transport is much more intense than what the model predicted. However, the model result suggests heat accumulation in July and heat escape in January for the tropical Atlantic, which agrees qualitatively with the indirect heat transport calculations of Hastenrath and Merle (1985) described earlier.

Following Bryan and Lewis (1979), Sarmiento (1986) investigated the heat transport process in the Atlantic Ocean between 25°S and 65°N using the primitive equation numerical model of Bryan (1969) with 25 levels in the vertical direction and a horizontal resolution of about 2°, which is just about the size of the internal deformation radius in the tropics. The model was forced by the monthly mean wind stress of Hellerman and Rosenstein (1983). Similar to Bryan and Lewis (1979), the temperature and salinity were fixed at the surface with the monthly mean data from Levitus (1982). The model result showed that, on an annual average, the equatorial region gained a large amount of heat associated primarily with the conversion of the northward geostrophic flow from the South Atlantic to the surface Ekman flow in the North Atlantic, estimated up to 6 Sv. The conversion process from the geostrophic to the Ekman flow implies a net mass and heat transfer between the thermocline layer and the surface layer. This is consistent with the aforementioned inverse calculation of Roemmich (1983), in which he estimated about $6 \sim 10$ Sv of the conversion rate. He also found that the seasonal cycle of low frequency northward heat transport was

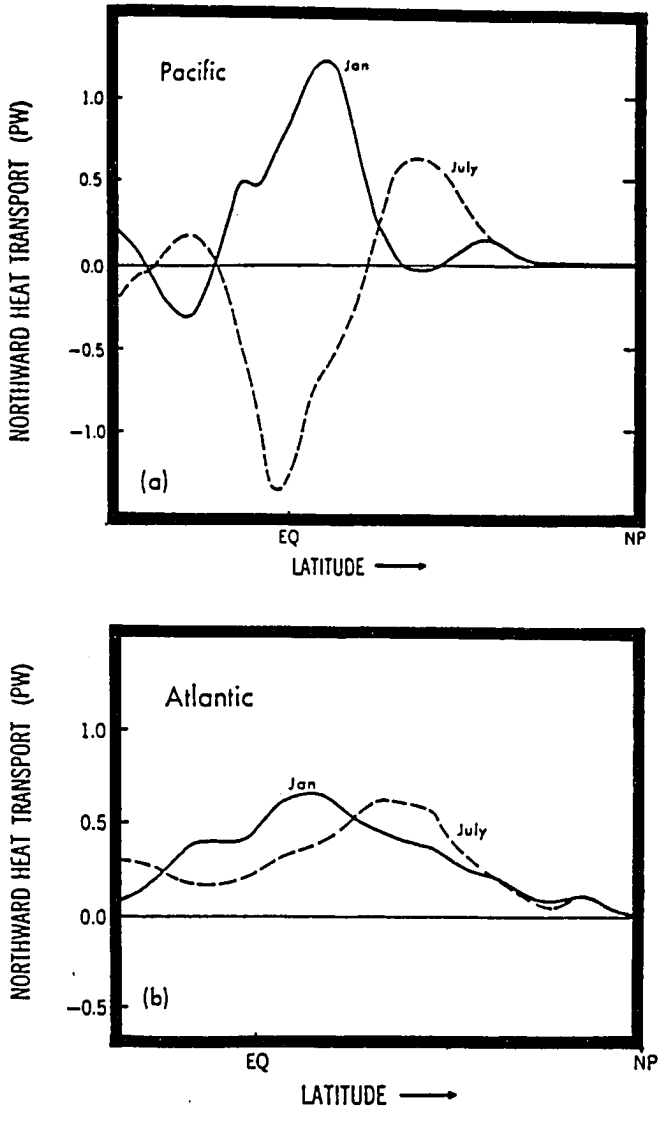

Figure 8: Heat transport for (a) the Pacific and (b) the Atlantic in January and July. The unit is petawatts ($1\text{Pw} = 10^{15}\text{W}$). Reproduced from Bryan and Lewis (1979).

almost identical to that of the North Equatorial Counter Current (NECC). More precisely, he observed that the northward heat transport went minimum in northern summer when the NECC dominated the surface flow and to maximum in the winter when the NECC disappeared and the northward Ekman transport dominated, suggesting a dynamical connection between the cycles of the NECC and the meridional heat transport. Details of heat transports by individual mechanisms, namely the geostrophic, eddy and Ekman transports, were also illustrated in this paper.

Sarmiento's (1986) work was further extended by Philander and Pacanowski (1986). They used basically the same model developed by Bryan (1969), this time however, the horizontal resolution was about 0.3° near the equator and the surface heat flux was directly calculated from the meteorological variables. Special attention was given in determining the value of the vertical viscosity and the diffusivity coefficient (see Pacanowski and Philander, 1981). Apart from the results similar to its predecessors, the model result showed that the seasonal variations of heat transport were significant only between 15°N and 5°S, as shown in Figure 9. They observed that the heat transport across 5°S and across 15°N had little seasonal variation. Across 8°N, however, the northward heat flux varied from 1.75 PW in January, when the NBC flowed continuously into the Gulf of Mexico, to -0.2 PW in August, when this current veered offshore near 5°N to form the NECC. They, therefore, concluded that the zonal bands 5°S to 8°N and 8°N to 15°N act as capacitators of heat that are out of phase in time. This model feature was consistent with the results from Merle's (1980) data analysis.

2.3 Formation and Escape of the Warm Water Mass

Based upon the observations and numerical studies discussed above, it appears that the formation of the WWM takes place mostly through the equatorial entrain-

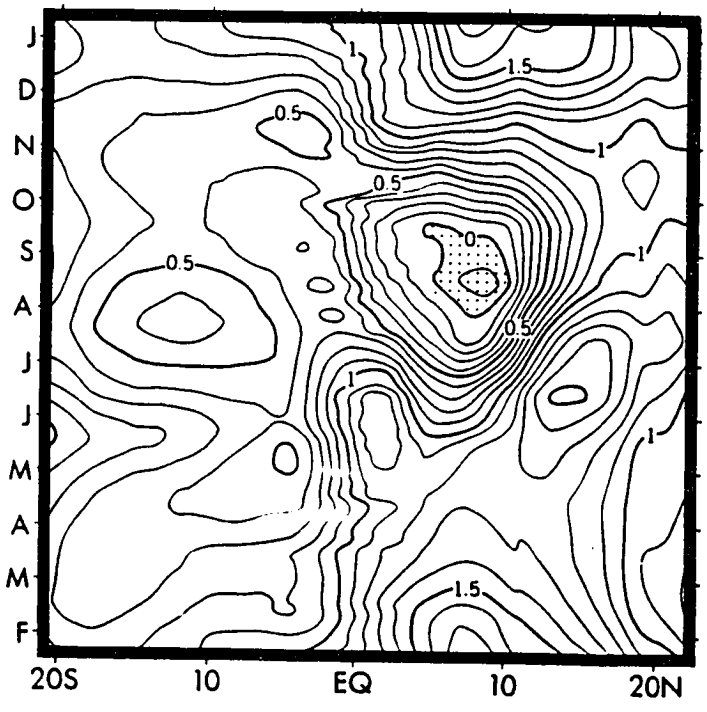

Figure 9: The zonally integrated meridional heat transport (in unit of Pw) as a function of month and latitude. Reproduced from Philander and Pacanowski (1986).

ment and the escape across the northern edge of the equatorial belt toward the North Atlantic (Csanady, 1987). For this reason, here we review the seasonal cycle of the entrainment and also the individual current systems near the northern edge of the equatorial belt, namely the NBC and the NECC. Some of the materials given in this section are partially repetitive of the two previous sections. Therefore, the following review is rather limited, concentrating only on the subjects in hand.

Seasonal Appearance of Cold Water Tongue

The SST in the tropical Atlantic is characterized by the summer appearance of a cold water tongue in the Guinea Gulf. Since there are no other sources of the cold water near this area (Picaut, 1983), it is usually believed that this sudden change of the SST is a manifestation of intense vertical mixing between the warm mixed layer and the relatively cold upper thermocline layer during northern summer. However, the underlying physics responsible for this vertical heat exchange process and its seasonal cycle are not clear at all. In an attempt to explain this, Houghton (1976) analyzed the SST variation using a simple wind mixing scenario. From the historical data set, he studied the correlation between the local wind stress and the SST variation near the Gulf of Guinea where the summer cold water tongue was observed. The result revealed, however, almost no correlation between the local wind stress and the SST change.

An alternative mechanism was, therefore, proposed by Moore *et al.* (1978). They argued that the summertime cold water tongue could be initiated by Kelvin waves, which were excited by the increased wind stress in the western part of the equator. The idea was based on an assumption that the lowered SST coincides with the uplifted isotherm. As clearly pointed out by Schopf and Cane (1983), however, the uplift of isotherm (or upwelling) does not change the SST; the entrainment does and they

are not necessarily correlated. Therefore, although supported by many observational and numerical studies (*e.g.*, Adamec and O'Brien (1978); Servain *et al.*,1982; Picaut, 1983), this remotely forced upwelling hypothesis is still very controversial.

Another hypothesis, also controversial, is based on the idea that the summer appearance of cold water tongue is due to the vertical mixing induced by the increased vertical shear between the westward South Equatorial Current (SEC) and the eastward Equatorial Undercurrent (EUC). Clear evidence was found by Voituriez and Herbland (1977). In the summer of 1975, they observed that the vertical shear was increased by the acceleration of the SEC and by the shoaling of the EUC. They calculated the Richardson number near the pycnocline at the equator (4°30'W) and found that it decreased from 5 to 0.3 between March and August in 1975, thereby indicating much higher shear in the August.

Surface Heat Gain near the Cold Water Tongue

The warm water formation process is completed only when the net oceanic heat gain in the tropics is utilized to warm up the cold water brought up by the entrainment (Csanady, 1984). This is accomplished due largely to the fact that the evaporation into the atmosphere is much slower in the cold water, hence releasing the latent heat into the atmosphere less efficiently. Niller and Stevenson (1982) developed a simple but effective heat budget scheme to quantify the heat necessary for the warm water formation. They integrated the heat content equation along 25°C isotherm, thereby canceling out the heat advection terms, to obtain a direct relationship between the entrainment cooling and the surface heat flux. They found that approximately 0.2 PW is required for the warm water formation. If the value is divided by the approximate space of the equatorial cell bounded by 25°C isotherm, we get about 8 W/m^2. Based on the mean heat flux value of 10 $\sim$ 15 W/m^2 inferred from Hastenrath (1982), the

8 W/m^2 represents about 60 $\sim$ 80 % of the total heat gain averaged over the tropics. Of course, this is just a rough estimation so that the exact value must not be taken too seriously. Even so, it still implies that the warm water formation process in the tropical Atlantic is one of the key control features in the global oceanic heat budget equally important to the cold water formation in the polar ocean (Csanady, 1984). The model of Niller and Stevenson (1982) was further used by Reverdin (1985) to include the seasonal upwelling effect.

Escape of the Warm Water Mass

The North Brazil Current (NBC) is thought to be an important conduit of the poleward escape of the warm water mass (WWM) in the tropical Atlantic Ocean. Based on several observational studies, Csanady (1985) reviewed the seasonal behavior of the NBC and its continuation to the Guiana Current. He concluded that the South Equatorial Current (SEC) transports about 30 Sv to the NBC between July and December, of which 20 Sv turns offshore to form the North Equatorial Counter Current (NECC) and the remaining 10 Sv continues northwestward as the Guiana Current, while in the months January/July, the transport from the SEC to the NBC is reduced to about 10 Sv, which continue to flow into the Guiana Current without retroflection. Accordingly, he suggested a constant flow of 10 Sv from the NBC to the Guiana Current, regardless of the season. This contradicts with the conventional view that the NBC flow turns into the NECC in summer but continues along the Guiana Current in winter.

This scenario was supported later by the high resolution GCM study of Schott and Boning (1991). They found no significant increase of the northwestward transport from the NBC to the Guiana Current in northern summer. Nevertheless, the estimation of Csanady (1985) must be taken with a caution. His estimate was based

exclusively on the ship drift map of Richardson and McKee (1984), which shows only the surface velocity averaged for a very long period. Therefore, he had to assume the mixed layer depth to be constant (100 m) everywhere to extract the mass transport value out of the surface velocity. Furthermore, there are several numerical and observational studies which disagree with the conclusion of Csanady (*e.g.*, Philander and Pacanowski, 1986). In fact, the degree of seasonal connection from the NBC to the Guiana Current remains a controversial issue. (Johns *et. al.*, 1990).

In addition to the major escape route of NBC-Guiana Current system, Csanady (1987) suggested a secondary route of the WWM transport from the NBC to the North Equatorial Current (NEC) via the interior of the cyclonic gyre located between the NECC and the NEC. He argued that since the western boundary current of the cyclonic gyre is always directed northward, the interior northward flow via the eastern leg of the cyclonic gyre must then be supplied by the NECC, so that a link of NBC-NECC-NEC is formed. He estimated that, on an annual average, about 10 Sv should escape via this route.

Jones *et al.* (1990) discovered another pathway of the WWM escape. Using coastal zone color scanner (CZCS) images from 1979 to 1980, they found that several anticyclonic eddies of about 400 km diameter are pinched off near the NBC retroflection point and drifted northwestward along the coast of South America. Didden and Schott (1993) also identified five retroflection eddies from their satellite altimetry data, solidifying Jones *et al.* (1990) observations. Recently, Richardson *et al.* (1994) suggested that these eddies could provide a significant northward mass transport of about 3 Sv even during northern summer when the NBC retroflects to feed the NECC.

In the course of delineating the mechanisms of warm water escape, we omitted the contribution of Ekman transport which could be potentially important. Since the western boundary current, geostrophic interior transport and the Ekman flux are op-

erated by different mechanisms, it is important to determine which plays a dominant role. Wyrtki (1981) investigated a similar problem in the eastern Pacific Ocean. Using a simple mass balance principle with a help of hydrographic data, he found that, within the top 50 m, the poleward Ekman heat flux dominates over the equatorward geostrophic heat transport. However, the influence of the western boundary current was not included in the domain of his study. This effect was investigated earlier by Schopf (1980), who used a normal mode numerical model to portray the relative roles of the Ekman and geostrophic heat transports in the tropical ocean. Applying simplified seasonal zonal wind stress on the model sea surface, he observed that the seasonal cycle of the zonally intergrated meridional heat transport was dominated by the Ekman transport cycle. The geostrophic transport signal was found not strong enough to alter the shape of the total heat transport, although it could be significant locally. Despite the oversimplified nature of the model, his result suggests a very important possibility that the heat transport via the western boundary current and the interior geostrophic current cancel, allowing the Ekman signal to dominate. It appears that the GCM study of Sarmiento (1986), to a certain extent, agrees with Schopf's (1980) result. Based on the model results, Sarmiento (1986) divided the total heat transport into the Ekman flux, eddy transport and the remaining terms (mostly geostrophic) as shown in Figure 10. Between the equator and 10°N, the northward heat transport cycle is predominated by the Ekman transport cycle, while the geostrophic transport is relatively uniform in season. The minimum heat transport centered at 5°N during July/October is especially attributed to the influence of the weak Ekman heat transport in these months.

Concerning the seasonal variation of the warm water escape in the tropical Atlantic, Hsiung *et. al.* (1989) calculated the seasonal heat transport from the difference between the net oceanic heat gain and the heat storage rate. However, the estimate was not accurate enough to determine the full seasonal cycle of the heat transport,

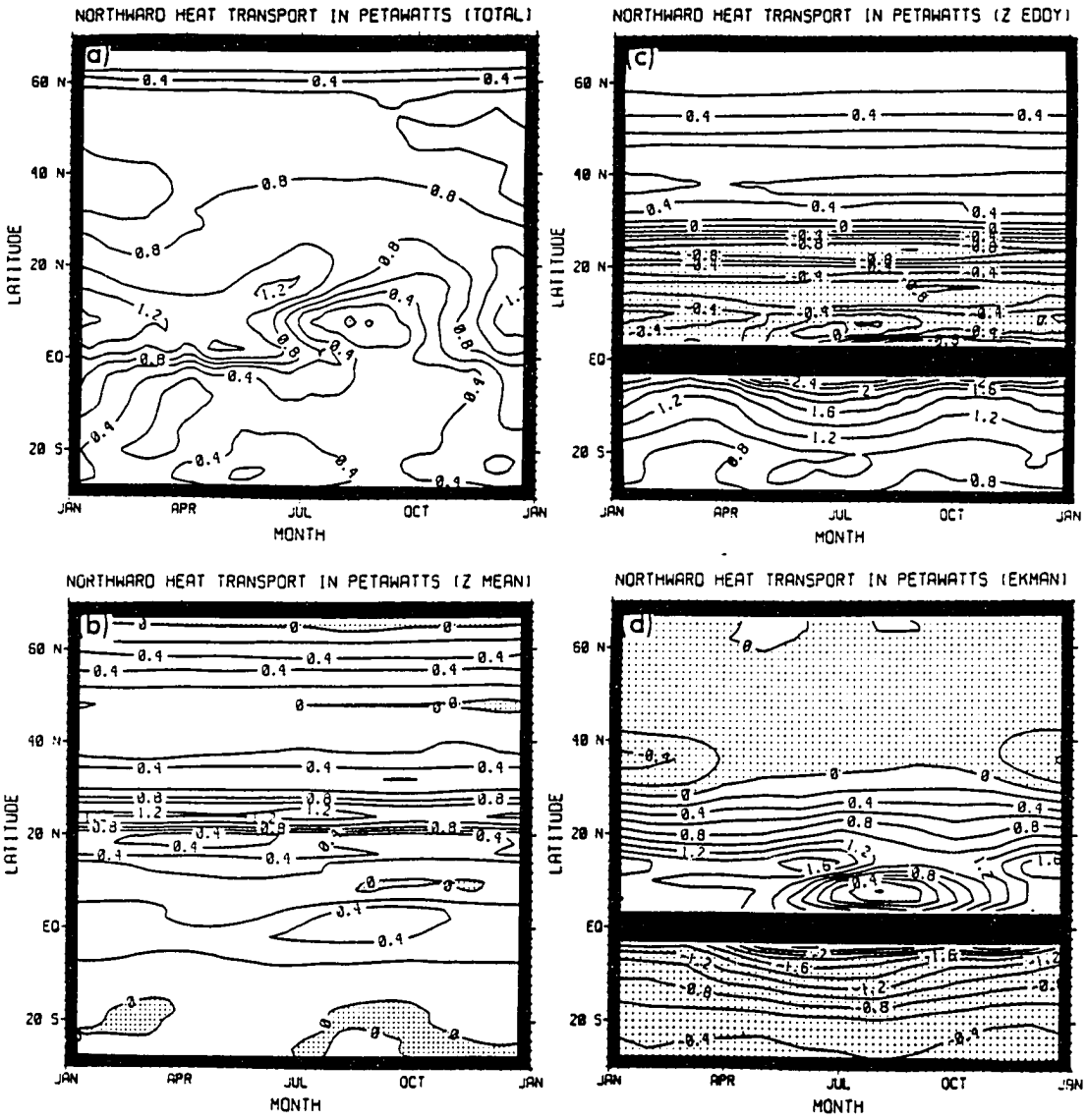

Figure 10: Model-produced (a) total heat transport, (b) geostrophic heat transport, (c) eddy heat flux and (d) Ekman heat flux as a function of month and latitude. Reproduced from Sarmiento (1986)

especially since the standard deviation of their study was as great as the heat flux values. The GCM studies of Sarmiento (1986) and Philander and Pacanowski (1986) appear to be the better sources of our estimation. While their numerical configurations may differ considerably, they all agree that the warm water escape is significant in northern winter and spring, and it goes to minimum in northern summer (Figure 9).

NBC and its Retroflection into the NECC

Previously, it was noted that there are at least three different routes of the WWM escape into the subtropics of the North Atlantic. It appears that these three are totally or partially dependent upon the retroflection of the NBC and its connection to the NECC. Although different studies do not agree whether the formation of the NECC enhances or inhibits the WWM escape, there is no doubt that the retroflection of the NBC and the formation of the NECC play significant roles on the seasonal cycle of the WWM escape.

Probably, the most dramatic feature in the tropical Atlantic is the seasonal appearance of the NECC. It is a well known fact that the seasonally intensifying NECC is a direct result of the negative local wind stress curl (or Ekman convergence) (Sverdrup, 1947). The seasonal behavior of the NECC is very well described in the surface current map of the Richardson and McKee (1984). Based upon historical ship drift velocities, they showed that the NECC extends as a continuous eastward-flowing current in the band 5°N-8°N from June to December and disappears during January/May. Figure 11, reproduced from Richardson and McKee (1984), is a monthly profile of surface zonal current in the central Atlantic at 25°W-30°W. According to the figure, the NECC starts in June and its strength gradually increases until August/September then disappears in January. At the same time, the core of NECC is shifted northward from 5°N to 8°N between June and August, then back to 5°N

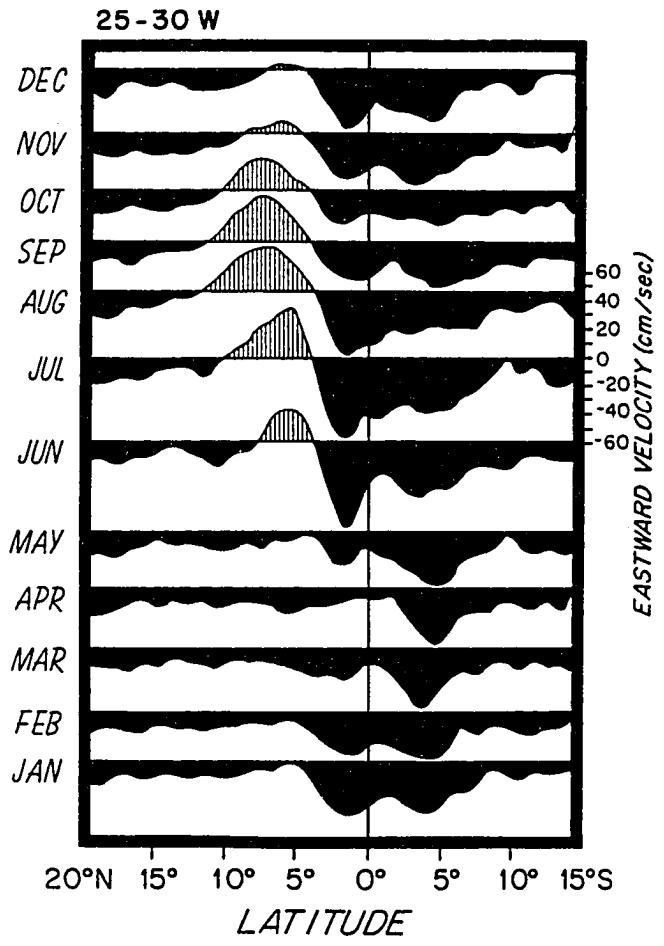

Figure 11: Monthly north-south profiles of zonal currents in the central Atlantic at 25-30°W. Reproduced from Richardson and McKee (1984).

during September/December. It is important to point out that, since the wind stress curl vanishes along the ITCZ, this migration of the NECC core roughly coincides with that of the ITCZ.

The seasonal variation of the NECC usually accompanies rise and fall of the thermoclines across its location. Garzoli and Katz (1983), using hydrographic data, analyzed the thermal structure associated with the NECC and its relation to the ITCZ movement. They found that the depths of the thermocline in the southern and the northern parts of the NECC core oscillate 180° out of phase to each other annually. This feature is shown in Figure 12 along with associated wind stress curl in these regions. The figure shows clearly that the curl of the wind stress (or Ekman pumping) is qualitatively correlated with the thermocline depth variations. In order to quantify this relationship, Busalacchi and Picaut (1983) used a single layer reduced gravity model with the realistic wind and geometry. They calculated the different terms of the linearized time dependent vorticity equation from their model results. From the analysis performed by this, they reached a conclusion that the major contribution in their vorticity equation representing the model thermocline variation north of the NECC is Ekman pumping (or wind stress curl), and south of the NECC is a combination of the Ekman pumping and the westward propagating Rossby waves.

Therefore, the dynamics of the NECC and the associated thermocline oscillation are basically local responses to the surface vorticity input; however, the behavior of the western boundary current (NBC) is not subject to the local balance but to the basin wide response. Because of this reason, our theoretical understanding of the NBC dynamics is very primitive, especially, since the separation of the NBC is one of the most puzzling problems for theoretical oceanographers. There exists, however, a couple of interesting ideas relevant to the seasonal separation of the NBC, but none

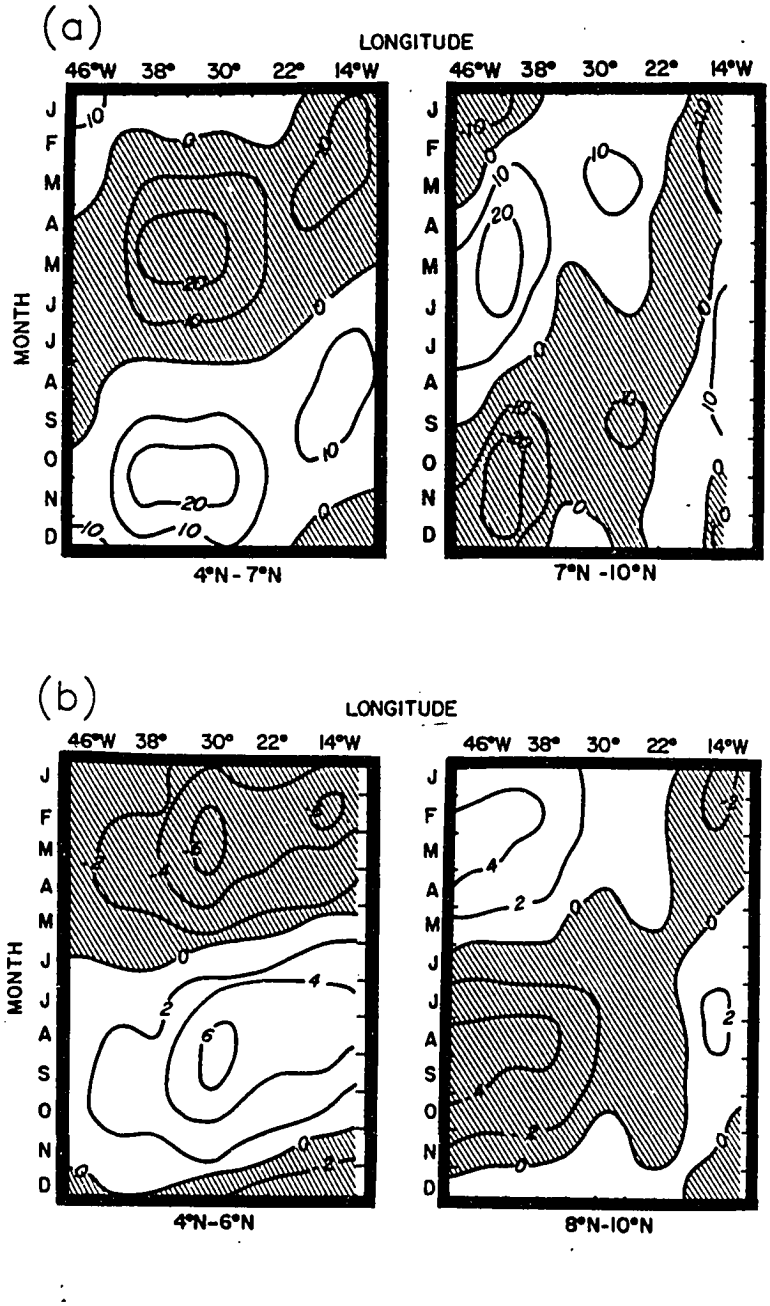

Figure 12: Variation of (a) thermocline depth and (b) curl of the wind stress as a function of time and longitude for the southern (4°N to 7°N) and northern (7°N to 10°N) sides of the NECC. The annual means are subtracted at each 4° longitude band. Units are meter for the thermocline depth and dyn/cm^{-3} for the wind stress curl. Reproduced from Garzoli and Katz (1983)

is so well founded in theory as to be convincing. There is a substantial body of work on the separation of the western boundary current in the mid-latitude. (Cessi, 1990; Parsons, 1969; Veronis, 1981). According to these theories, the separation of western boundary current from the coast is associated with the surface outcropping of the thermocline. This line of work was later applied on the separation of the NBC by Condie (1991). But as clearly stated by Csanady (1990), in separating NBC, the thermocline remains absolutely submerged; therefore, this outcropping-separation mechanism is not a plausible idea for the separation of the NBC.

The classical theories of the wind-driven circulation suggests that the principal role of the western boundary current is to close the mass imbalance caused by the meridional Sverdrup transport in the interior. Based on this idea, one may argue that the separation of the NBC is a response of the western boundary current to the interior Sverdrup transport (NECC in this case). This hypothesis was later challenged by a new idea introduced by Csanady (1985), in which he suggested that the NBC separation from the coast is due to the potential vorticity (PV) front developed as the low PV waters coming from the south run into high PV waters in the northern part. The PV map near the retroflection point produced by Flagg *et al.*, (1986) supported his idea.

McCreary and Kundu (1988) explored a possible effect of slanted geometry of the coast line on the boundary current separation. Although their numerical model was originally applied to the Somali Current, the model result suggests that the slanted western boundary may support the separation of the western boundary current.

3 Physics of Entrainment

The nature of the large-scale ocean circulation model requires a separate form of the equation for the entrainment rate as a function of model variables. In this chapter, we review some of the classical and modern ideas of the entrainment parameterization and the physical assumptions behind them. Based on this review, we arrive at an entrainment formula reasonably suited for the the tropical ocean.

Before, we proceed, it is important to realize that the entrainment is one of the most important elements of the mixed layer dynamics. The oceanic mixed layer is a fully turbulent region of the upper ocean, bounded above by the air-sea interface. The wind and upward latent heat flux through the sea surface maintain the generation of the turbulence. At the same time, the mixed layer is in contact below with a relatively stable thermocline layer. The vertical fluxes of heat, salt and momentum take place through this interface, and they are also very important in maintaining the structure and dynamics of the mixed layer.

Earlier work of Kraus and Turner (1967) provides a basis for understanding the physics of the mixed layer. The model was based on a concept that a fraction of the turbulent energy from the wind is used to entrain the denser water from the thermocline layer; therefore, a direct relationship between the wind stress and the entrainment rate was obtained. Later, Kato and Phillips (1969), through a careful laboratory experiment, found an entrainment law valid over Richardson numbers

between about 20 and 300:

$$w_e = 2.5\frac{u^{*3}}{g'H} \quad , \tag{2}$$

where u^* is the frictional velocity determined from the surface stress only, g' and H are the reduced gravity and the mixed layer depth, respectively. Since Kato and Phillips (1969) performed the classical laboratory experiment on the turbulent mixing in stratified shear flow, a large number of laboratory studies has been conducted. See Fernando (1991) for the summary of these studies.

In the ocean, the vertical mixing is also triggered by local shear instabilities (Kelvin-Helmholtz type) at the base of the mixed layer. Thorpe (1987) described stages involved in the transition from small amplitude Kelvin-Helmholtz instability to fully developed turbulence. In this context, Pollard *et al.* (1973) argued that the dominant source for the turbulence mixing energy originates mostly from the mean shear; therefore, they used the mean shear (Δu) as the frictional velocity scale instead of the surface stress u^*. Price (1979) reexamined the Kato and Phillips (1969) experimental results and derived an entrainment law using Δu as the frictional velocity scale. Later, he applied this result to obtain the upper ocean response to a moving hurricane using a fully nonlinear time dependent numerical model (Price, 1981). Koop and Browand (1979), Christodoulou (1986) and Narimousa and Fernando (1987) derived entrainment laws of their own based upon assumptions similar to Pollard *et al.* (1973). However, these models included only the turbulence generated from shear instability and failed to consider the turbulent energy input from the wind (Fernando, 1991).

In a departure from Kraus and Turner (1967) and Pollard *et al.*(1973), Jones and Mulhearn (1983) suggested a new way of parameterizing the entrainment rate. Their underlying assumption was that the turbulent mixing is maintained by both surface stress and the shear at the interface, so that $\sqrt{\Delta u u^*}$ must be the relevant frictional

velocity scale. According to Voituriez and Herbland (1979), this assumption is clearly valid in the tropical Atlantic Ocean; therefore, it is conceivable that the Jones and Mulhearn (1983) model provides an appropriate parameterization for estimating the entrainment rate in the tropical Atlantic. Independent from Jones and Mulhearn (1983), Csanady (1995) later suggested a practical formula for the entrainment rate aimed for the tropical ocean: the rate of turbulence energy production is the stress × rate of strain, which he supposed proportional to the surface wind stress × the stress at the mixed layer base. A fraction of this turbulence energy is reconverted into mean potential energy. Therefore, the potential energy gain associated with entrainment is

$$w_e g' = \gamma \frac{u^{*2} |\triangle u|}{H}, \tag{3}$$

with γ as an entrainment coefficient, the efficiency of energy conversion.

4 Model Development and Requirements

In order to develop a simple model suited for modeling the tropical ocean dynamics, the formulation of some previous tropical ocean models are reviewed here.

Cane (1979) developed a simple numerical model to study the wind driven equatorial circulation. The model was a fully nonlinear time dependent two-layer model that included a mixed layer of constant depth and a thermocline layer below. No additional equation was required to estimate the turbulent mixing rate at the interface. Instead, it was determined strictly from the momentum divergence of the mixed layer only. The density was constant in both layers, therefore, the vertical mixing did not change the thermal properties in either layers.

Cane's (1979) model provided a framework for later tropical ocean model studies, since it was the first model which accounted for equatorial entrainment and also contained all the major components of the equatorial circulation system including the Equatorial Undercurrent. However, the major problem was that the model was incapable of predicting the mixed layer temperature. In order to overcome this deficiency, Schopf and Cane (1983) proposed a new reduced gravity model that included active thermodynamics, thereby allowing the temperature of the mixed layer to vary. The model included the upper two layers in which the second layer had a linear stratification. The entrainment (and detrainment) rate was determined from the Kraus and Turner's (1967) model, where wind stress is the only source for turbulent mixing. The model was tested with constant easterly winds in a closed basin. The mixed layer near the equator quickly reached a minimum depth and the entrainment rate was

determined by the momentum divergence of the mixed layer thereafter. Eventually, the water accumulated in the mixed layer outside the equatorial region, giving a clue that the Kraus and Turner's model is not adequate for parameterizing the equatorial mixing process.

The model developed by Schopf and Cane (1983) was further extended by Gent and Cane (1989) who included more vertical structure in the second layer. The model was basically identical to that of Schopf and Cane (1983) except that the second layer was divided into an arbitrary number of numerical layers. The diapycnal mixing between these layers was determined by the initial depth ratio among these numerical layers. This artificial procedure was required in order to avoid outcropping of individual layers. This model was further used by Gent (1991) and Chen *et al.* (1994).

More recently, McCreary and Yu (1992) used a numerical model with two and a half layers similar to that of Schopf and Cane (1983) to develop a simple model of steady state equatorial circulation. The entrainment (and detrainment) rates were calculated strictly from the mixed layer thickness. The escape of warm water mass was modeled by the detrainment process; therefore, the heat flux into the second layer during the detrainment process had to be removed by an artificial cooling term. Later, McCreary *et al.* (1993) included a fossil layer in the McCreary and Yu's model in order to simulate the seasonal thermocline dynamics in the Indian Ocean. Again, an artificial cooling term was required to cool off the heat gain in the thermocline layer during the detrainment process.

Philander and Pacanowski (1986), on the other hand, used the general circulation model of Bryan (1969) with a very high resolution (0.3° in horizontal and 27 levels in vertical). The vertical heat flux in the interior was parameterized by eddy heat diffusion. Inadequacies of this mixing parameterization resulted in the decay of the

thermocline. The model results were, therefore, valid only within a few years.

From the success and failure of the models discussed above, we may able to conclude the following: (1) Schopf and Cane (1983) model is ideally suited for the goal of this study, since it contains most of essential components of the tropical dynamics; (2) For the tropical ocean problem, the Kraus and Turner (1967) model is not appropriate in determining the entrainment rate; therefore, the mean shear effect should be included. The mixed layer models suggested by Csanady (1994) and Jones and Mulhearn (1983) appear to be the best candidates; and (3) The detrainment process is not essential in the simple tropical ocean model and must be avoided. Therefore, open boundaries must be placed somewhere between the equatorial cell and subtropics where the detrainment process may become important.

5 Model Formulation

5.1 Governing Equations

Consider an ocean consisting of two active layers including a surface mixed layer and a thermocline layer as illustrated in Figure 13. The deep fluid below the thermocline layer is assumed to be stagnant (the reduced gravity approximation; see Cushman-Roisin (1994) for in-depth discussion). Let the longitude and latitude be given by ϕ and θ, respectively, then the depth integrated momentum, continuity and heat conservation equations for the mixed layer are:

$$\frac{\partial(u_1h_1)}{\partial t} + \frac{1}{a\,cos\theta}\frac{\partial}{\partial\phi}(u_1^2h_1) + \frac{1}{a}\frac{\partial}{\partial\theta}(u_1v_1h_1) - 2\frac{u_1v_1h_1}{a}tan\theta - 2\Omega sin\theta v_1h_1 = \frac{-h_1}{\rho_1 a\,cos\theta}\frac{\partial p_1}{\partial\phi} + \frac{\tau^{(\phi)}}{\rho_1} + w_e u_2 - K(u_1 - u_2) + F_{1\phi} \quad (4)$$

$$\frac{\partial(v_1h_1)}{\partial t} + \frac{1}{a\,cos\theta}\frac{\partial}{\partial\phi}(u_1v_1h_1) + \frac{1}{a}\frac{\partial}{\partial\theta}(v_1^2h_1) + \frac{(u_1^2 - v_1^2)h_1}{a}tan\theta + 2\Omega sin\theta u_1h_1 = \frac{-h_1}{\rho_1 a}\frac{\partial p_1}{\partial\theta} + \frac{\tau^{(\theta)}}{\rho_1} + w_e v_2 - K(v_1 - v_2) + F_{1\theta} \quad (5)$$

$$\frac{\partial h_1}{\partial t} + \frac{1}{a\,cos\theta}\{\frac{\partial u_1h_1}{\partial\phi} + \frac{\partial}{\partial\theta}(v_1h_1\,cos\theta)\} = w_e, \quad (6)$$

$$\frac{\partial T_1}{\partial t} + \frac{u_1}{a\,cos\theta}\frac{\partial T_1}{\partial\phi} + \frac{v_1}{a}\frac{\partial T_1}{\partial\theta} = \frac{Q}{\rho C_{pw}h_1} - \frac{w_e}{h_1}(T_1 - T_2) + K_h\nabla^2 T_1, \quad (7)$$

and for the thermocline layer:

$$\frac{\partial(u_2h_2)}{\partial t} + \frac{1}{a\,cos\theta}\frac{\partial}{\partial\phi}(u_2^2h_2) + \frac{1}{a}\frac{\partial}{\partial\theta}(u_2v_2h_2) - 2\frac{u_2v_2h_2}{a}tan\theta - 2\Omega sin\theta v_2h_2 = \frac{-h_2}{\rho_2 a\,cos\theta}\frac{\partial p_2}{\partial\phi} - w_e u_2 + K(u_1 - u_2) + F_{2\phi} \quad (8)$$

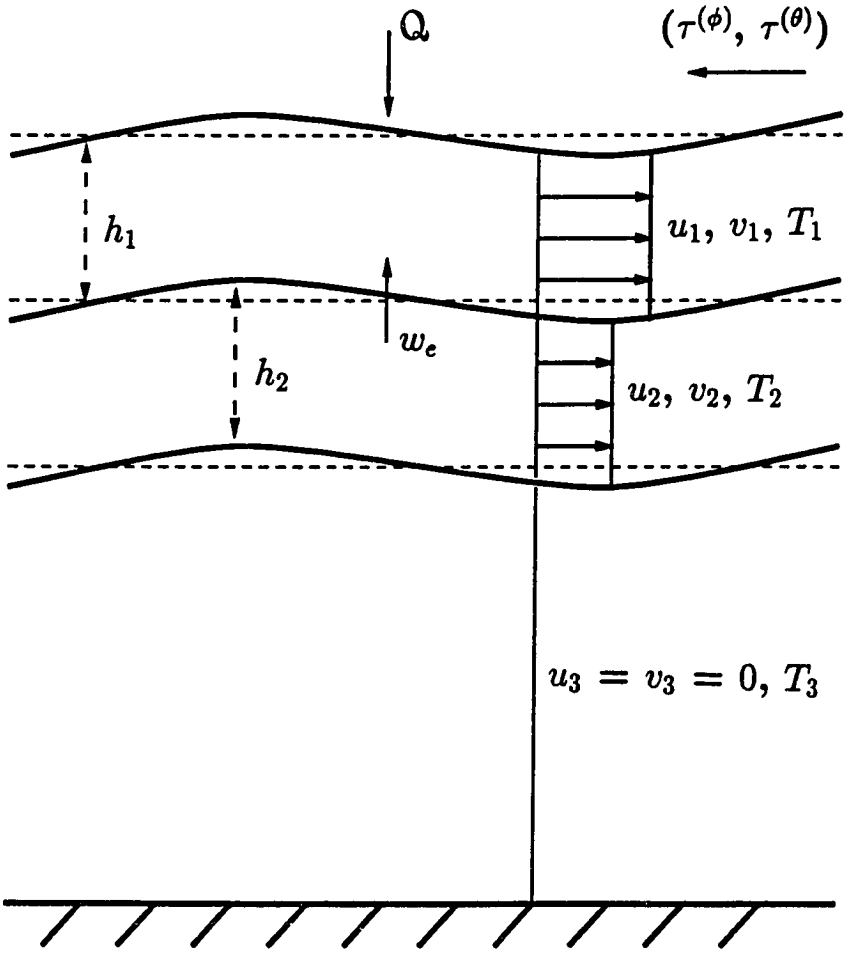

Figure 13: The model configuration and the vertical structure of temperature and velocity assumed in the model equations.

$$\frac{\partial(v_2h_2)}{\partial t} + \frac{1}{a\,cos\theta}\frac{\partial}{\partial\phi}(u_2v_2h_2) + \frac{1}{a}\frac{\partial}{\partial\theta}(v_2^2h_2) + \frac{(u_2^2 - v_2^2)h_2}{a}tan\theta + 2\Omega sin\theta u_2h_2$$
$$= \frac{-h_2}{\rho_2 a}\frac{\partial p_2}{\partial\theta} - w_e v_2 + K(v_1 - v_2) + F_{2\theta} \quad (9)$$

$$\frac{\partial h_2}{\partial t} + \frac{1}{a\,cos\theta}\{\frac{\partial u_2h_2}{\partial\phi} + \frac{\partial}{\partial\theta}(v_2h_2\,cos\theta)\} = -w_e, \quad (10)$$

$$\frac{\partial T_2}{\partial t} = 0, \quad (11)$$

where the horizontal friction terms for j-th layer are (Gill, 1982)

$$F_{j\phi} = A_h h_j(\nabla^2 u_j - \frac{u_j}{a^2cos^2\theta} - \frac{2sin\theta}{a^2cos^2\theta}\frac{\partial v_j}{\partial\phi}), \quad (12)$$

$$F_{j\theta} = A_h h_j(\nabla^2 v_j - \frac{v_j}{a^2cos^2\theta} + \frac{2sin\theta}{a^2cos^2\theta}\frac{\partial u_j}{\partial\phi}). \quad (13)$$

Based on the hydrostatic relation, the pressure gradient terms are given by

$$\nabla p_1 = g\alpha\nabla\{h_1(T_1 - T_3) + h_2(T_2 - T_3)\} - {}^1\!/_2 g\alpha h_1\nabla T_1, \quad (14)$$

$$\nabla p_2 = g\alpha\nabla\{(h_1 + h_2)(T_2 - T_3)\}, \quad (15)$$

where the buoyancy is calculated only from a linear thermal expansion for simplicity. The entrainment rate is determined in a manner similar to that in the Csanady (1995) model, except for the addition of a background dissipation term (Kim, 1976):

$$w_e = \gamma\frac{u^{*2}|\,\triangle u\,|}{g'H} - \frac{2\epsilon_o}{g'}, \quad (16)$$

where γ is the entrainment coefficient, u^{*2} is the surface stress and $\triangle u$ is the mean shear at the mixed layer floor. If the entrainmant rate becomes negative, it is fixed as zero.

The symbols used in Eqns. (4)-(16) are:

u_j,v_j : zonal and meridional components of velocity for layer j;

h_j : thickness of layer j;

T_j : temperature of layer j;

g : acceleration of gravity;

α : thermal expansion coefficient;

ρ_j : density of layer j;

p_j : pressure of layer j;

a : radius of the Earth;

Ω : angular velocity of rotation of the earth;

$\tau^{(\phi)}$,$\tau^{(\theta)}$: zonal and meridional components of wind stress;

w_e : entrainment velocity across the interface;

A_h : Laplacian mixing coefficient for momentum;

K_h : Laplacian mixing coefficient for heat;

K : interfacial friction parameter;

Q : heat flux at the sea surface; and

C_{pw} : specific heat of water.

5.2 Surface Heat Flux

The formula for thermal heat flux is based on the heat budget of the ocean (Fleagle and Businger, 1980), which can be written by

$$Q = Q_{SW} - Q_{LW} - Q_S - Q_E, \tag{17}$$

where Q is the net heat flux, Q_{SW} is the incoming short wave radiation, Q_{LW} is the back radiation (positive upward), Q_S is the sensible heat flux, and Q_E is the latent heat flux of evaporation. The bulk formula of sensible heat flux is:

$$Q_S = \rho_a C_{pa} D_s |V|(T_1 - T_a), \tag{18}$$

where ρ_a is the density of air, C_{pa} is the specific heat of air, T_a is the air temperature, D_s is the dimensionless constant for heat conduction (or Stanton number), and $|V|$ is

the wind speed. The formula for the latent heat flux of evaporation (Haney, 1971) is

$$Q_E = \rho_a D_d L |V| [e_s(T_1) - \varrho e_s(T_a)](0.622/P_a), \tag{19}$$

where P_a is the atmospheric pressure (in mb), L is the latent heat of evaporation per unit mass, D_d is the dimensionless constant for evaporation (or Dalton number), ϱ is the relative humidity (dimensionless), and $e_s(T_1)$ and $e_s(T_a)$ are saturation vapor pressure at the sea surface and air (10 m above sea surface), respectively. The saturation vapor pressure (in mb) for temperature between $\pm$ 40°C can be parameterized (Gill, 1982) by

$$log_{10} e_s(T) = \frac{(0.7859 + 0.03477T)}{(1 + 0.00412T)}. \tag{20}$$

The forcing variables (Q_{SW}, Q_{LW}, $|V|$, T_a) are obtained from Esbensen and Kushnir (1981). The cubic spline interpolation is applied to the twelve monthly means of the data in order to match the model grid system (from 5° interval to 1°). Then this interpolated data are decomposed into five Fourier harmonics (12,6,4,3,2.4 month periods) in time to provide a continuous time series for the model integration.

5.3 Model Geometry

The model covers the tropical Atlantic Ocean and some portion of the subtropical oceans of both hemispheres from 20°S to 20°N and 90°W to 20°E as shown in Figure 14. The northern and southern boundaries are open. The caribbean islands are all removed from the model geometry for simplicity. The model domain is not extended further poleward in order to avoid the detrainment process.

5.4 Numerical Formulation

The model equations (4)-(11) are discretized in space on the Arakawa C-grid scheme. The numerical scheme is the mass and energy conserving Lilly (1965) scheme

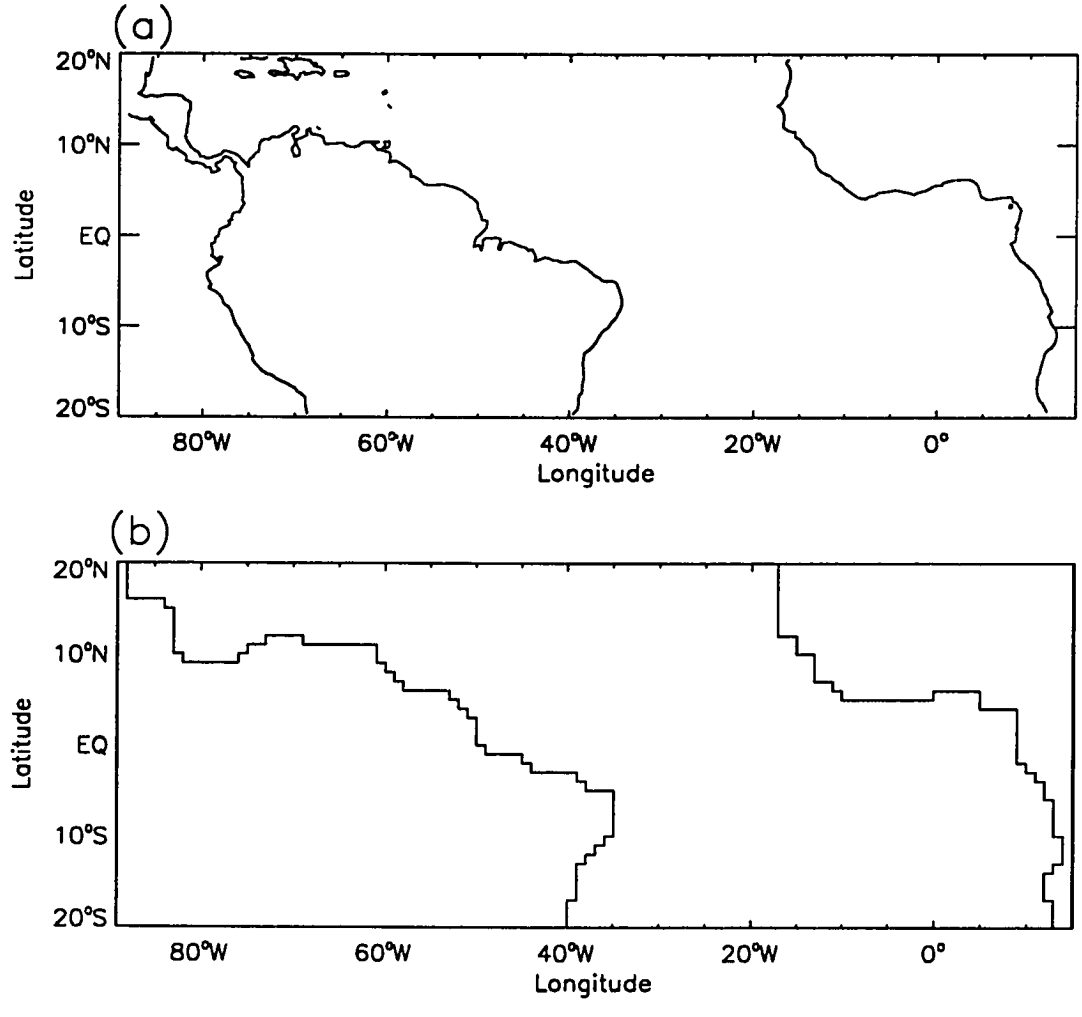

Figure 14: (a) Actual and (b) model geometries. The northern and southern boundaries are opened, and all remaining boundaries are solid walls.

(C-scheme according to Grammeltvedt ,1969), with an exception of the Coriolis terms. Holland and Lin's (1975) scheme is used for the Coriolis term. The grid size is 1^o in both horizontal directions; therefore, the model domain contains 121×41 grid points per layer for each variables. The leap-frog time integration scheme is used with a time step of about one hour. The Shuman (1957) averaging scheme is applied twice consecutively every 40 time steps to remove the computational mode produced by the leap-frog scheme as suggested by Killworth (1984).

5.5 Boundary Conditions

At the wall boundaries, a no-slip boundary condition is applied. For the two openings at 20°N and 20°S, Orlanski's (1976) radiation condition is used for u, v and h variables in an implicit form suggested by Chapman (1985). For temperature variable T, a no-flux condition is applied at all walls and open boundaries. In order to account for the realistic heat flux through the open boundaries, two narrow zonal sponge layers are specified from 15^o to 20^o in both hemispheres. The mixed layer temperature is, therefore, relaxed back to the surface temperature data of Levitus (1983) inside the sponge layers (e-folding time scale of about 25 days). For the stability at the open boundaries, one-dimensional Hensen (1962) filter is applied every 40 time steps to the two rows nearest to the open boundaries for u, v and h. In addition, the mixing coefficients, A_h and K for u_j, increase linearly inside the sponge layers from 15^o to 20^o. There is no corresponding treatment on v_j so that the fluid can pass freely across the open boundaries. To allow realistic mass exchanges through the open boundaries (similar to the idea of thermal sponge layers) the layer depths are slowly relaxed back to the initial depth profile inside the narrow sponge layers (e-folding time scale of about 250 days). This scheme will provide the mass restoring mechanism during the model intergration. A similar procedure was employed previously by Jensen (1990)

on the numerical simulation of the Somali current.

5.6 Wind Forcing over Tropical Atlantic Ocean

The model is forced by a climatological monthly mean wind stress of Hellerman and Rosenstein (1983). Similar to the heat flux variables, the cubic spline interpolation is applied to the twelve monthly means of wind stress data in order to match the model grid system (from 2^o interval to 1^o). Then they are decomposed into five Fourier harmonics (12,6,4,3,2.4 month periods) in time to provide a continuous time series for the model integration.

The monthly averaged wind stress and its curl over the tropical Atlantic Ocean are reproduced from Hellerman and Rosenstein (1983) in Figures 15 and 16, respectively. Associated with the movement of the ITCZ, the seasonal variation of tropical wind stress is highly concentrated inside the zonal band between 2°N and 10°N (Servain and Legler, 1986). The wind stress inside this zonal band is relatively strong during northern summer and its curl changes sign from positive to negative between April and August. It is noticeable that the wind stress pattern exhibits a significant variation in zonal direction as well as in meridional direction. The wind stress is stronger and generally zonal in the western equatorial region, while the eastern side is dominated by the meridional wind.

The parameter values used for the model integration are listed in Table 2. Unless specified otherwise, the values in Table 2 are all constant during the model integration.

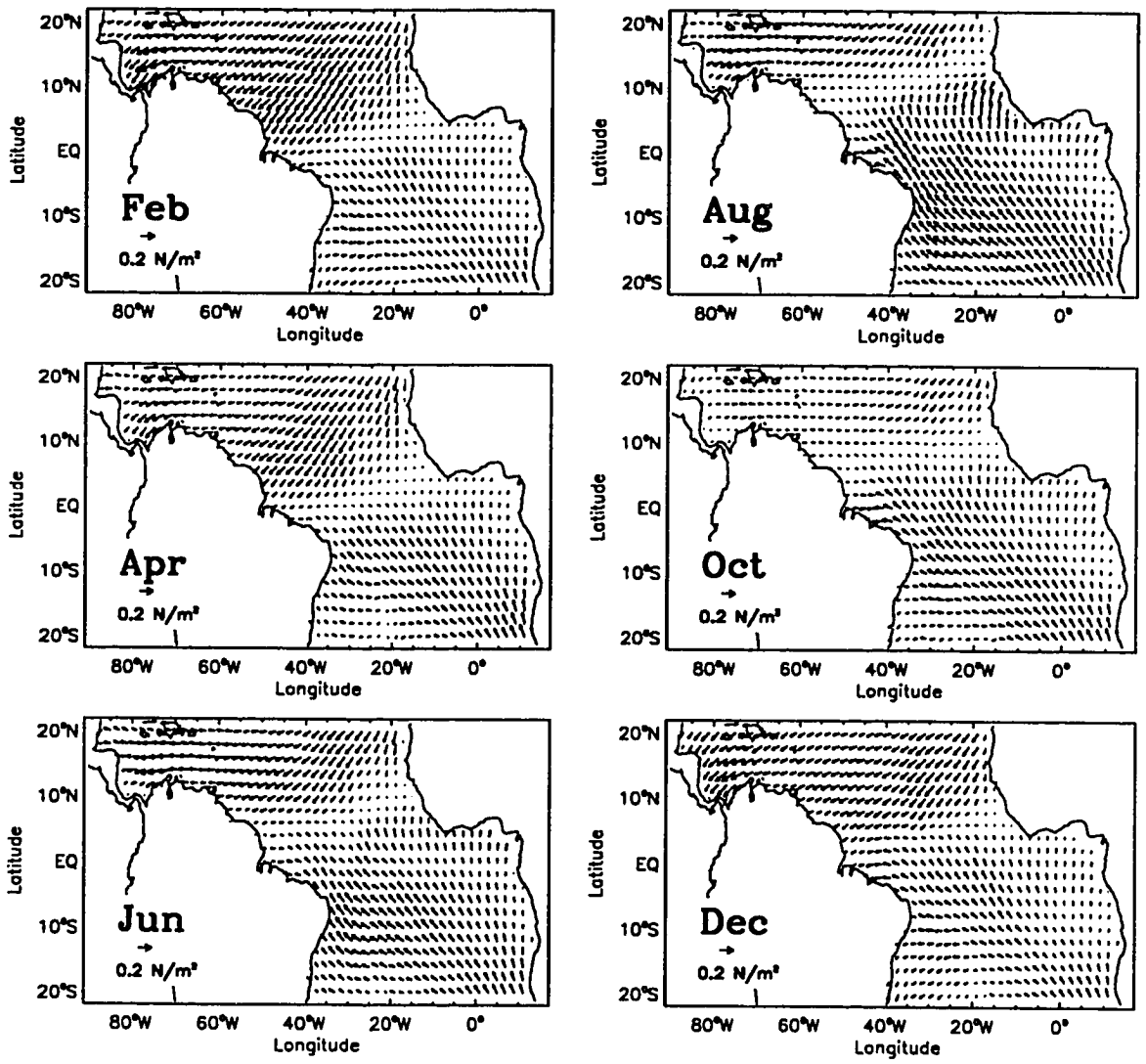

Figure 15: Monthly mean wind stress vectors from February to December (in unit of N/m^2). Reproduced from Hellerman and Rosenstein (1983).

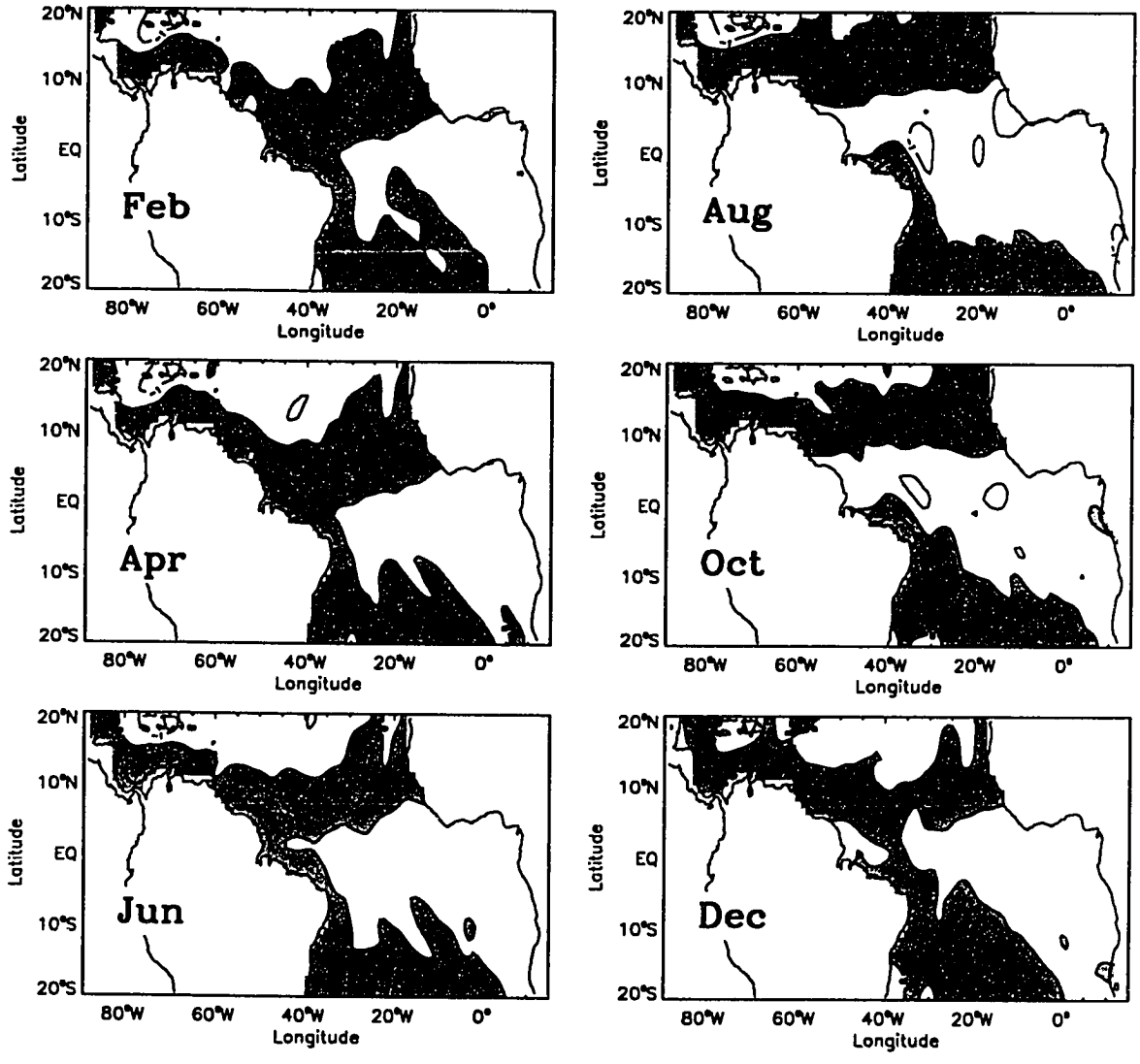

Figure 16: Monthly mean wind stress curls from February to December (in unit of N/m^3). Positive wind stress curl is shaded. Reproduced from Hellerman and Rosenstein (1983).

Parameter	Notation	Value
H_1	Initial thickness of the layer 1	50m
H_2	Initial thickness of the layer 2	150m
T_1	Initial temperature of layer 1	25.7°C
T_2	Temperature of layer 2	20°C
T_3	Temperature of layer 3	10°C
α	Thermal expansion coefficient	$0.00025°C^{-1}$
A_h	Laplacian mixing coefficient for momentum	$3500m^2/s$
K_h	Laplacian mixing coefficient for heat	$3500m^2/s$
K	Interfacial friction parameter	$8\times10^{-7}s^{-1}$
C_{pw}	Specific heat of water	$4200J\cdot Kg^{-1}{}^oC^{-1}$
C_{pa}	Specific heat of air	$1004J\cdot Kg^{-1}{}^oC^{-1}$
P_a	Atmospheric pressure at 10m from sea level	1013mb
ρ_a	Air density	$1.2Kg/m^3$
ϱ	Ralative humidity (dimension less)	0.8
L	Latent heat of evaporation per unit mass	$2.49\times10^6J\cdot Kg^{-1}$
D_s	Stanton number (dimension less)	1.5×10^{-3}
D_d	Dalton number (dimension less)	1.5×10^{-3}
γ	entrainment coefficient	1/12
ϵ_o	background dissipation of entrainment	7.5×10^{-9} m^2/s^3

Table 2: A list of parameters used for the model integration.

6 Model Results and Discussion

The model was integrated from rest and run for about 15 years, at which time it reached a quasi-periodic state. This was determined by the fact that the model attained a quasi-periodic cycle in kinetic energy, as well as mass and heat budget. The results described here are based on the 16th year of the model simulation.

6.1 Annual Mean Mass and Heat Budget

Figure 17 shows schematic diagrams of the annual mean mass and heat transports integrated zonally along 8°S and 8°N. The upper and lower bars represent the mixed and thermocline layer transports, respectively. The upward adn downward arrows indicate the vertical transport via the equatorial entrainment and the surface heat flux, respectively. The total meridional transport at each latitude is indicated at the bottom of the figures. For better comparison with previous studies, the southward transport of North Atlantic Deep Water (NADW) required to balance the net northward mass transport of the upper ocean is included in Figure 18. In order to estimate the total heat transport, a mean temperature of 7.5°C is assumed for the NADW. Associated new total transport is indicated at the bottom of these figures.

These figures illustrate that 10 Sv of thermocline water enters the equatorial cell, with roughly 9 Sv, about 90 % of the total input, coming from the South Atlantic and the rest 1 Sv from the North Atlantic. This 10 Sv of upper thermocline water is entrained in the surface mixed layer. This water then joins 1 Sv of surface water

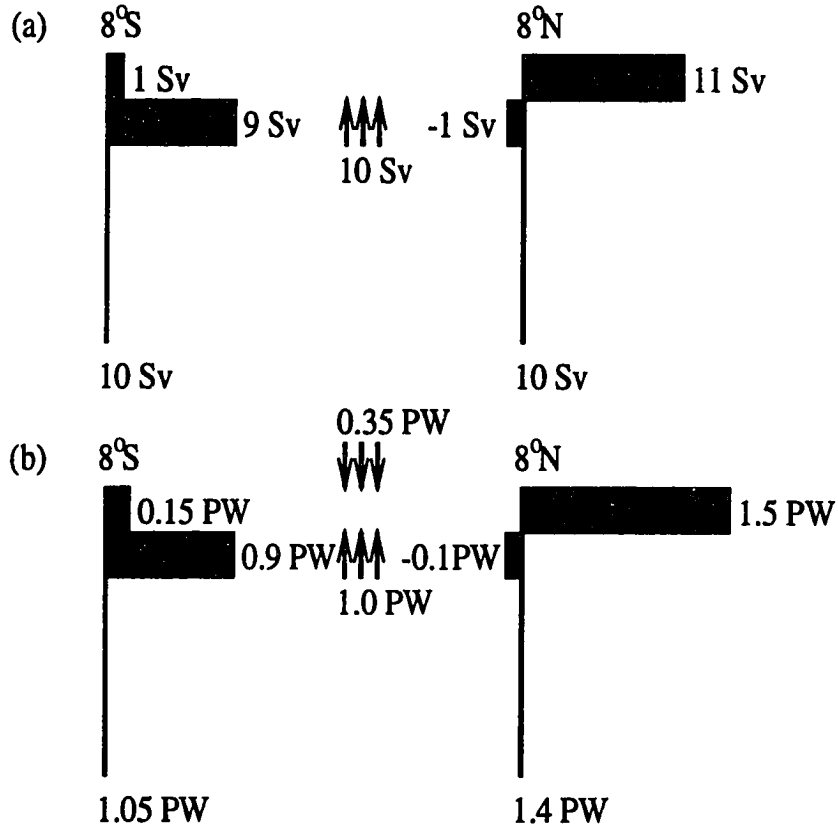

Figure 17: Annual mean (a) mass (in Sv) and (b) heat (in PW) transports across 8°S and 8°N. The upper and lower bars represent the mixed and thermocline layer transports respectively, with northward transports to the right of the zero line.

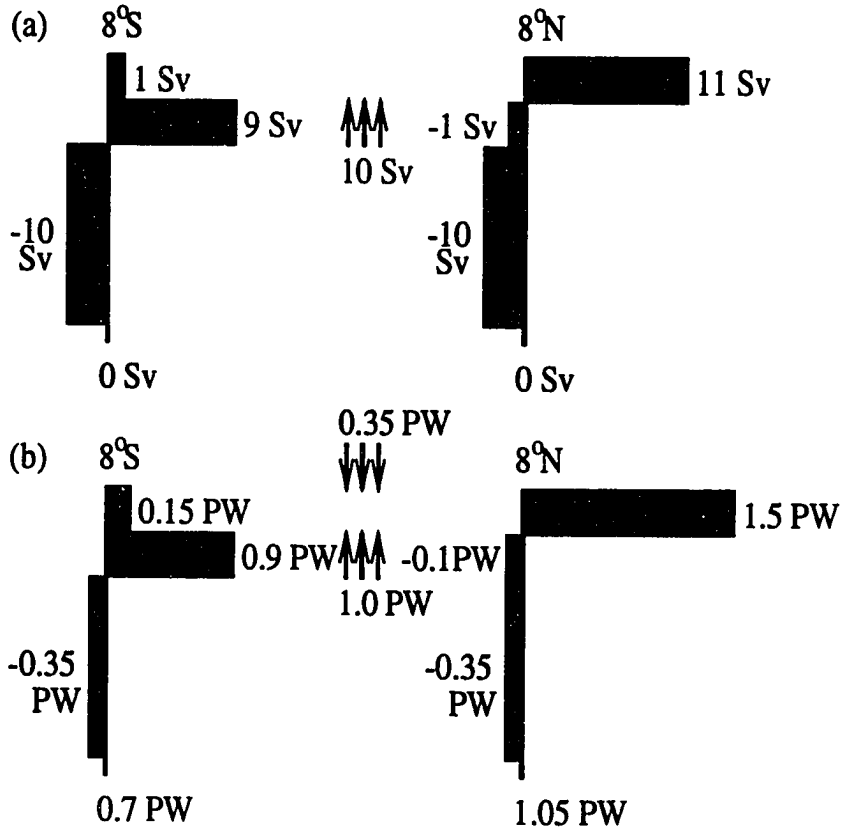

Figure 18: As in Figure 17 but with the NADW transport.

from the South Atlantic and flows into the North Atlantic across the equator. The estimate of the absolute and the relative transport scales are in good agreement with observations (*e.g.*, Roemmich, 1983).

In Figure 17(a) and (b) it is noted that the heat flux across a given surface is almost proportional to the mass flux. The reason is that the temperature variation is far smaller than the space-averaged temperature (Philander and Pacanowski, 1986). Even though the heat transport closely follows the mass transport, some features of the heat transport pattern in Figure 17(b) are still worth while to be explored. In the thermocline layer, about 0.9 PW (10^{15}W) of heat is transported to the tropical cell across 8°S from the South Atlantic. A total of 1.0 PW of heat is transferred to the surface mixed layer via the equatorial entrainment. This cold entrained water then gains about 0.35 PW of heat at the sea surface (warm water formation) and is carried away to the subtropical ocean in the North Atlantic. There are additional heat gains from the surface water of the South Atlantic (0.15 PW) and from the thermocline water of the North Atlantic (0.1 PW), but their contributions are not significant. Therefore, taking the NADW transport (−0.35 PW) into account, the total heat transports are 0.7 PW at 8°S and 1.05 PW at 8°N. The heat deficit between the two latitudes is added from the surface heat flux (0.35 PW). The total heat transport is in good agreement with the GCM study of Philander and Pacanowski (1986); however, it underestimates the heat transport values obtained by the inverse calculation of Roemmich (1983). He estimated about 0.74 PW and 1.61 PW at 8°S and 8°N, respectively, thereby a net heating of 0.87 PW at the sea surface. It must be noted, however, that not all estimates of heat transports in the tropical Atlantic are consistent with each other. For instance, using the heat budget equation, Hastenrath (1980) obtained about 1.25 PW and 1.5 PW at 10°S and 10°N, respectively, hence a net surface heating of 0.25 PW between the two latitudes. But, using the same method, Hsiung (1985) estimated 0.2 PW and 0.8 PW at 10°S and 10°N, respec-

tively. Therefore, it is not clear whether the model underestimated the heat transport values or not. Nevertheless, the model result roughly falls inside the range between Hastenrath (1980) and Hsiung's (1985) estimations.

Figure 19 shows the two-dimensional mass transport vectors for both mixed and thermocline layers. The vertical mass flux rate between the two layers is also shown in Figure 19(c). These figures illustrate that the thermocline waters enter the model domain from the southeastern corner, cross the South Atlantic via the northern leg of the subtropical gyre, and then turn northward and feed the Equatorial Undercurrent. These cold thermocline waters are then entrained at the central and eastern parts of the equator and transported to the west by the South Equatorial Current, thus escaping the equatorial region via the NBC. In turn, the NBC bifurcates into the Guiana Current and the NECC. The Guiana Current continues northwestward along the western boundary. The NECC, on the other hand, joins the NEC via the cyclonic gyre located between the NECC and the NEC. Eventually, both branches join at the western boundary near 12°N and escape the model domain through the Caribbean Current. It is evident from Figure 19(b) that the subsurface subtropical waters of the North Atlantic hardly contribute to the Equatorial Undercurrent. The major route and the scale of the mass transport inside the tropical cell agree well with the schematic pictures presented by Csanady (1987; 1990) and Gouriou and Reverdin (1992).

6.2 Seasonal Cycle of Mass and Heat Budget

The tropical Atlantic is subject to unusually high seasonal variation presumably associated with the seasonal excursion of ITCZ. Therefore, in this section, we investigate the seasonal cycle of the mass and heat budget from the model results focusing on the budget near the equatorial region.

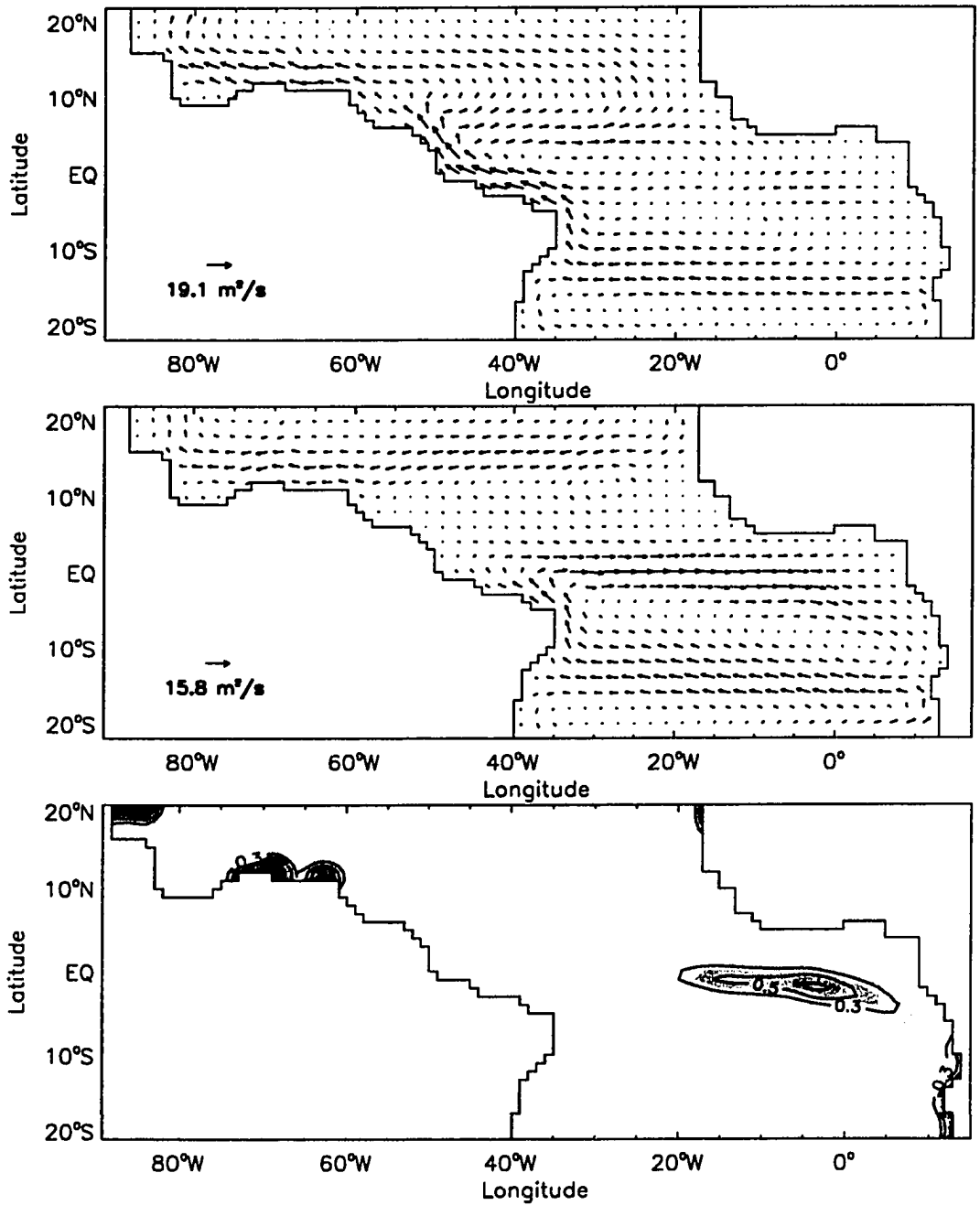

Figure 19: Annually averaged mass transport in (a) the mixed layer and (b) the thermocline layer (in m^2/s) . (c) Annual mean entrainment rate (in $10^{-5}m/s$)

Equatorial Entrainment

Before we examine the model results, it is important to point out that the underlying assumption behind our entrainment formulation is different from those of previous tropical ocean models. Most tropical ocean models suffer from the lack of proper representation of the vertical turbulent mixing process. It is usually assumed that the entrainment velocity is proportional to the inverse of the mixed layer depth (*e.g.*, McCreary and Yu, 1992). Among others, the Kraus and Turner (1969) scheme may be the most widely used turbulent mixing parameterization. However, as demonstrated by Schopf and Cane (1983), the major drawback of this scheme is its lack of shear generated turbulent mixing, which may be the major mechanism of equatorial entrainment (Voituriez and Herbland, 1977; Csanady, 1995). Therefore, in this study, we scale the intensity of the entrainment rate by wind stress and the mean shear at the base of the mixed layer, based on the studies of Csanady (1995) and Jones and Mulhearn (1983). (See Eqn. 17 for exact formulation).

Figure 20 shows the entrainment rate for February, April, June, August, October and December. The entrainment rate near the equator is nearly zero between February and April. The entrainment suddenly starts around May at the equator east of 10°W. Within a month, it quickly extends toward the central basin up to 25°W. Shortly after it reaches its peak ($\sim 1.2\times10^{-5}$m/s) in June, the entrainment rate starts to reduce and its center moves back toward the eastern basin. It appears that the entrainment lasts until December and dies out only in January. A prominent feature is that the entrainment is limited to in the central and eastern basin where the mixed layer depth is relatively shallow. It is noticeable that the center of the entrainment is located slightly southward of the equator around 1°S $\sim$ 2°S, especially since the eastern end is tilted much more toward the south and sometimes connected to the coastal entrainment zone off the west coast of the South Africa in the South

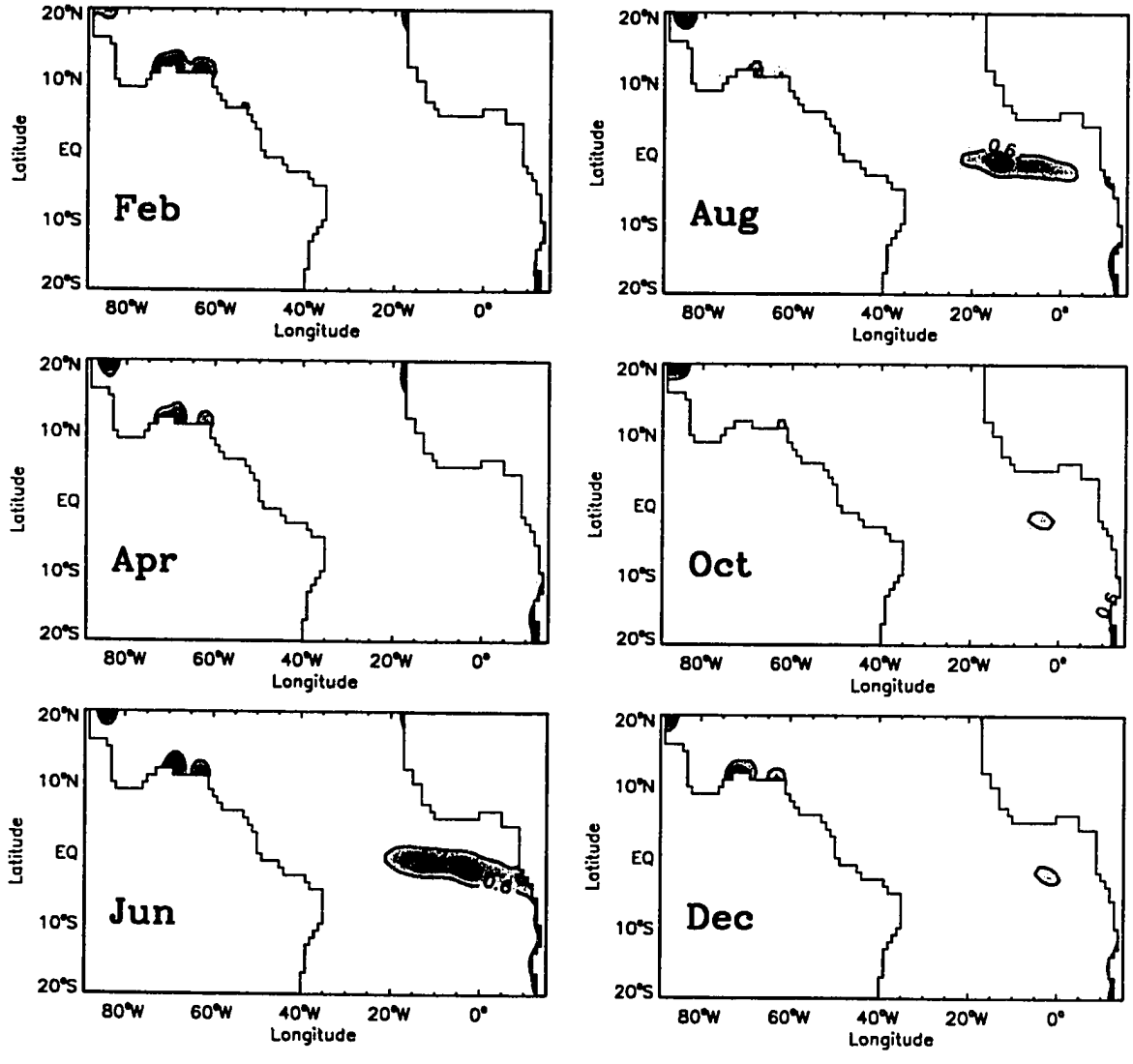

Figure 20: Monthly averaged entrainment rate from February to December from the model results. The unit is 10^{-5}m/s.

Atlantic.

Although controversial in many respects, the most widely accepted hypothesis on the cause of the equatorial entrainment is the remote forcing hypothesis of Moore *et al.*, (1978). The physical basis is that when the Kelvin wave trough, transmitted from the western part of the equator due to the increased zonal wind stress, reaches the eastern basin, the cold subsurface water is brought closer to the surface, thus it is easier to mix across the mixed layer base.

However, it appears that the zonal wind stress pattern in the west shown in Figure 21 does not match with the entrainment signal in the east. The zonal wind stress in the west increases during June/September, but the entrainment in the east starts much earlier in May. Therefore, it is hard to imagine any dynamical connection between the wind stress anomaly in the west and the entrainment in the east. It appears that the source of this confusion originates from a notion that the equatorial entrainment rate can be identified by the intensity of the cold water tongue, which is coldest in August and not in June (Figure 21(c)). To fully understand this connection between the variations of the SST and the entrainment rate, the examination of the mixed layer heat budget is required. The heat budget of the mixed layer is investigated in chapter 6.3.

Based on the model results obtained here, we concluded in following manner: during February/April, the ITCZ is located slightly northward of the equator in the east of 30°W, forming a region of weak zonal wind stress near the equator. Therefore, the strength of the SEC and the EUC are also very weak, thereby low shear at the mixed layer base. In these months, the weak wind stress and shear allows no significant entrainment. As the ITCZ migrates northward from May, the zonal wind stress near the equator is increased, which speeds up the westward-flowing SEC and pushes more WWM into the western basin creating a mass divergence in the east.

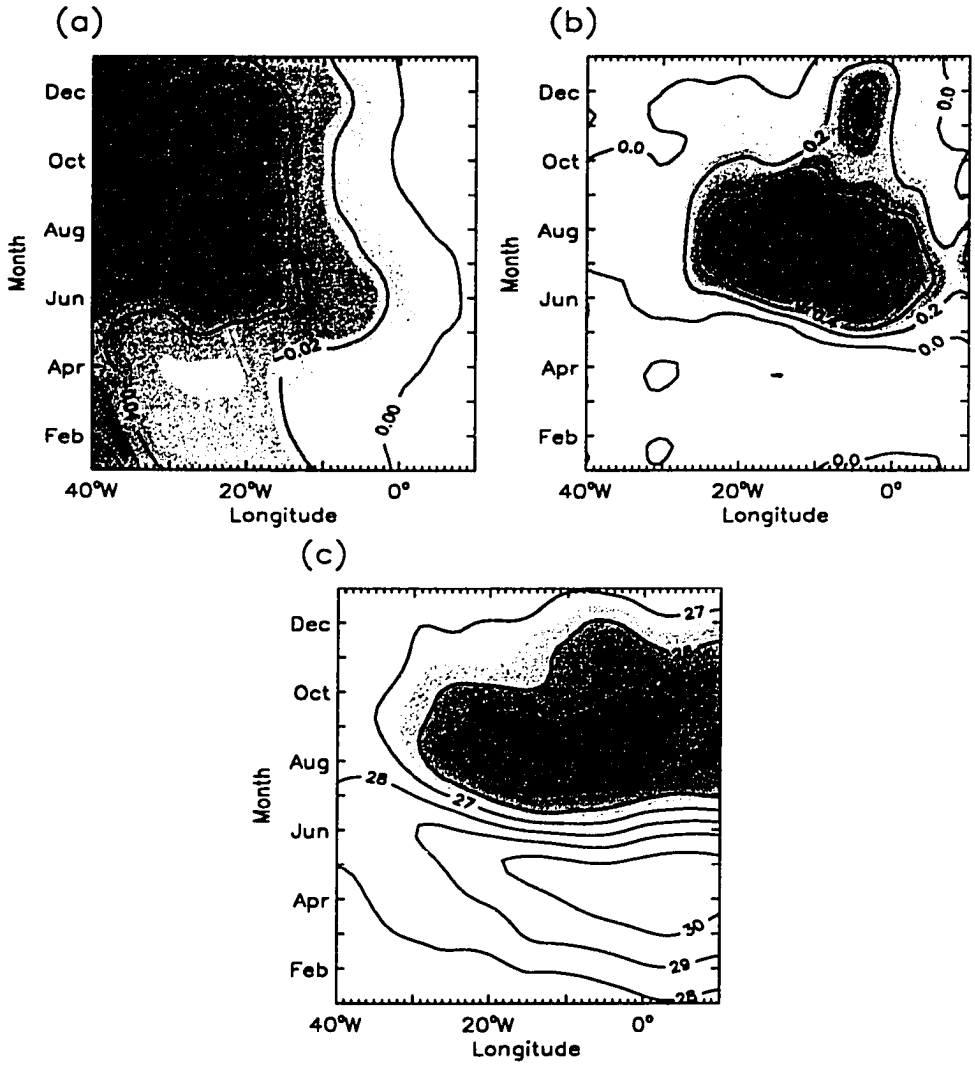

Figure 21: The time-longitude plots of (a) the zonal wind stress (N/m^2) from Hellerman and Rosenstein (1983), (b) the entrainment rate ($10^{-5}m/s$) and (c) the SST (^oC) all averaged between 2^oS and 2^oN.

An additional pressure gradient is then set up below the mixed layer, which in turn increases the speed of the EUC. Consequently, the shear between the mixed layer and the upper thermocline layer increases until the zonal wind stress is relaxed. During May/October, the enhanced wind and shear, together with the shallow mixed layer depth in the eastern basin, generate Kelvin-Helmholdz type instability, which grows into a fully developed turbulence. This is verified by Figure 22 which shows a very high correlation between the zonal wind stress east of 30°W and the interfacial shear. The inverse of the mixed layer depth is also shown in Figure 22(c). The figure shows that this signal is particularly correlated with the entrainment signal east of 0°.

SEC and NECC

Previously, it was shown that the escape of the WWM takes place predominantly toward the north of the equator. It is therefore vital to investigate the behavior of the NBC in order to fully describe the seasonal mass budget of the upper tropical Atlantic Ocean. Before we examine the NBC however, it is necessary to understand the seasonal cycle of the SEC and the NECC, since these two current systems are strongly coupled with the NBC, the major route of the WWM escape.

Figure 23 shows the bimonthly map of the mixed layer mass transport from February to December. The transports are averaged monthly; therefore, the eddy transports are mostly averaged out. Two distinctive branches of the SEC are observed. The first branch is located at the equator and the second near 10°S. Hereafter, these branches are referred to as the equatorial branch of the SEC (ESEC) and the southern branch of the SEC (SSEC), respectively.

The SSEC is the northern leg of interior subtropical gyre in the South Atlantic. It carries the surface water westward toward the east coast of South America. When

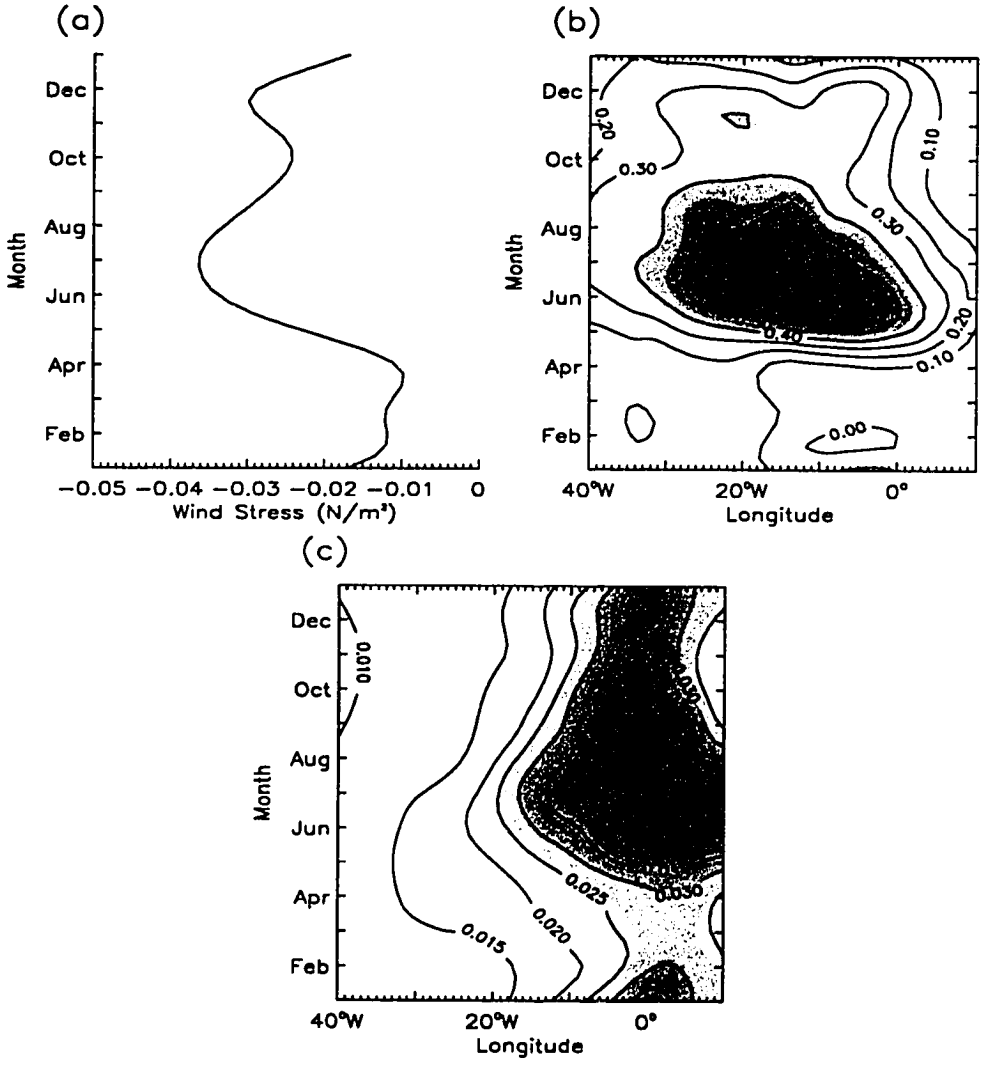

Figure 22: (a) The zonal wind stress averaged between 30°W and 10°E (N/m^2). The time-longitude plots of (b) the interfacial shear at the mixed layer base (m/s) and (c) the inverse of the mixed layer depth (m^{-1}). The (a),(b) and (c) are all averaged between 2°S and 2°N.

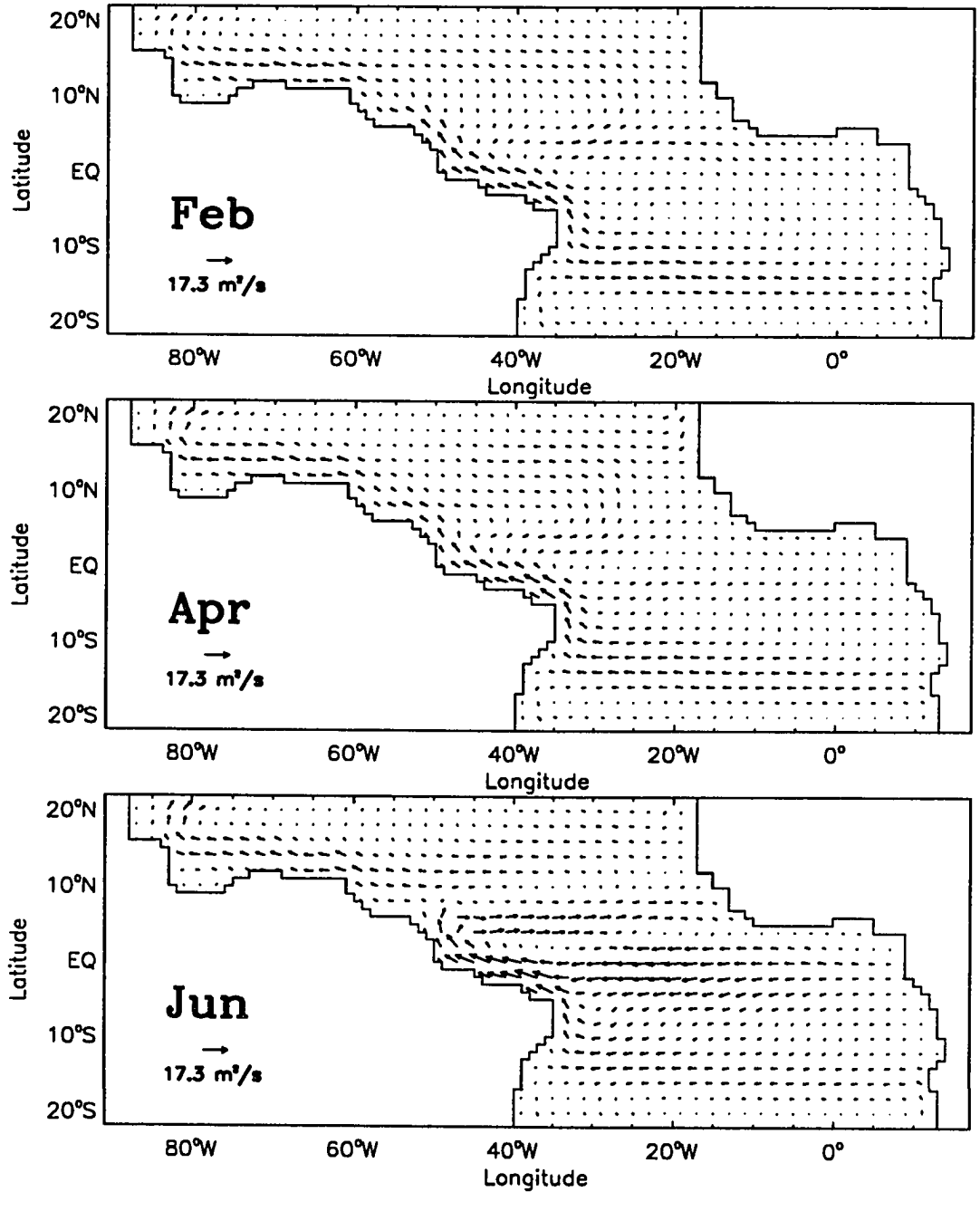

Figure 23: Monthly averaged mass transport in the mixed layer from February to December inferred from the model result. The unit is m/s.

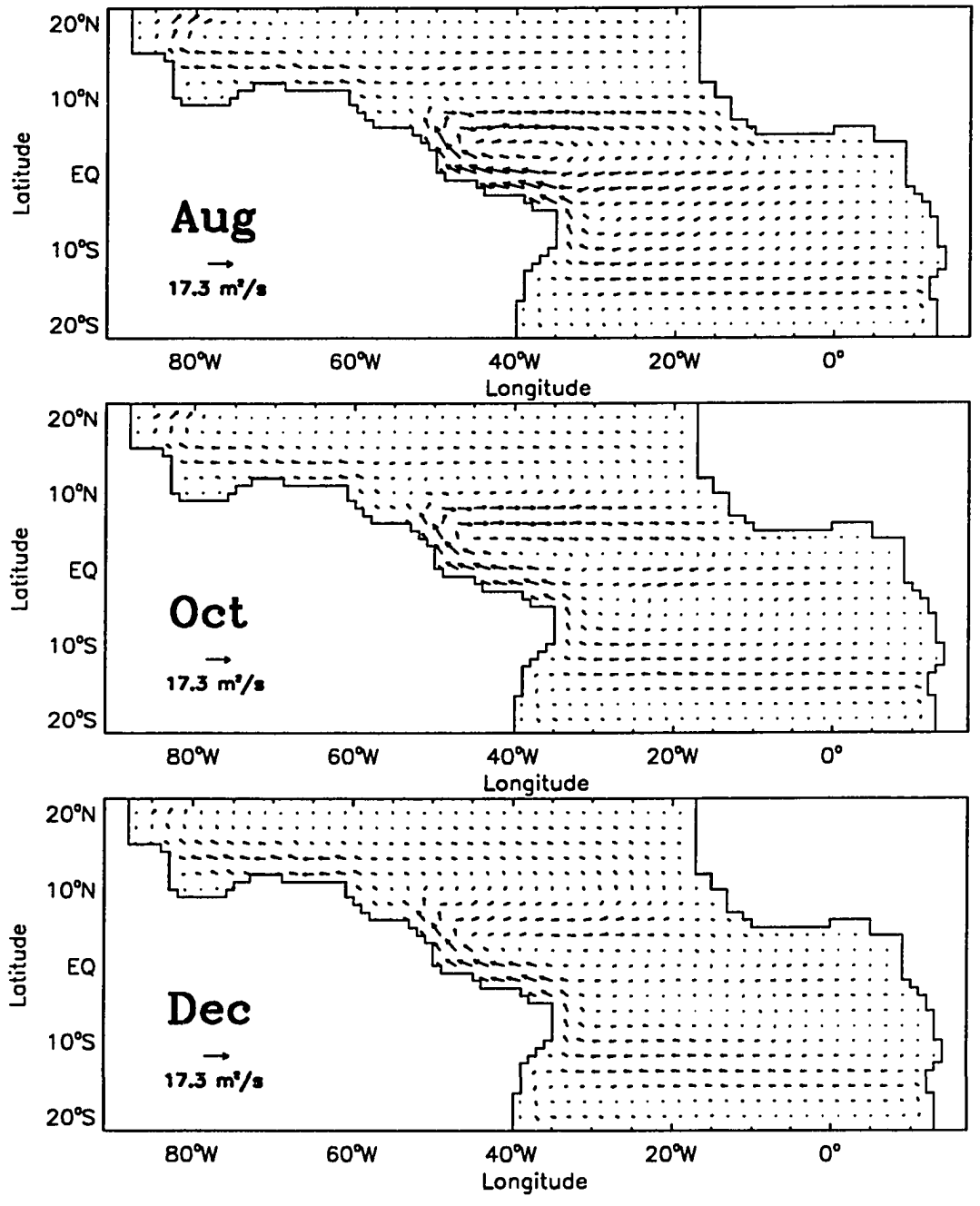

Figure 24: continues.

the SSEC collides with the coast, it bifurcates into the south-flowing Brazil Current and the NBC, which flows toward the equator. The location and strength of the SSEC exhibits very minor changes with time. Judging from Figure 16, the zero wind stress curl line in the South Atlantic is located approximately near the center of the SSEC at 10°S and hardly moves with time. Since the SSEC is in Sverdrup balance in general, it is not surprising to observe that the SSEC is nearly steady most of time.

The ESEC, on the other hand, is the west-flowing equatorial surface jet and is influenced mostly by the zonal wind stress cycle near the equator. The response of the ESEC to the seasonal cycle of the zonal wind stress can be readily observed in Figure 25, which shows the time changes of the zonal wind stress and of the ESEC transport averaged between 2°S and 2°N. There are two peaks of the ESEC, one in the western basin during June/August and the other in the central basin between May and July. The variation of the ESEC has some similarities to the variation of zonal wind stress along the equator, especially since the variation of the zonal wind stress east of 30°W is highly correlated with that of the ESEC as shown in Figure 25(c). In any case, as a consequence of the seasonal cycle of the ESEC shown in Figure 25(b), the dominant source for the NBC is shifted from the SSEC to the ESEC during June/August. In these months, since the SSEC is nearly steady, there exists an excess of the WWM available to be taken out via the NBC to the subtropics.

The seasonal cycle of the NECC can be clearly observed in Figure 23. In general, the simulated cycle is compatible to the ship drift map of Richardson and McKee (1984). However, although very weak, the east-flowing NECC still exists during February/April between 2°N and 5°N, contradicting the surface current map of Richardson and McKee (1984), which shows a reversal of the NECC in these months. Between February and April, the location of the simulated NECC core still matches with the position of the ITCZ (Figure 16; Figure 23). Therefore, the model-produced

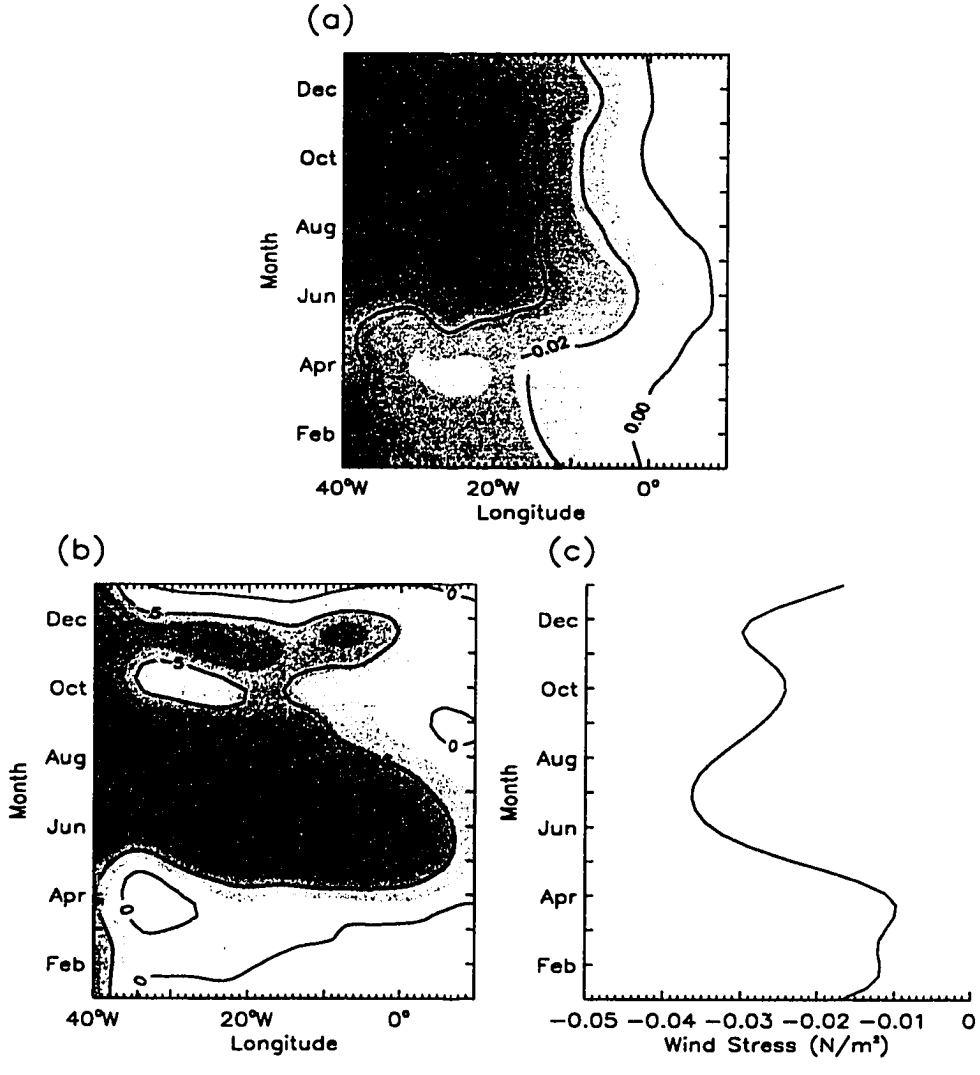

Figure 25: The time-longitude plots of (a) the zonal wind stress (from Hellerman and Rosenstein, 1983) and of (b) the ESEC transport at the equator. (c) The zonal wind stress averaged between 30°W and 10°E. The (a), (b) and (c) are all averaged between 2°S and 2°N. The units are N/m^2 for (a) and (c) and m^2/s for (b)

NECC is more or less in phase with the wind stress curl pattern. Despite the disagreement in February/April, the seasonal change of the location and strength of the simulated NECC are very close to those found by Richardson and McKee (1984). From February to April, the NECC is very weak and located south of the 5°N. It gains maximum strength in August and remains strong until October. During this period, the core of the NECC moves from 5°N to 8°N then back to 5°N again. Between November and January, the equatorward excursion of the NECC core still continues. But this time, the strength of the NECC becomes much weaker.

To better describe the dynamics of the simulated NECC, the model result is compared with the Sverdrup volume transport stream function obtained from the wind stress data of Hellerman and Rosenstein (1983). The stream function is calculated from the Sverdrup equation:

$$\psi = \int_{\phi}^{\phi_e} \frac{a}{2\Omega cos\theta \rho_o} \left(\frac{\partial \tau^{\theta}}{\partial \phi} - \frac{\partial}{\partial \theta}(\tau^{\phi} cos\theta)\right) d\phi, \tag{21}$$

where ϕ and θ are the longitude and latitude, respectively, ϕ_e is the longitude of eastern boundary and ρ_o is the reference density. Figure 26 shows the bimonthly map of the volume transport stream function calculated from Eqn. 21. The location of the ITCZ is identified by the zero stream line in the figure since the curl of wind stress vanishes along the ITCZ. The zero stream line migrates from 2°N in April to 10°N in August and roughly matches with the seasonal movement of the simulated NECC. In the mean time, the spatial gradient across the stream lines represents the strength of the transport. The stream lines across the ITCZ are highly compacted around August, consistent with the model result.

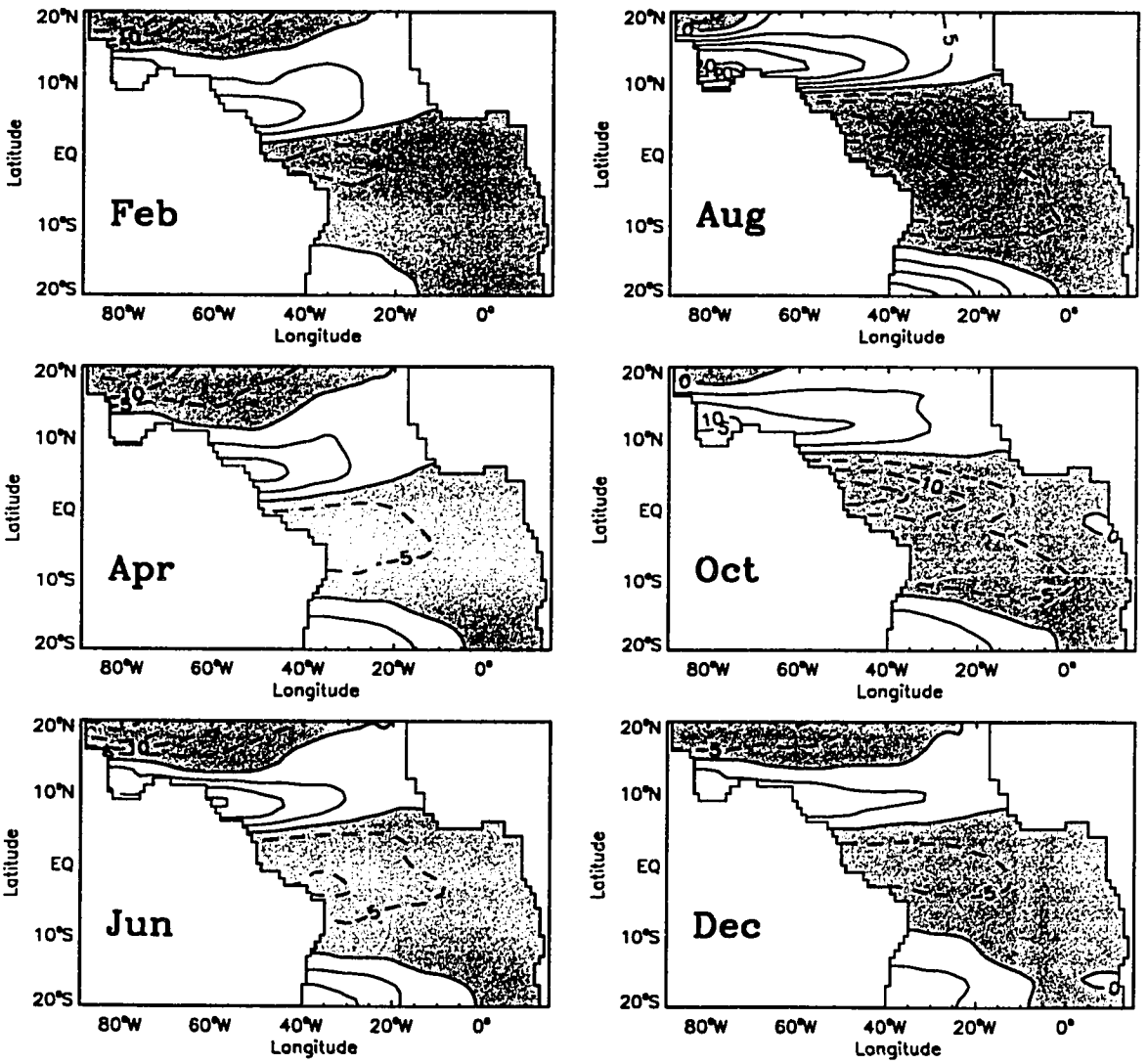

Figure 26: The Sverdrup volume transport stream function from February to December produced from the wind stress data of Hellerman and Rosenstein (1983). The unit is in Sv.

Escape of the Warm Water Mass (WWM)

To show the detailed behavior of the NBC, the mixed layer mass transport near the NBC retroflection point is plotted in Figure 27. Again, the model results are averaged monthly; therefore, eddy features are mostly filtered out. Continuation of the NBC to the Guiana Current is apparent in February. During March/April, the NEC, the southern leg of the subtropical gyre, moves down as far as 8°N and enhances the northwestward Guiana Current. In June, the NBC retroflects from the coast and feeds the eastward-flowing NECC. At the same time, the northwestward mass transport via the NBC-Guiana Current system is reduced considerably. In August, the NBC turns completely offshore into the NECC and the northward flow from the NBC to the Guiana Current is nearly vanished. After October, the NECC becomes weaker and the mass transport through the NBC-Guiana Current system is increased again. The escape of the WWM via this route becomes maximum in February when the NECC practically dies out.

It is evident from Figure 23 that there is a secondary route of the WWM escape from the NBC to the NEC, via the interior of the cyclonic gyre as pointed out by Csanady (1990). The cyclonic gyre is driven by a band of positive wind stress curl which exists between the equator and 10°N in April and between 10°N to 20°N in August (Figure 16). The meridional WWM transport across 8°N, shown in Figure 28(a), illustrates that the escape of the WWM via this route takes place during October/June and terminates in July/September when the NECC is relatively strong.

Csanady (1990) attempted to explain this using a mass conservation principle: since the NBC flows always northwestward, the NBC is incapable of supplying the water mass to the interior cyclonic gyre. Therefore, in order to close the mass deficit, the water from the NECC origin must cross the zero wind stress curl line and support

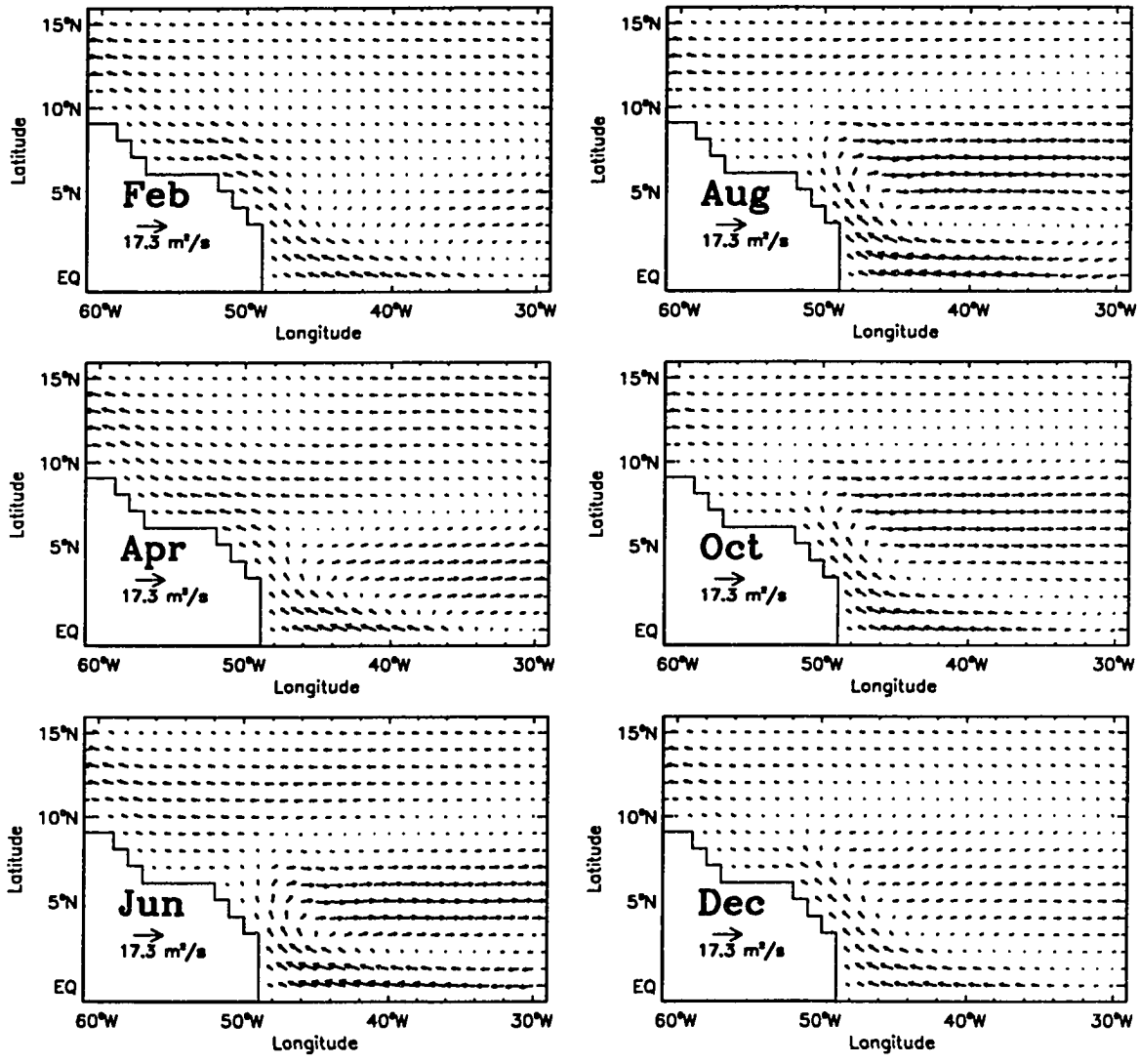

Figure 27: The mixed layer mass transport near the NBC retroflection point from February to December produced from the model result (in m^2/s).

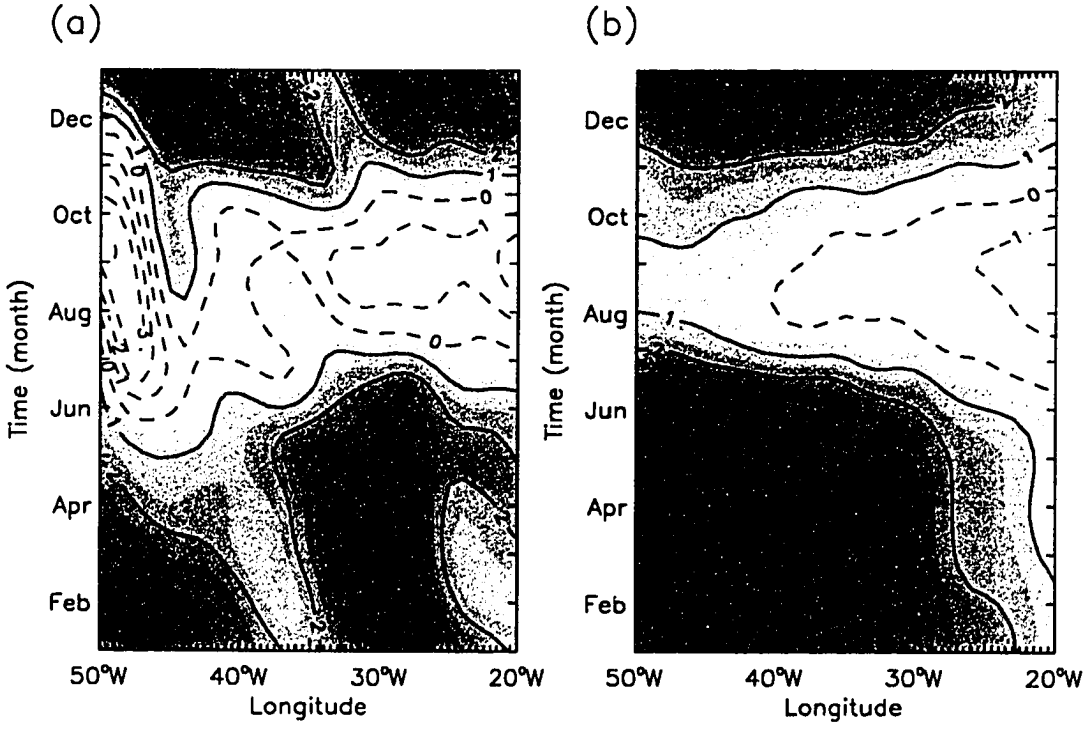

Figure 28: The time-longitude plot of (a) the total meridional transport in the mixed layer and (b) the meridional Ekman transport across 8°N. The unit is m^2/s.

the cyclonic gyre. However, this hypothesis is valid only for the annually averaged transport. It appears that this meridional transport during October/June is associated with the Ekman and Sverdrup transport cycles. The Sverdrup transport in Figure 26 shows that, across 8°N, the meridional Sverdrup transport is always northward during October/June. In addition, the Ekman transport is also in favor of the northward transport of the WWM (Figure 28(b)) during these months.

The meridional transport, in contrast to October/June, is completely blocked during July/September (Figure 28(a)). In these months, the southern end of the cyclonic gyre is located above 8°N; therefore, the Sverdrup transport is slightly southward. The contribution of Ekman transport across 8°N is also equatorward during this period (Figure 28(b)). More importantly, during July/September, a sudden increase in the wind stress curl north and south of 8°N causes a seasonal deepening (shallowing) of the mixed layer depth south (north) of 8°N, forming a strong potential vorticity (PV) front (Figure 29). Since the geostrophic flow tends to follow along the PV contours, the meridional motion is limited in these months.

Transport in the Thermocline Layer

The mass transport in the thermocline layer from February to December is shown in Figure 30. In order to show the seasonal cycle of the EUC, the zonal mass transport is contoured across 30°W, 20°W and 10°W, as shown in Figure 31. The zonal transport across 30°W shows that the EUC transport is relatively small during February/May. After May, it starts to increase until it reaches its maximum in July/August and decreases thereafter. At 20°W, the EUC transport pattern is very similar to that across 30°W, but the maximum transport occurs in September and the core of the EUC is shifted slightly southward. The EUC transport is reduced significantly at 10°W and its core shifted further south.

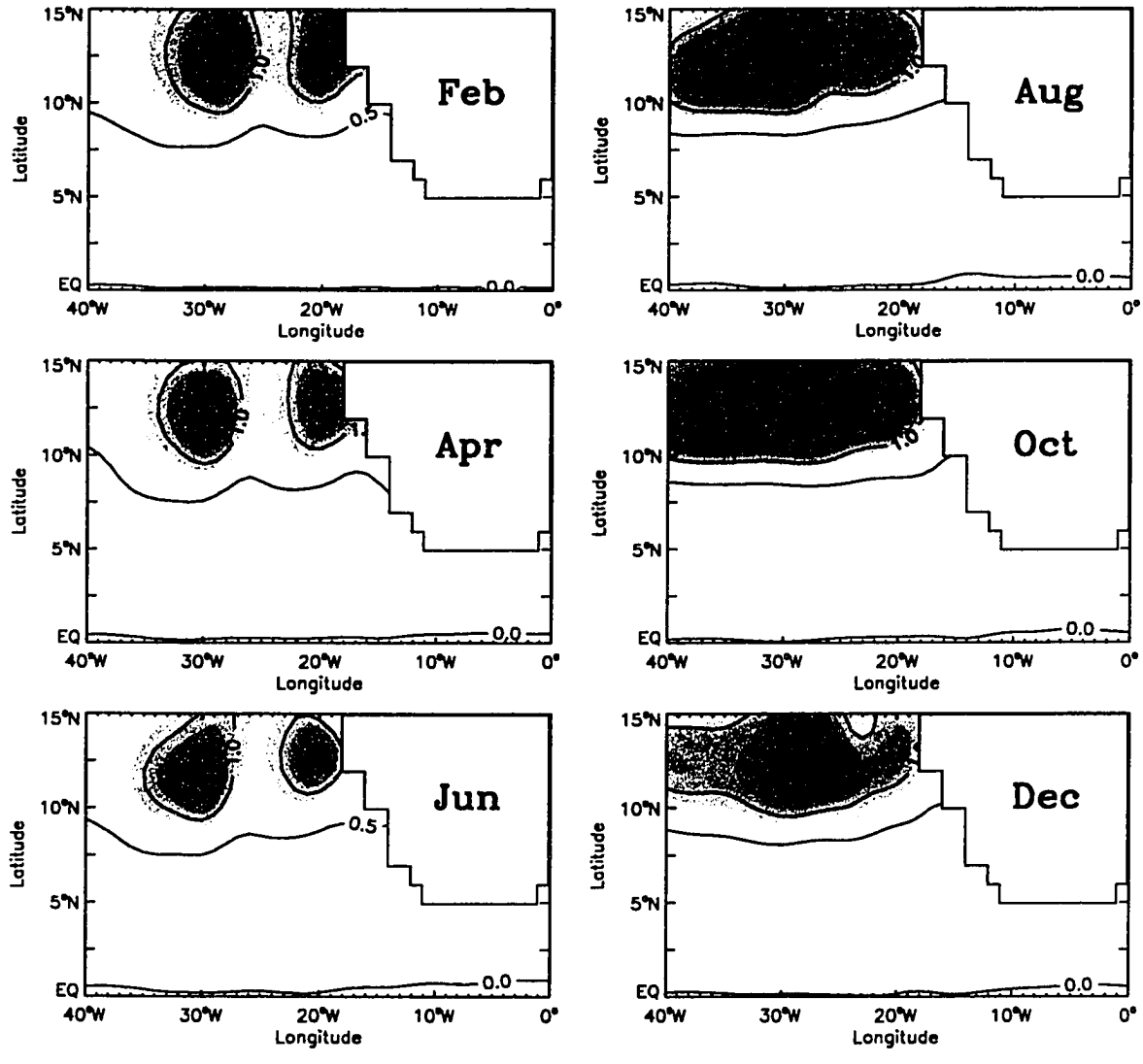

Figure 29: The potential vorticity of the mixed layer from February to December taken from the model result (in $10^{-6}\mathrm{m}^{-1}\mathrm{s}^{-1}$).

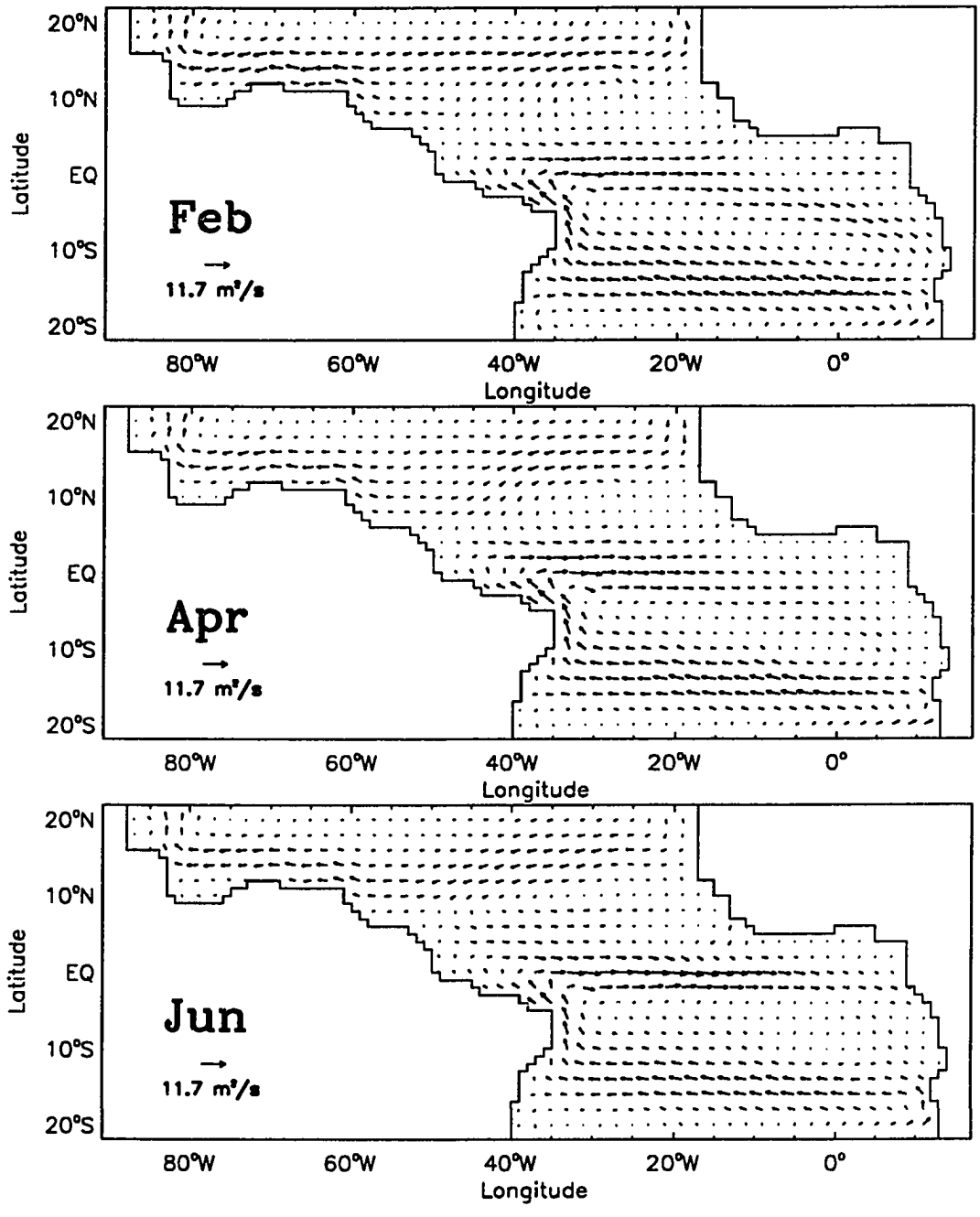

Figure 30: The mass transport in the thermocline layer from February to December taken from the model result (in m^2/s).

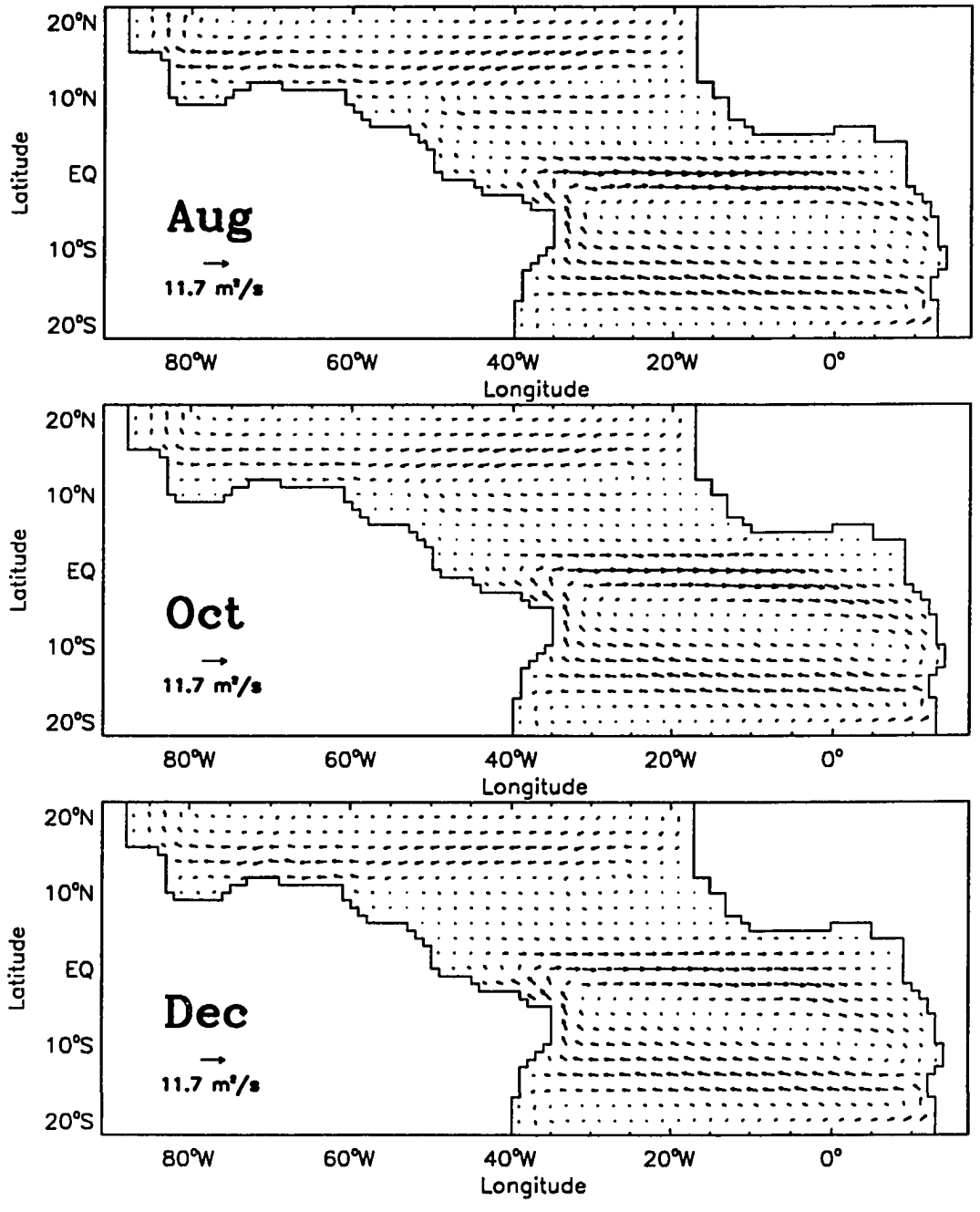

Figure 30: continues.

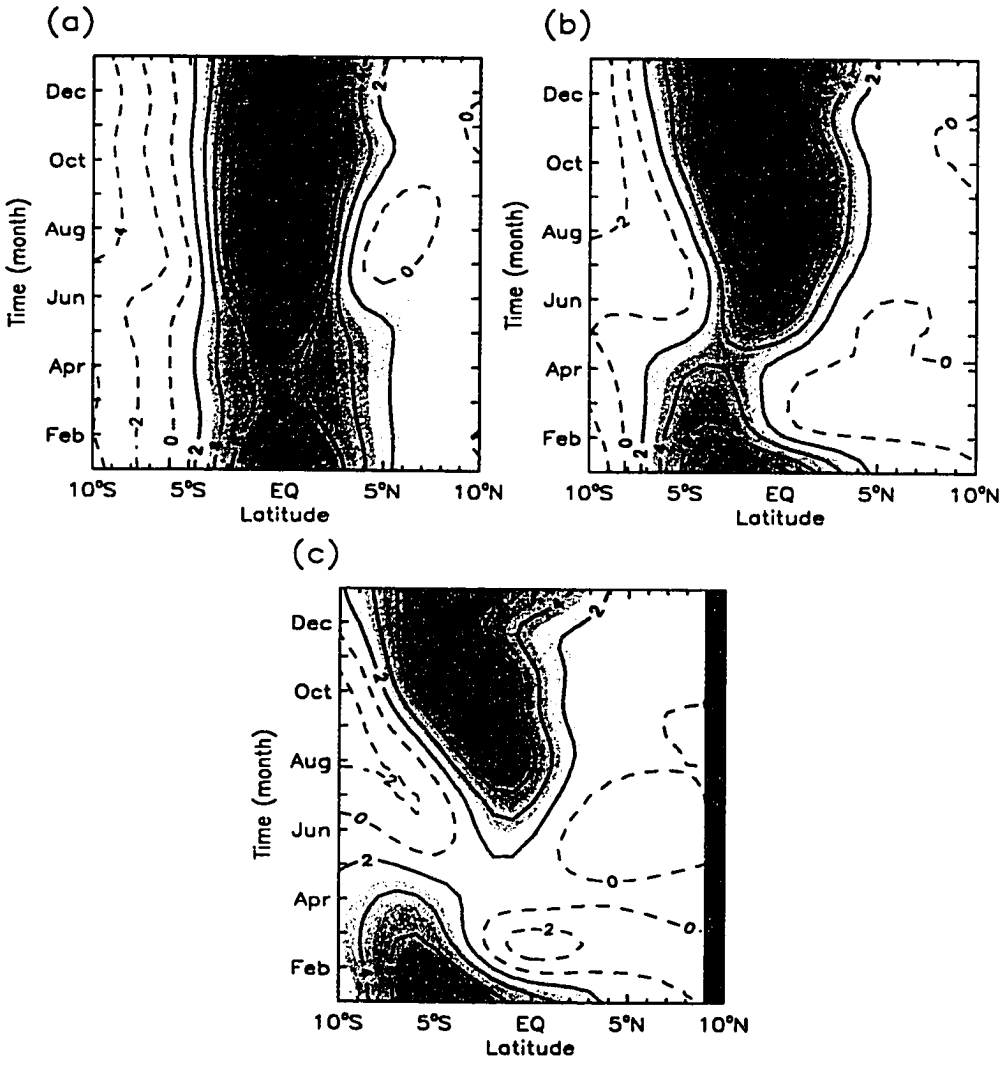

Figure 31: The time-latitude plot of the EUC across (a) 30°W, (b) 20°W and (c) 10°W from the model result. The unit is m^2/s.

Figure 32 shows the meridional mass transport in the thermocline layer across 8°S as a function of time and longitude. The subsurface NBC experiences no significant seasonal changes. Meanwhile, the transport in the eastern basin is dominated by its seasonal cycle. It appears that the variability in the east is created by the surplus of the EUC transport during September/May, when the equatorial entrainment is not significant.

Seasonal Storage Rate of Mass and Heat

The storage rate of the WWM inside the tropical belt is the sum of entrainment and horizontal flux rate across the two zonal boundaries at 8°S and 8°N. Therefore, in order to quantify the seasonal cycle of the WWM storage rate, the entrainment rate is integrated between 8°N and 8°S and the meridional transports of the WWM are integrated along 8°S and 8°N. The WWM storage rate is obtained by summing these three components as shown in Figure 33. The entrainment rate reaches 25 Sv in June and decreases rapidly afterward until October. A minor peak of 8 Sv is observed in November. The horizontal mass flux across 8°S is insignificant. The storage rate of the WWM is, therefore, largely characterized by the interplay between the entrainment rate and the northward escape across 8°N. Between January and April, the entrainment nearly ceases, while the northward escape reaches its maximum. During April/December, on the contrary, the entrainment becomes significant, but the northward escape is reduced considerably. Consequently, the WWM inside the equatorial belt undergoes divergence during November/April and accumulation between May and October as depicted in Figure 33(c). The maximum accumulation occurs during June/August as the entrainment rate has its maximum at June and the northward escape rate has its minimum in August. The storage rate in the thermocline layer is, on the other hand, determined solely by the entrainment rate, since the fluxes across

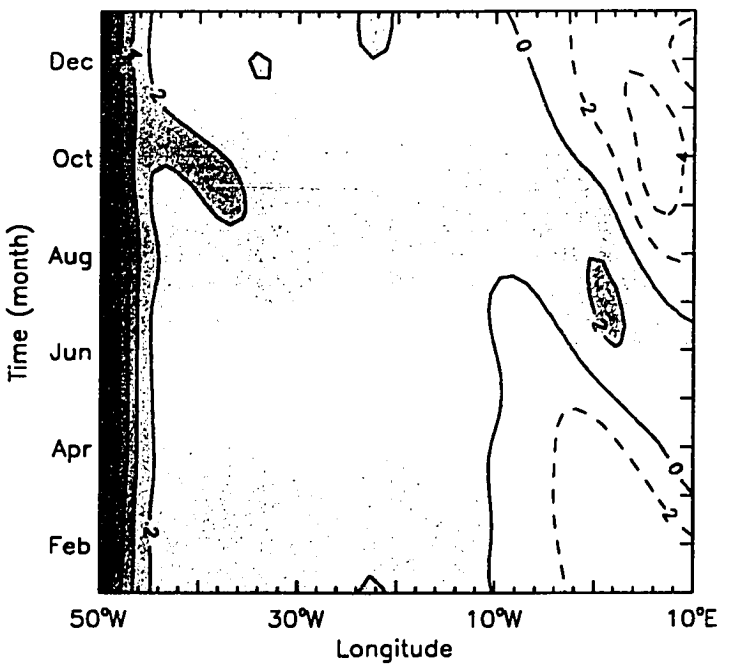

Figure 32: The time-longitude plot of the meridional mass transport in the thermocline layer across 8°S taken from the model result. The unit is m^2/s.

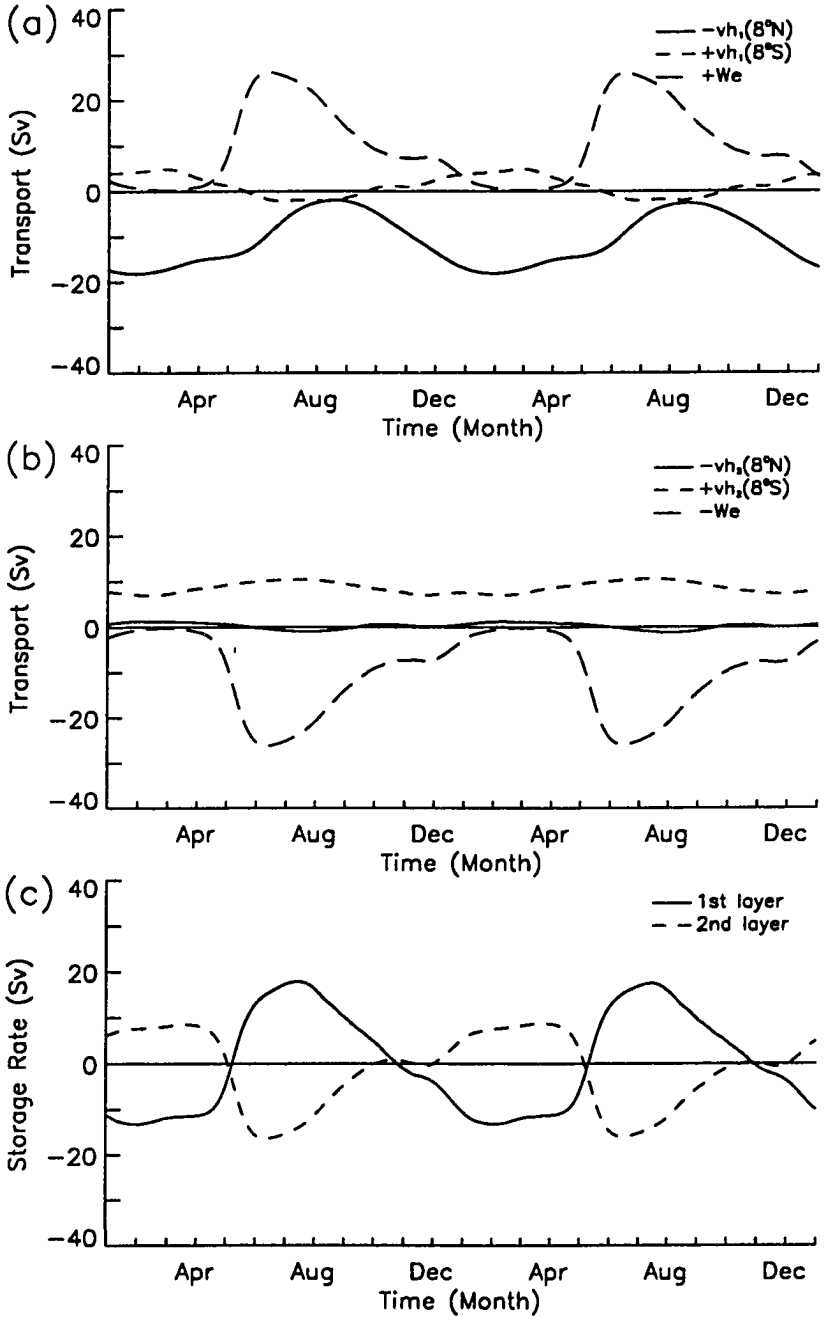

Figure 33: The time changes of the meridional transports of the WWM integrated along 8°S and 8°N, the entrainment rate and storage rate of the WWM both integrated between 8°N and 8°S. The unit is in Sv.

the 8°N or 8°S show no significant seasonal changes (Figure 33(b)).

The two-dimensional pattern of the warm water mass storage rate is also shown in Figure 34, which provides a more detailed spatial structure. The unit is meter per month. The seasonal variability of storage rate is mostly concentrated in the western and central tropical Atlantic, bounded zonally by the equator and 15°N. The storage rate of two latitude bands of 0-8°N and 8°N-15°N oscillate 180° out of phase to each other, annually. As discussed earlier, the Ekman pumping cycle in this region is appears to be responsible for this (Garzoli and Katz, 1983). Between 8°N and 15°N, Ekman divergence occurs during December/April and Ekman convergence in August/October, as shown in Figure 35. The Ekman divergence south of 8°N is out of phase to the north of 8°N. This signal matches with the warm water mass storage rate in this region. Another seesaw pattern of the storage rate is observed between the western and eastern basins of the equator. Between May and July, accumulation occurs in the western tropics while divergence prevails in the eastern tropics and vice versa during November/March.

6.3 Mixed Layer Heat Budget (WWM Formation)

In the previous sections, it was found that the entrainment is a heat gain term for the mixed layer (*e.g.*, Figure 17) rather than a cooling term. This is because we calculated the divergence of heat content with respect to zero degree water, not to the mixed layer temperature. Therefore, as long as the temperature of the entrained water is warmer than zero degree, the heat divergence contribution of the entrainment is always a heat gain.

Furthermore, it was also noticed that the seasonal cycle of the heat transport via the entrainment closely followed that of the volume transport. The reason is that

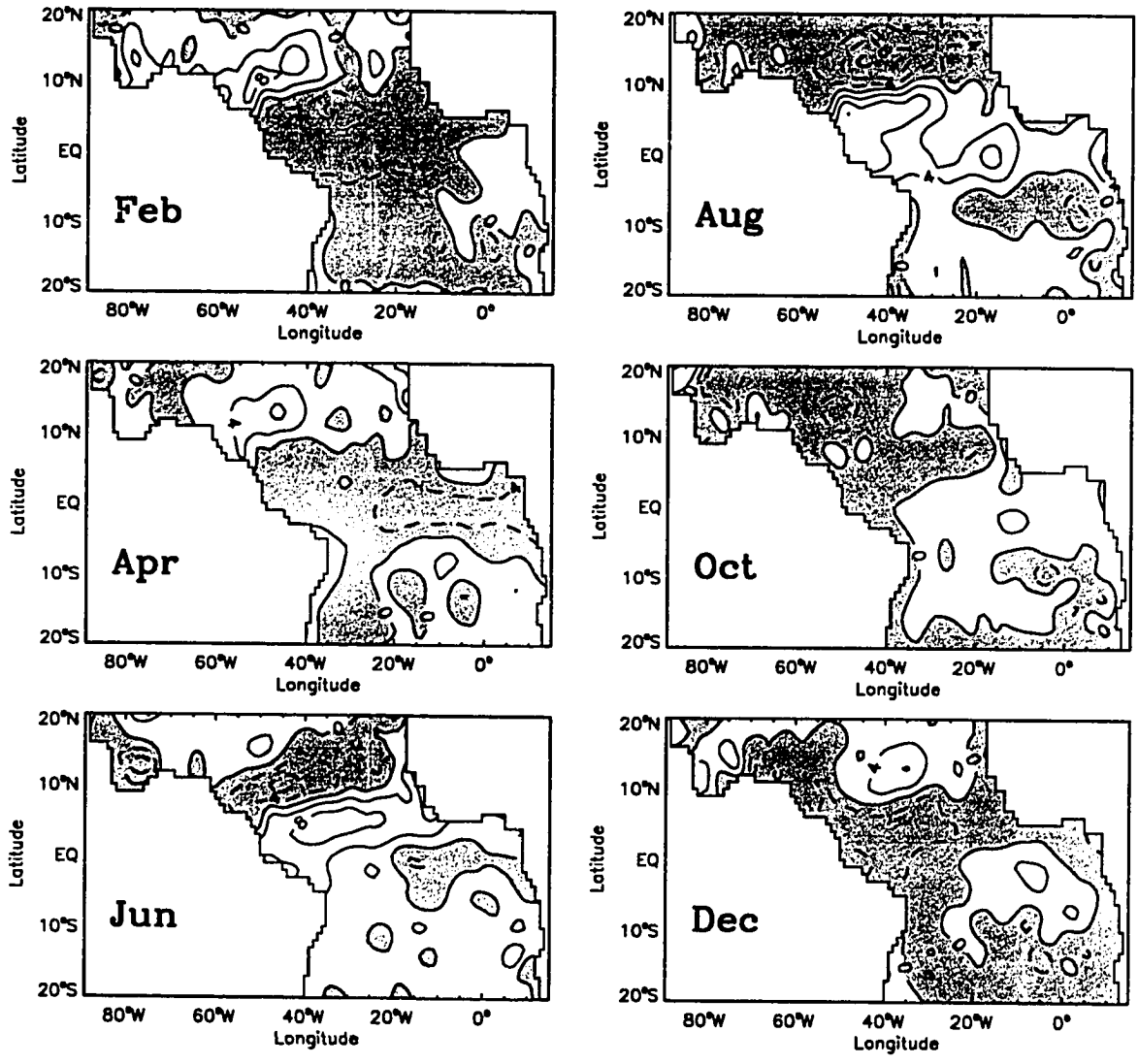

Figure 34: The 2-D structure of the WWM mass storage rate from February to December based on the model result. The unit is meter per month.

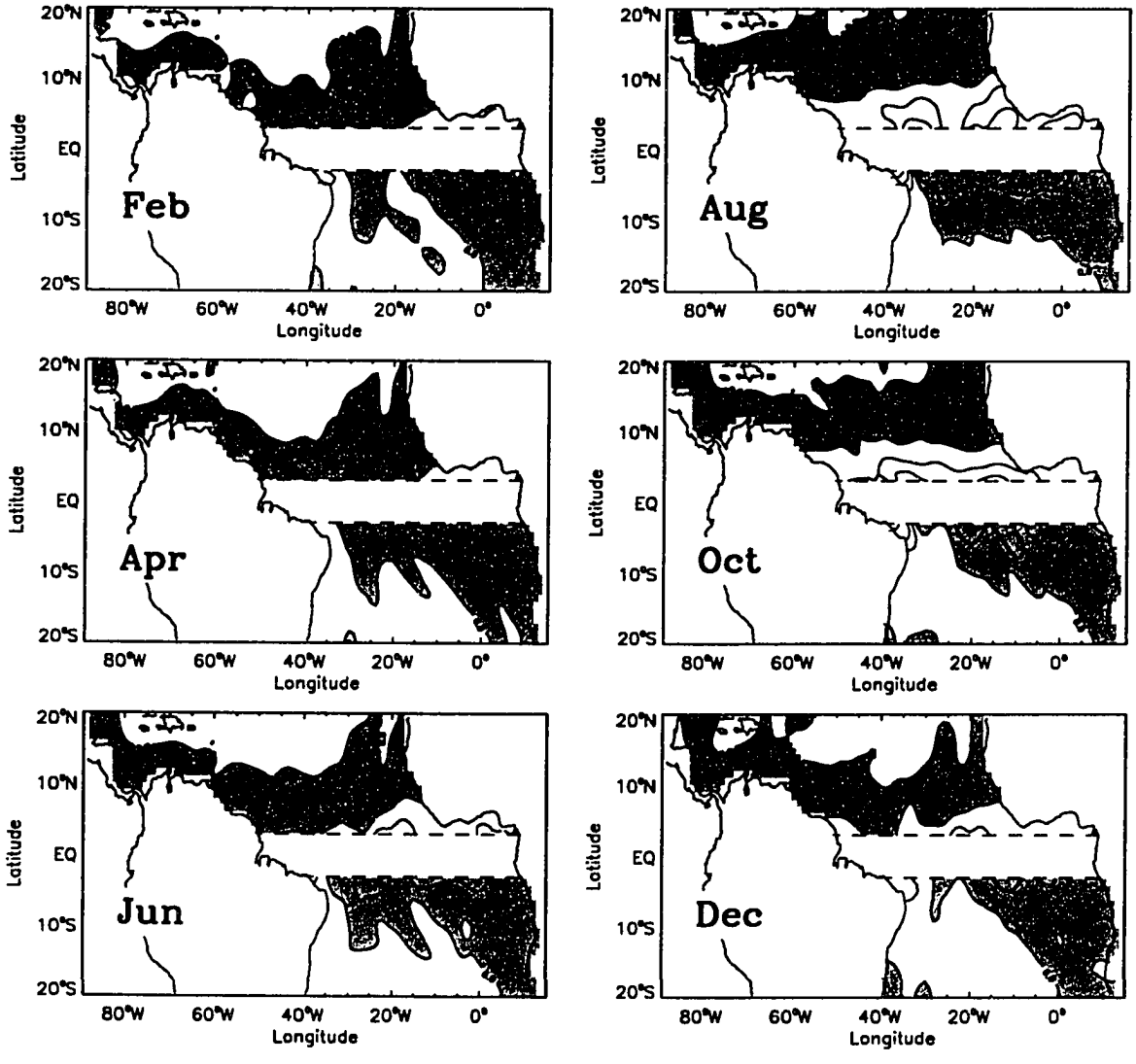

Figure 35: Monthly mean Ekman divergence (shaded) from February to December (in unit of 10^{-5}m/s). Reproduced from Hellerman and Rosenstein (1983).

the volume gain by the entrainment is far greater than the actual decrease of the temperature due to the cooling effect of the entrainment (Philander and Pacanowski, 1986).

Considering these, it would be misleading to use the conventional heat content equation to describe or quantify the warm water formation process. Therefore, we now derive a set of new equations appropriate for studying thermodynamics in the tropical warm water. With the help of these equations, the seasonal heat balance of the mixed layer is examined.

The total heat content equation for the mixed layer is written as:

$$\frac{\partial(T_1 h_1)}{\partial t} + \frac{\partial}{a\cos\theta\partial\phi}(u_1 T_1 h_1) + \frac{\partial}{a\partial\theta}(v_1 T_1 h_1) = \frac{Q}{\rho C_{pw}} + w_e T_2. \tag{22}$$

Multiplying the continuity equation (Eqn. 6) by a constant temperature T_o then subtracting it from the Eqn. 22, we get

$$\frac{\partial[(T_1 - T_o)h_1]}{\partial t} + \frac{\partial}{a\cos\theta\partial\phi}[u_1(T_1 - T_o)h_1] + \frac{\partial}{\partial\theta}[v_1(T_1 - T_o)h_1] = \frac{Q}{\rho C_{pw}} - w_e(T_o - T_2). \tag{23}$$

The heat storage rate of the mixed layer can be divided into two terms:

$$\frac{\partial(T_1 h_1)}{\partial t} = \frac{\partial(T_o h_1)}{\partial t} + \frac{\partial[(T_1 - T_o)h_1]}{\partial t}. \tag{24}$$

The first term on the right side describes the change of the heat content not affected by the temperature change in the layer (adiabatic heat change), while the second term represents the net change of the heat content with respect to the T_o (diabatic heat change). If the T_o indicates the annually and spatially averaged temperature of the mixed layer inside the equatorial cell bounded by the continental lands and the two zonal boundaries, the Eqn. 23 becomes the heat content anomaly equation for the mixed layer. Niller and Stevenson (1982) chose T_o to be 25°C and integrated Eqn. 23 along that isotherm to remove the divergence terms. But in this study, such

a procedure is not required since the advective velocity at a given time and location is predetermined from the model result.

When the Eqn. 23 is integrated over the whole equatorial cell, we get:

$$\int_A \frac{\partial[(T_1 - T_o)h_1]}{\partial t} dA - \int_{8^oS} \vec{v_1} \cdot \vec{n} h_1 (T_1 - T_o) dl + \int_{8^oN} \vec{v_1} \cdot \vec{n} h_1 (T_1 - T_o) dl = \int_A \frac{Q}{\rho C_{pw}} dA - \int_A w_e (T_o - T_2) dA, \quad (25)$$

where the unit vector $\vec{n}$ represents the vector normal to the southern or northern boundaries. Since these boundaries are both zonal, the normal velocity is meridional velocity. A is the total space of the equatorial cell and l is the integration paths along the zonal boundaries. Figure 36 shows the seasonal variation of each term in the Eqn. 25 inferred from the model result. In general, the contribution of the diabatic heat anomaly fluxes at the zonal boundaries are negligibly small (not shown here). Therefore, the cycle of the diabatic heat storage rate is determined by the local heat balance between the air-sea heat flux and the entrainment cooling. The air-sea heat flux has two maximums in March and October and a minimum in May/June. The entrainment cooling prevails only between May and December, with its maximum in June/July. Accordingly, diabatic heat storage occurs between September and March and escape during April/August. The SST change is out of phase with the diabatic heat storage rate; the maximum (minimum) SST occurs when the storage rate changes sign from positive (negative) to negative (positive). It must be pointed that the total heat storage rate is largely determined by the mass storage rate (or adiabatic heat storage rate), and the diabatic heat storage rate accounts for only a small portion.

There is a general belief that the strength of the cold water tongue represents the entrainment rate. However, the result presented here suggests that the SST change at the equator is a rather complicated result of the mixed layer heat balance marked by the local heat balance between the air-sea heat flux and the entrainment cooling. Furthermore, the SST change is roughly out of phase with the entrainment cooling

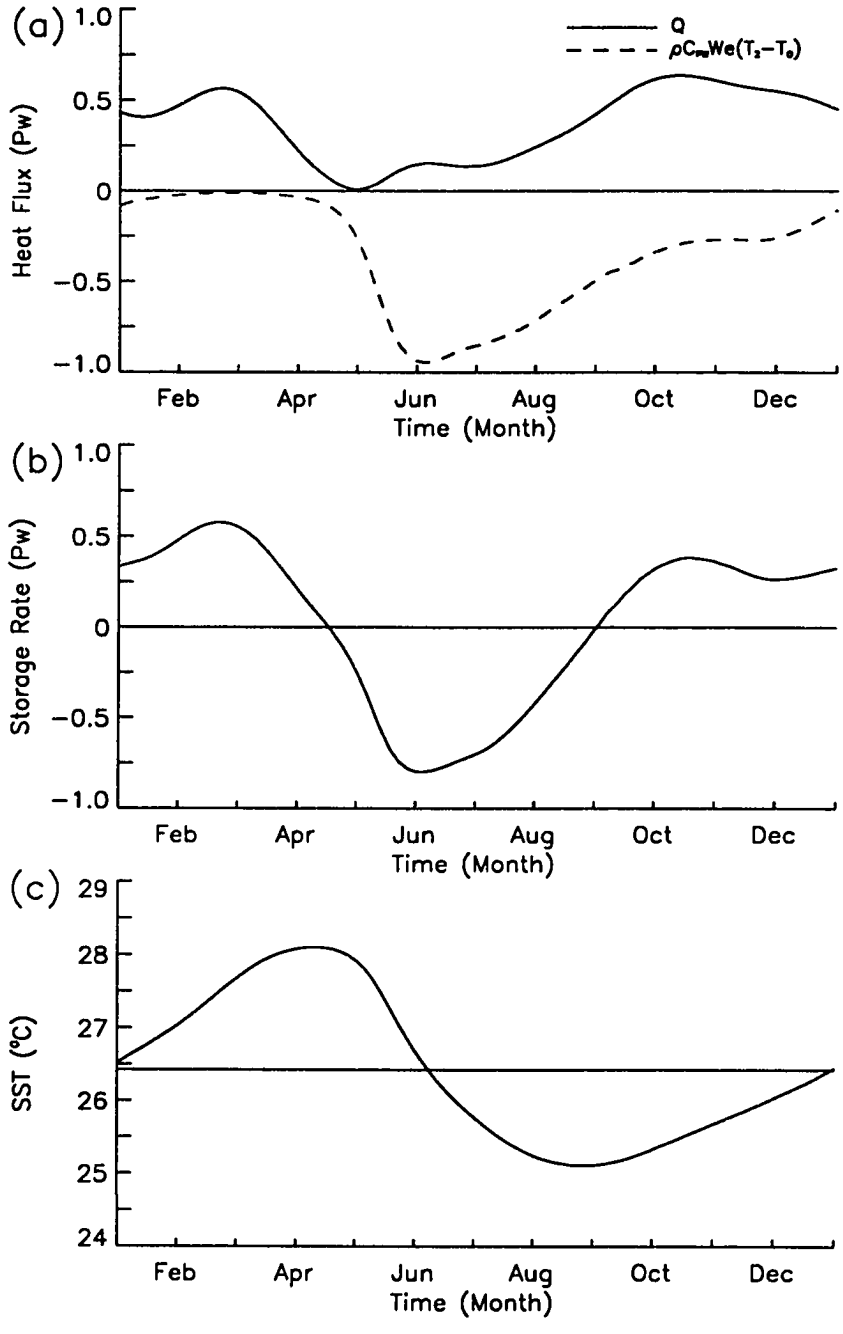

Figure 36: Model-produced (a) net surface heat gain and entrainment cooling, (b) the diabatic heat storage rate all integrated between 8°S and 8°N and (c) the SST (°C) averaged between 8°S and 8°N.

cycle, since the entrainment has an accumulative effect on the SST change. Therefore, the minimum SST occurs in August/September and the entrainment rate becomes maximum in June/July.

The entrainment cooling is responsible for the diabatic cooling during May/August, and the air-sea heat flux is mainly used to warm up this water mass. Therefore, the warm water formation is a direct result of the entrainment of cold water and the atmospheric heating at the air-sea interface. The contribution of the horizontal heat anomaly flux is very small. Figure 36(a) shows that, on an annual average, roughly 0.35 PW is required for the warm water formation.

7 Comparison with Observations

The results from the simple two layer model presented in the previous chapters showed that the heat and mass storage (escape) occur in the equatorial cell during May/October (November/April), which agrees well with the observational evidence provided by Hastenrath and Merle (1986). The model results also revealed that the seasonal cycle of the heat and mass storage rate is determined entirely by the relative strength of the equatorial entrainment and the escape across the northern edge of the equatorial cell; however, the observational evidences are not extensive enough to validate this.

It is, therefore, necessary to compare our model results with the available observational data to test how well the model results represent reality. If the comparison is poor or no agreement is reached between the model results and the observations, the underlying physics of the model must be reconsidered, and furthermore this comparison can be used to identify inadequate aspects of the model physics. On the other hand, if agreement is found between the two, it is reasonable to assume that the model has at least minimal physics required, and we can further assume that the model is reproducing the realistic physics in other aspects where there is no data for verification. In this chapter, the mixed layer depth from Levitus (1982), the SST and the air-sea heat flux both from Hastenrath and Lamb (1977) are used to verify the model results.

Figure 37 is the bimonthly map of the mixed layer depth obtained from Levitus (1982). There is no universal definition of the mixed layer depth. The mixed

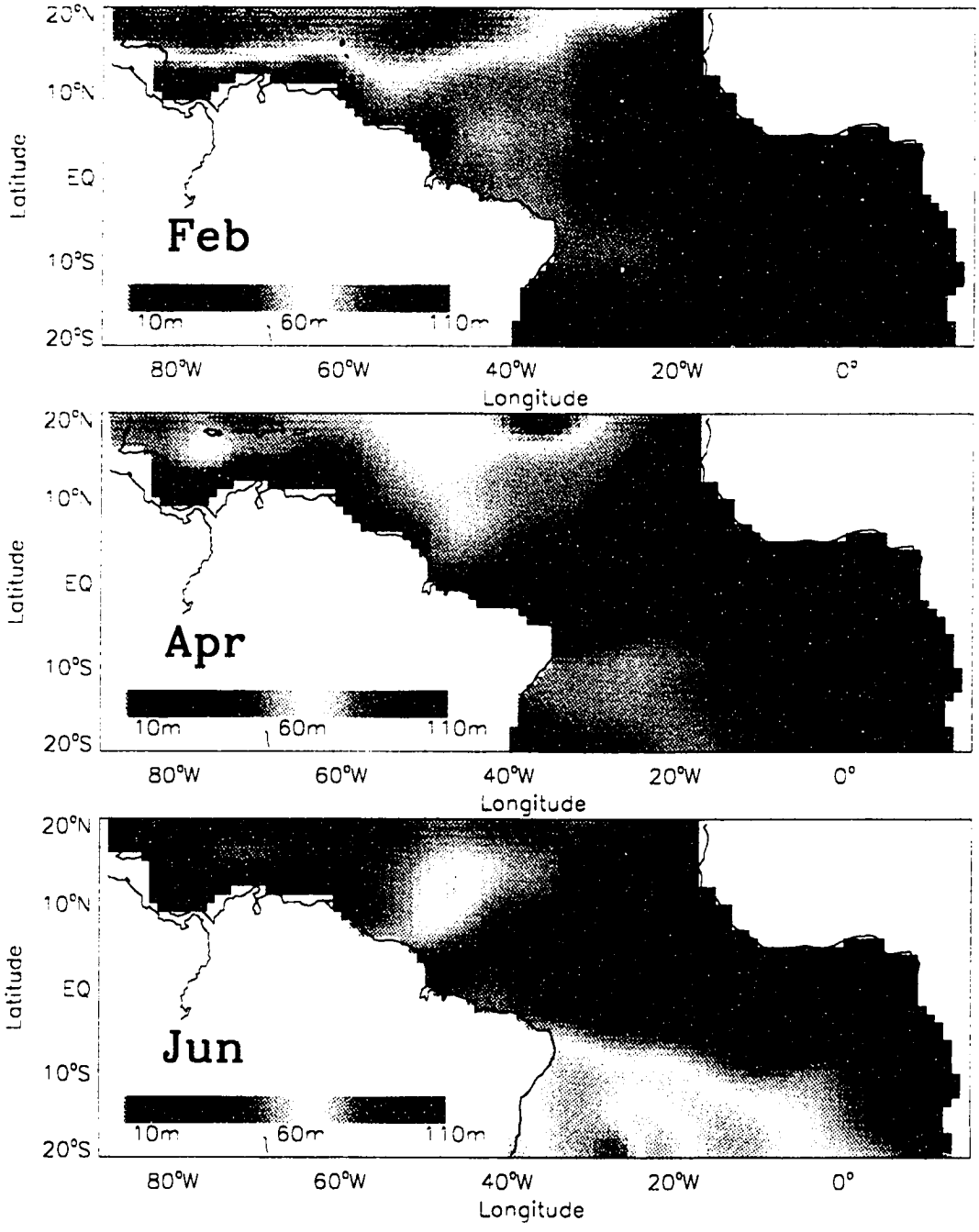

Figure 37: Monthly averaged mixed layer depths from February to December obtained from Levitus (1982). The unit is meter

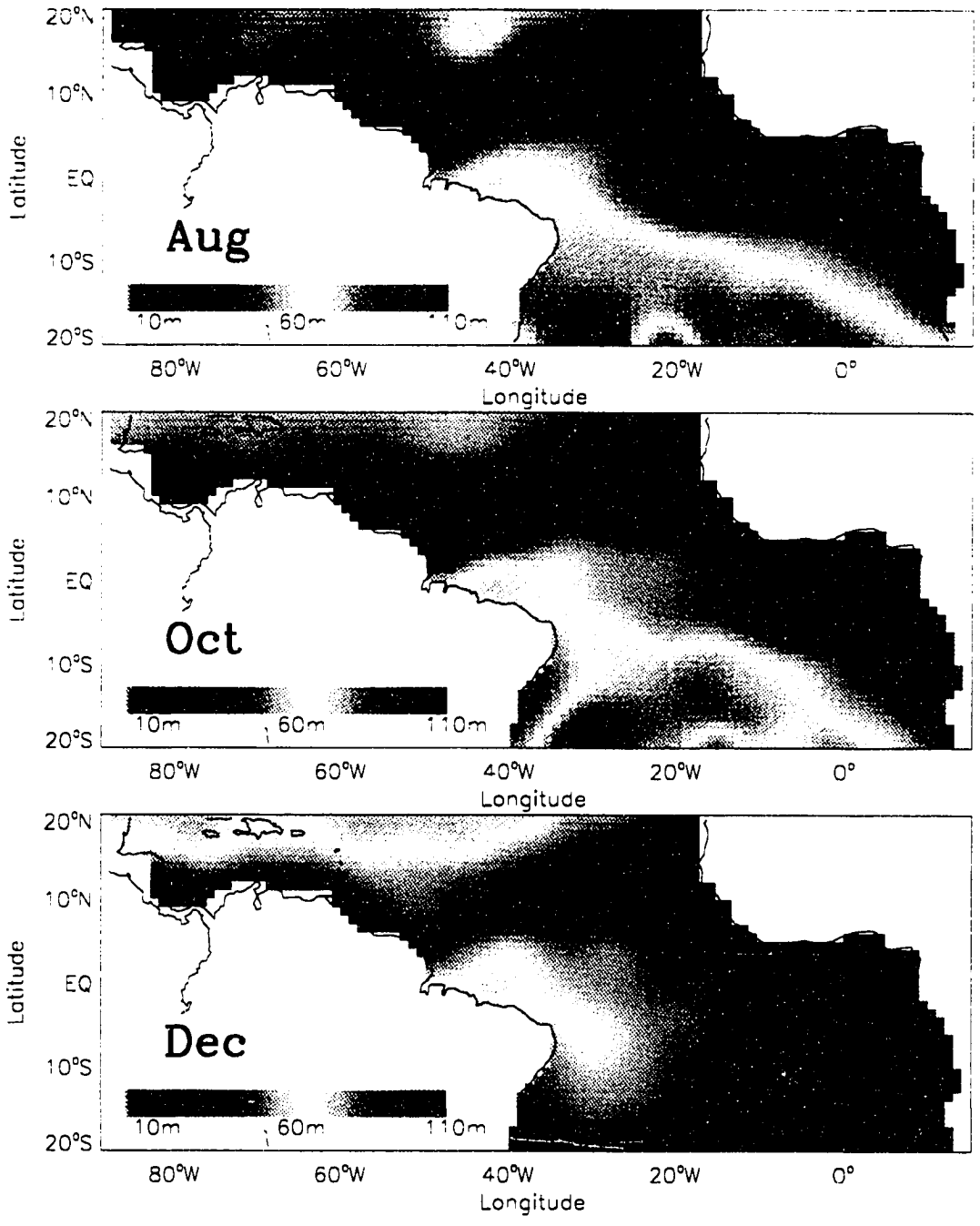

Figure 37: continues.

layer base is often taken to be the level at which the temperature is $0.5 \sim 1°C$ less than the SST (*e.g.*, Lamb, 1984). However, since the present model does not offer accurate mixed layer physics off the equator, the model-produced mixed layer depth is an isotherm rather than the actual mixed layer depth except near the equator. Therefore, we take the 25°C isotherm from Levitus (1982) and assume it as the mixed layer base (Figure 37). The salinity effect is not accounted here since it is assumed constant in the model. The model-produced mixed layer depth is shown in Figure 38.

From August to December, the Levitus data show a building-up of a warm water pool in the western part of the equator. The model mixed layer depth shows a similar pattern during that period. Away from the equator, the model results show that the 40 m contour line in the North Atlantic is extended further offshore from the African continent during August/December. A similar trend can be found from the Levitus data but is not as sharp as the model results. In general, the correlation between these two mixed layer depth patterns was poor.

The monthly averaged SST from the model results is shown in Figure 39. The corresponding map of the observed SST is taken from Hastenrath and Lamb (1977) as shown in Figure 40. In comparison to the mixed layer depth discussed above, there is an excellent agreement between the model results and the observation. The warm water pool (high SST) in the eastern equatorial cell is observed from December to April in both SST maps. As discussed earlier, this warm water pool is maintained by the net surface heat gain and very weak entrainment during these months. Both SST maps shows a sudden development of the cold water tongue in June and its intensification in August. It is widely known that isopycnal models are superior to level models, such as the GCM, in reproducing realistic SST in the tropics. This is because, in the level models, the entrainment rate is determined by the momentum divergence

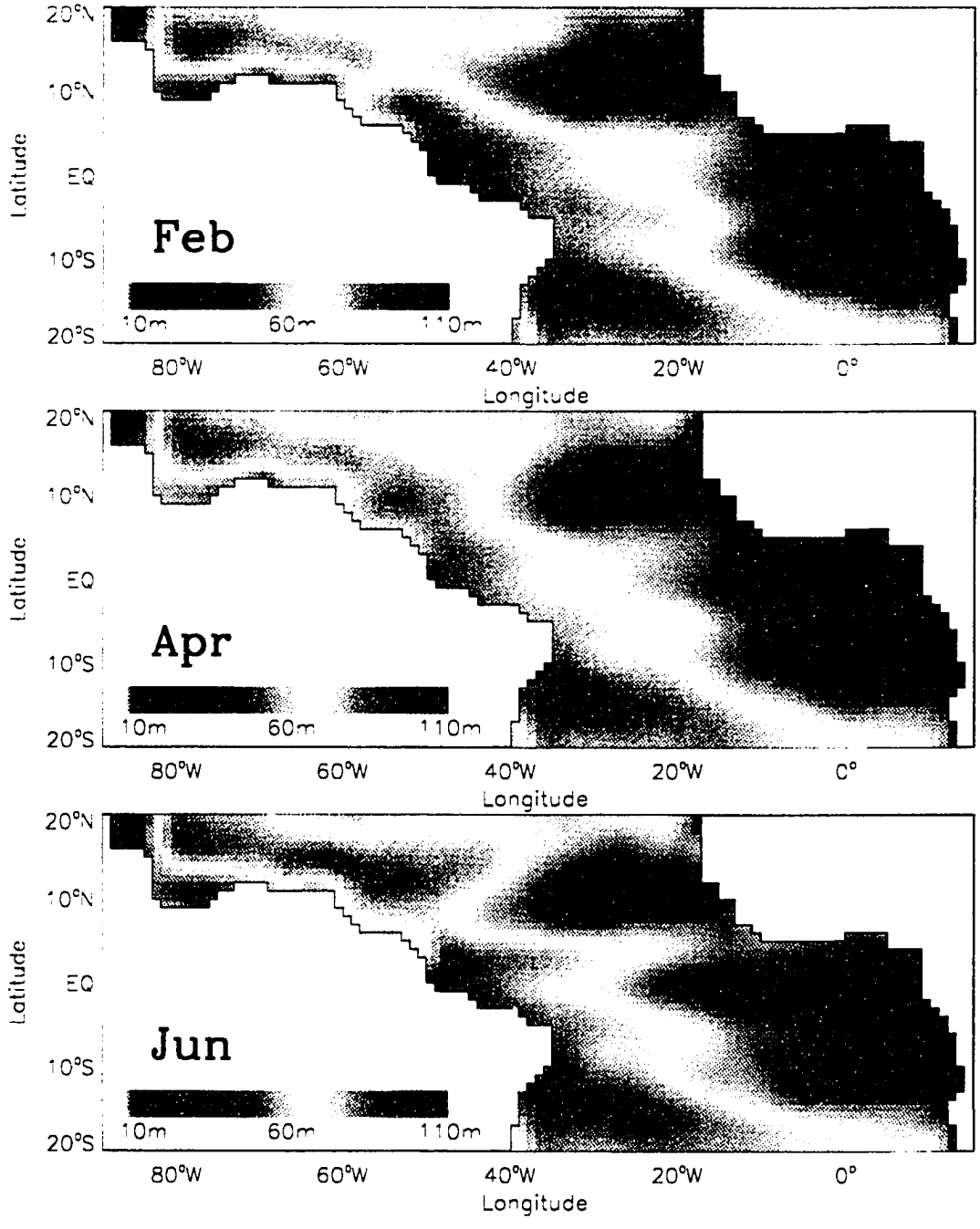

Figure 38: Monthly averaged mixed layer depths from February to December inferred from model results. The unit is meter

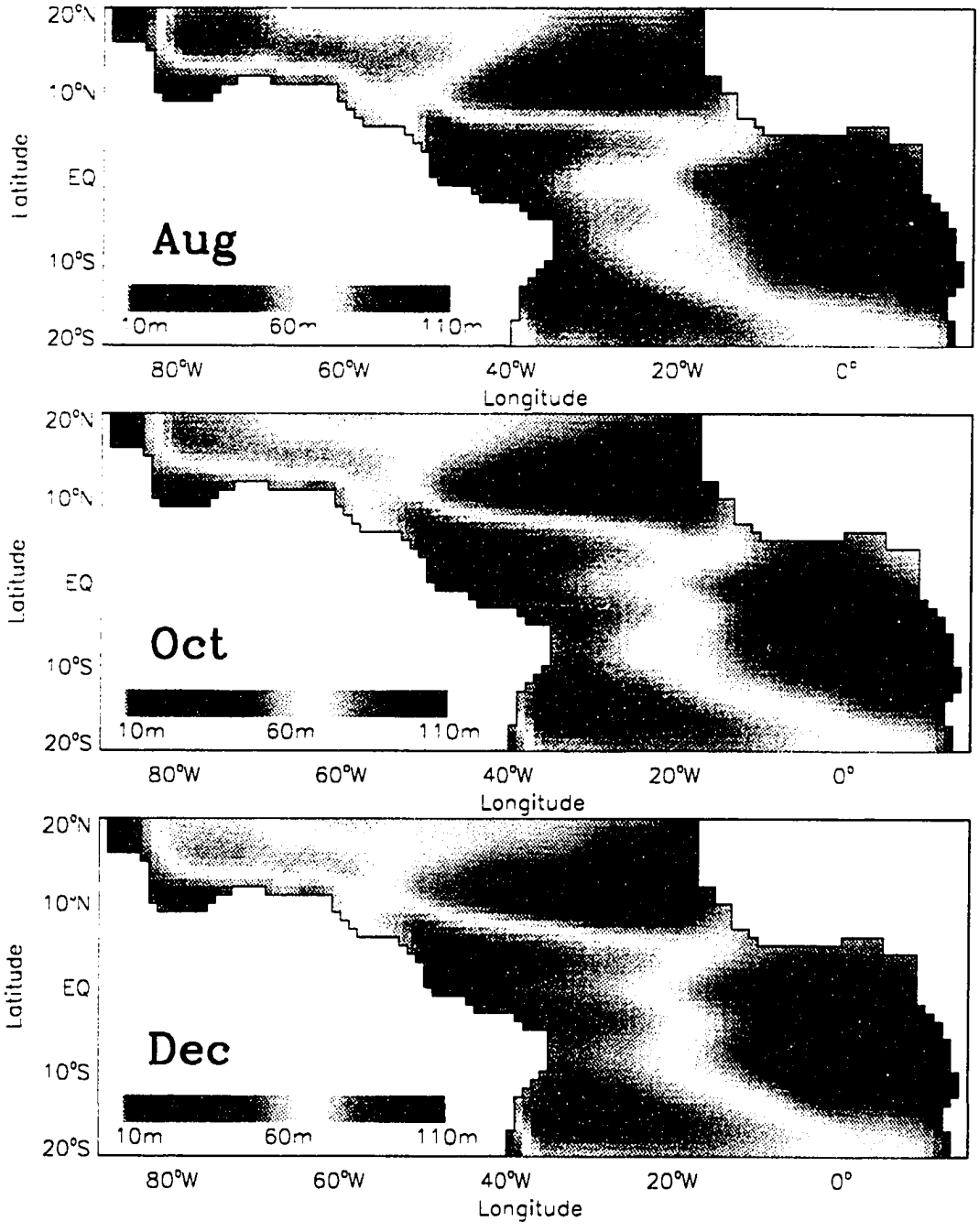

Figure 38: continues.

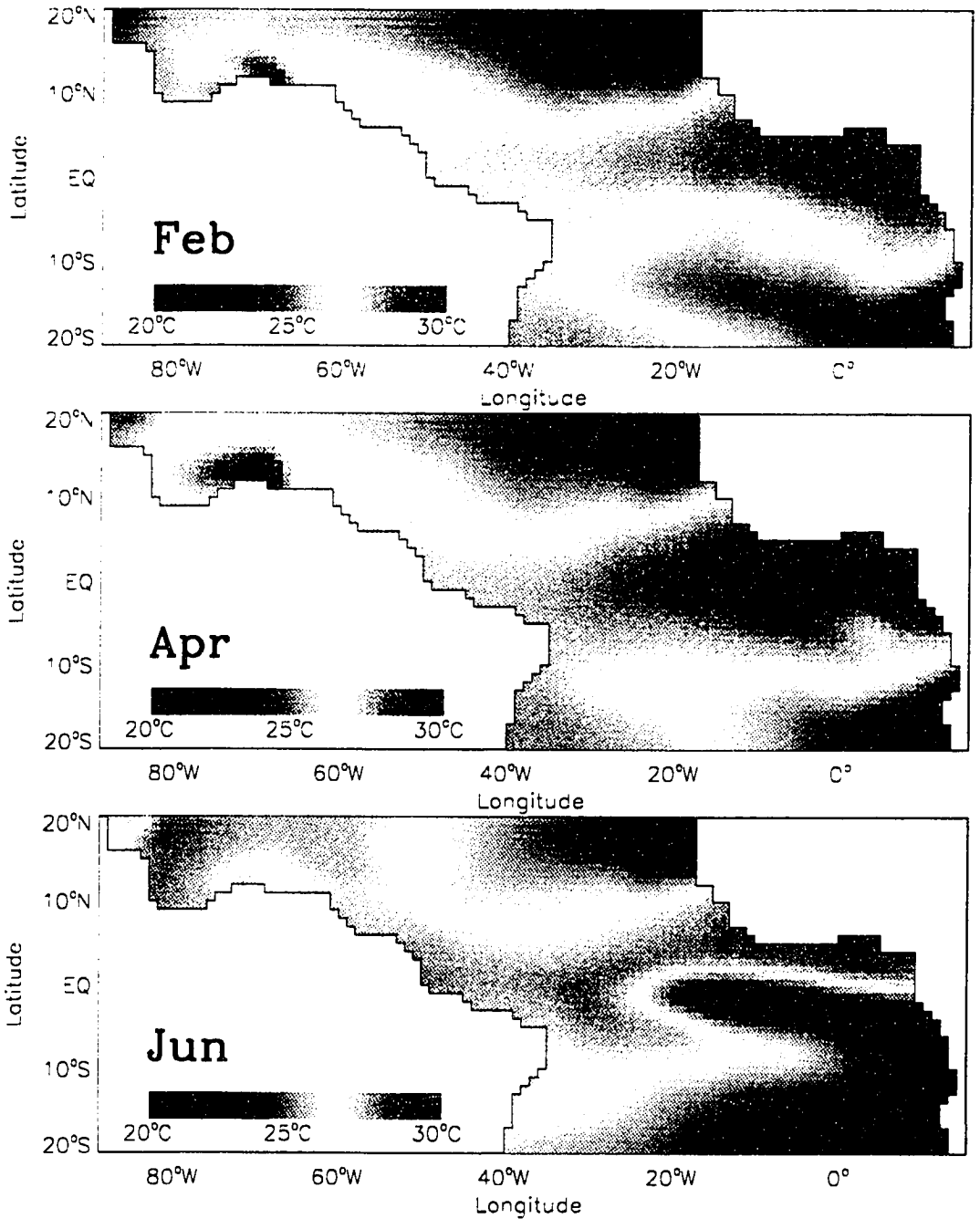

Figure 39: Monthly averaged SST from February to December inferred from model results. The unit is °C

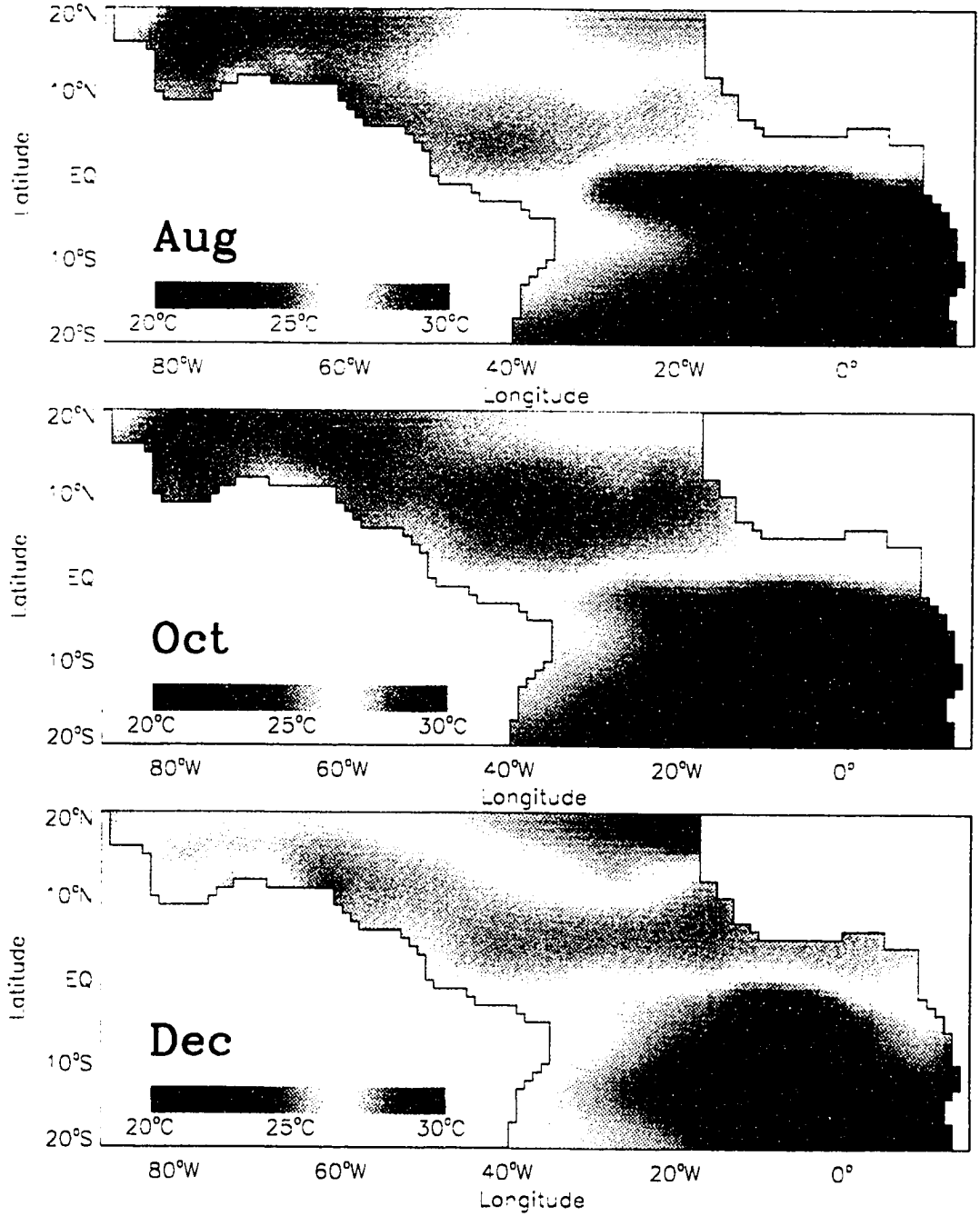

Figure 39: continues.

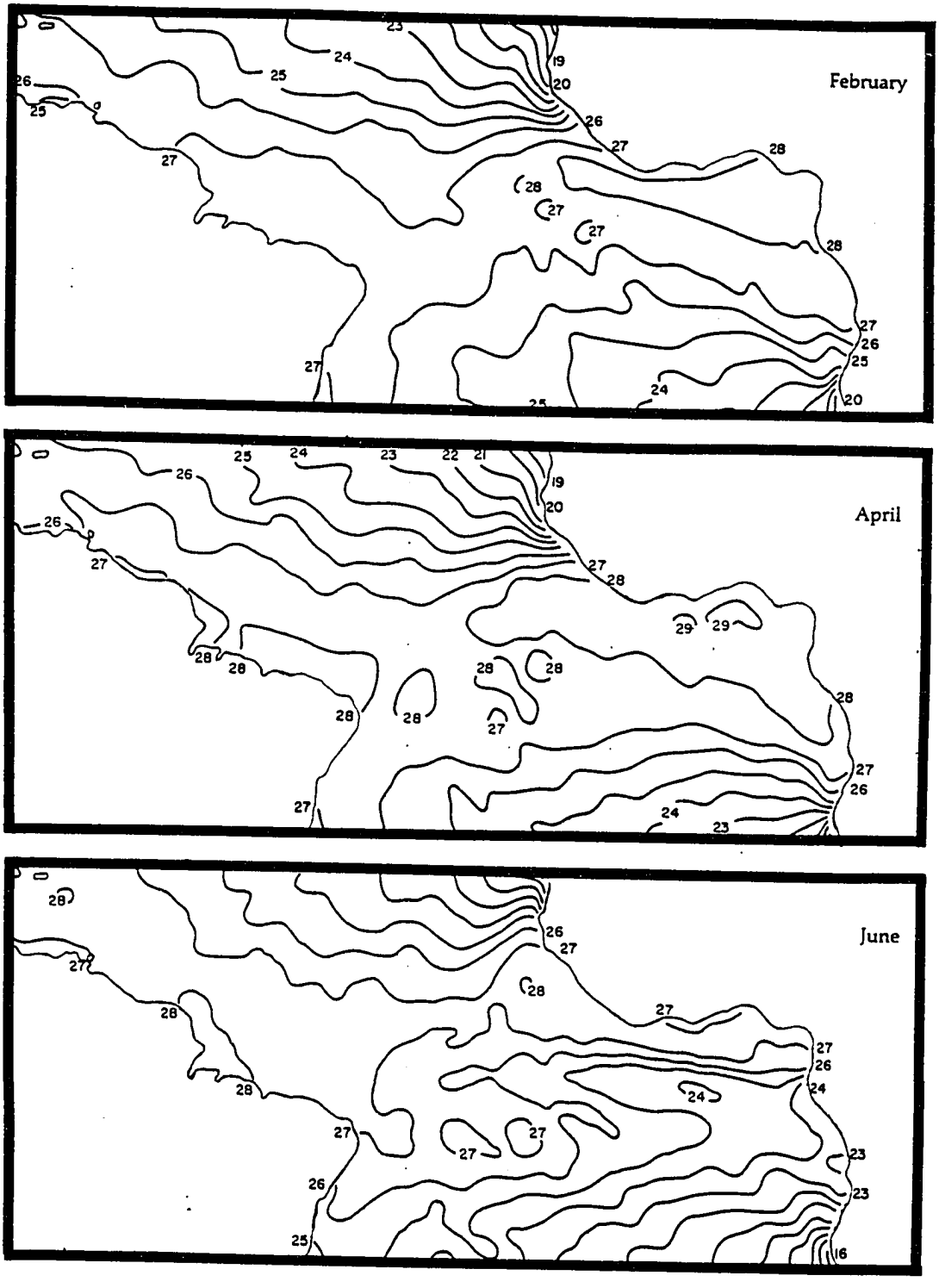

Figure 40: Monthly averaged SST from February to December from Hastenrath and Lamb (1977). The unit is °C

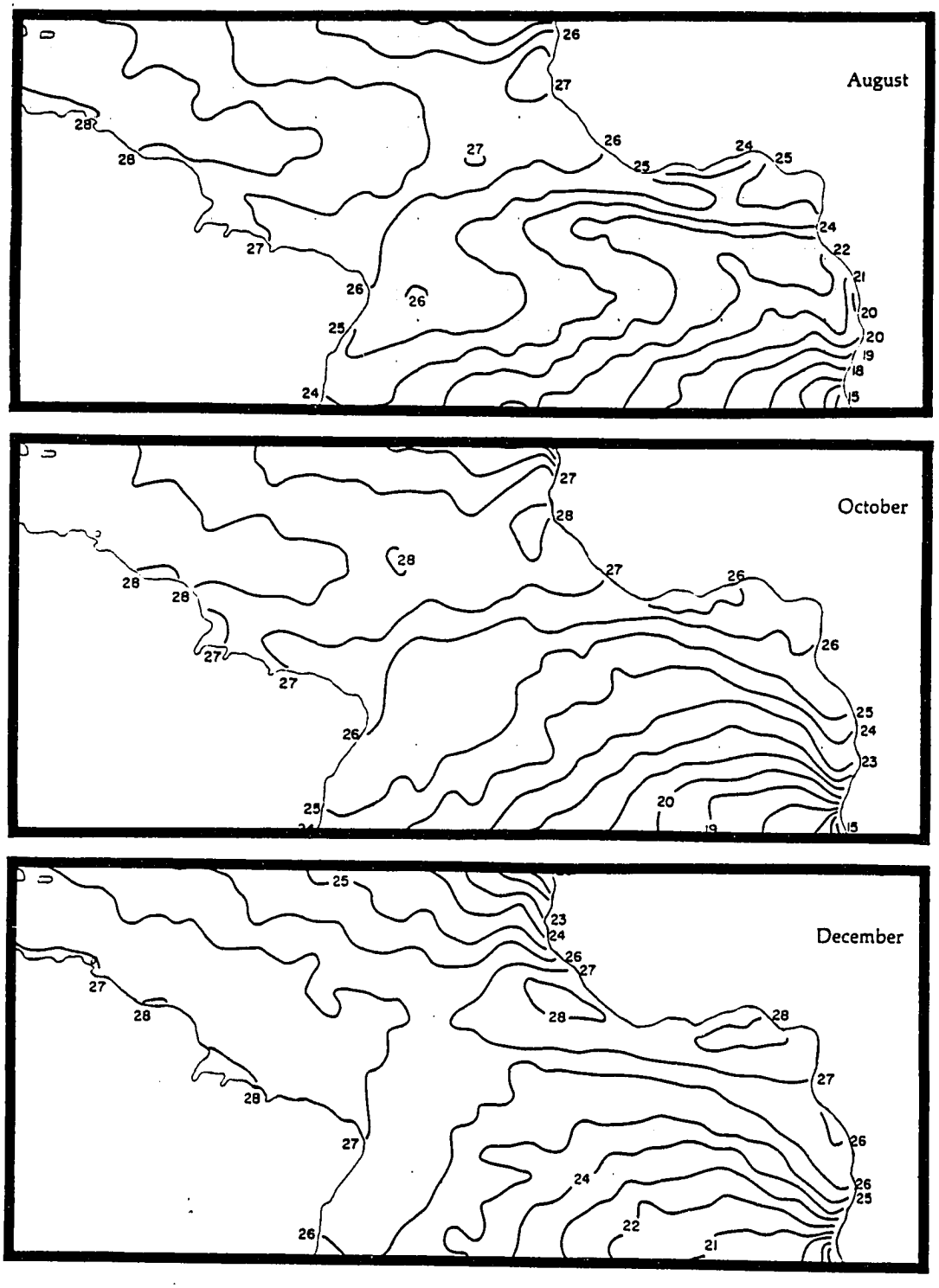

Figure 40: continues.

and diffusion rather than the vertical turbulence. However, isopycnal models may still produce poor results if unrealistic entrainment formulation is used. Therefore, the fact that the simulated SST is an excellent realization of observed SST implies that our basic assumption of the mixed layer entrainment is valid. Accordingly, we may able to conclude that the shear driven entrainment accounts for the major part of the equatorial entrainment cycle.

The observed air-sea heat flux is also taken from Hastenrath and Lamb (1977) as shown in Figure 41. The model-produced heat flux is shown in Figure 42. In general, the two maps show a pattern of the summer hemisphere gaining heat and the winter hemisphere losing heat. The central and eastern part of the equator in both maps are characterized by maximum heat gain in June/August, associated with the intense entrainment (or warm water formation). This is due to the decreased latent heat flux associated with cold SST. Both maps also show small heat loss near the warm water pool in the western part of the equator in August.

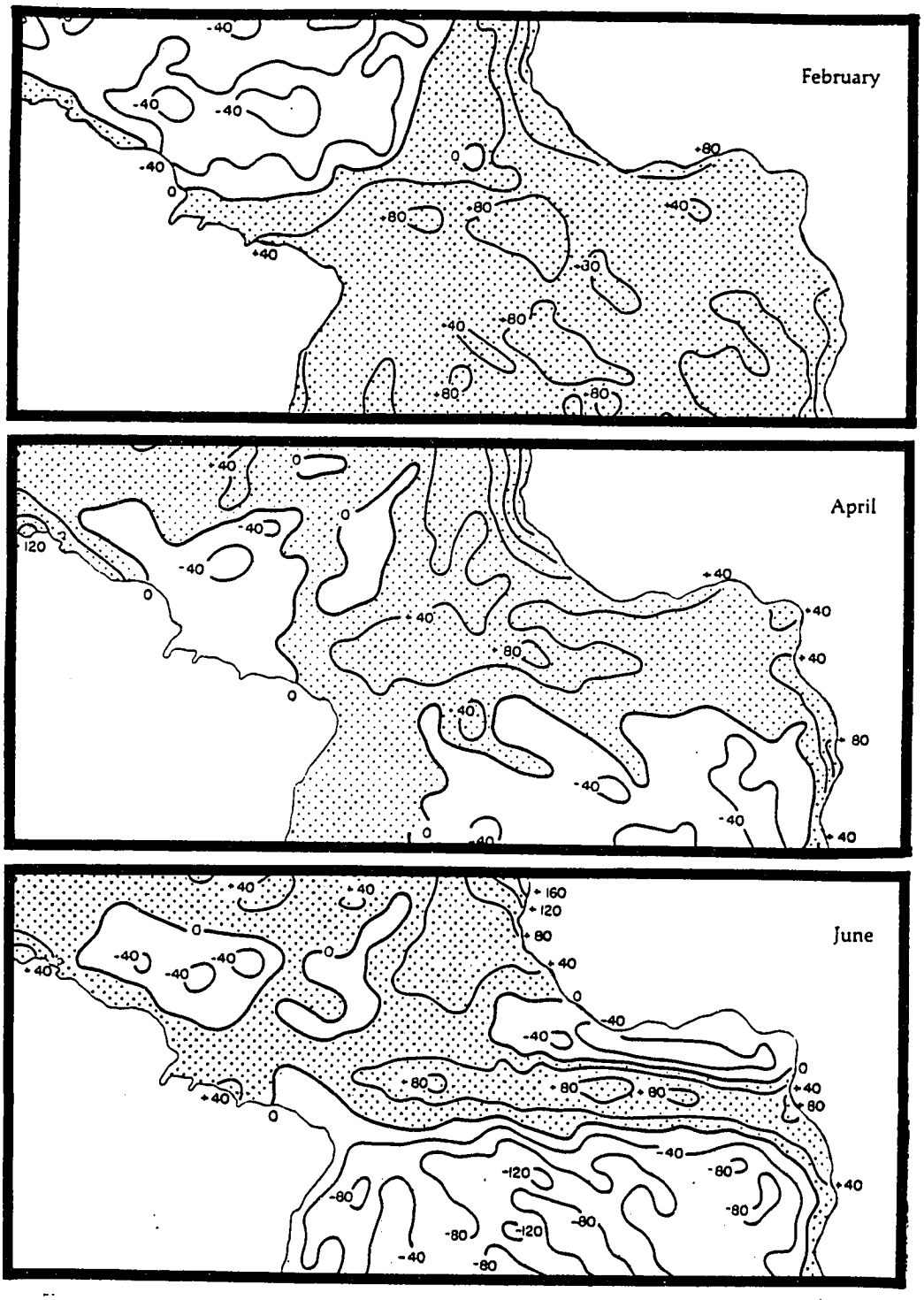

Figure 41: Monthly averaged net oceanic heat gain from February to December from Hastenrath and Lamb (1977). The unit is W/m^2

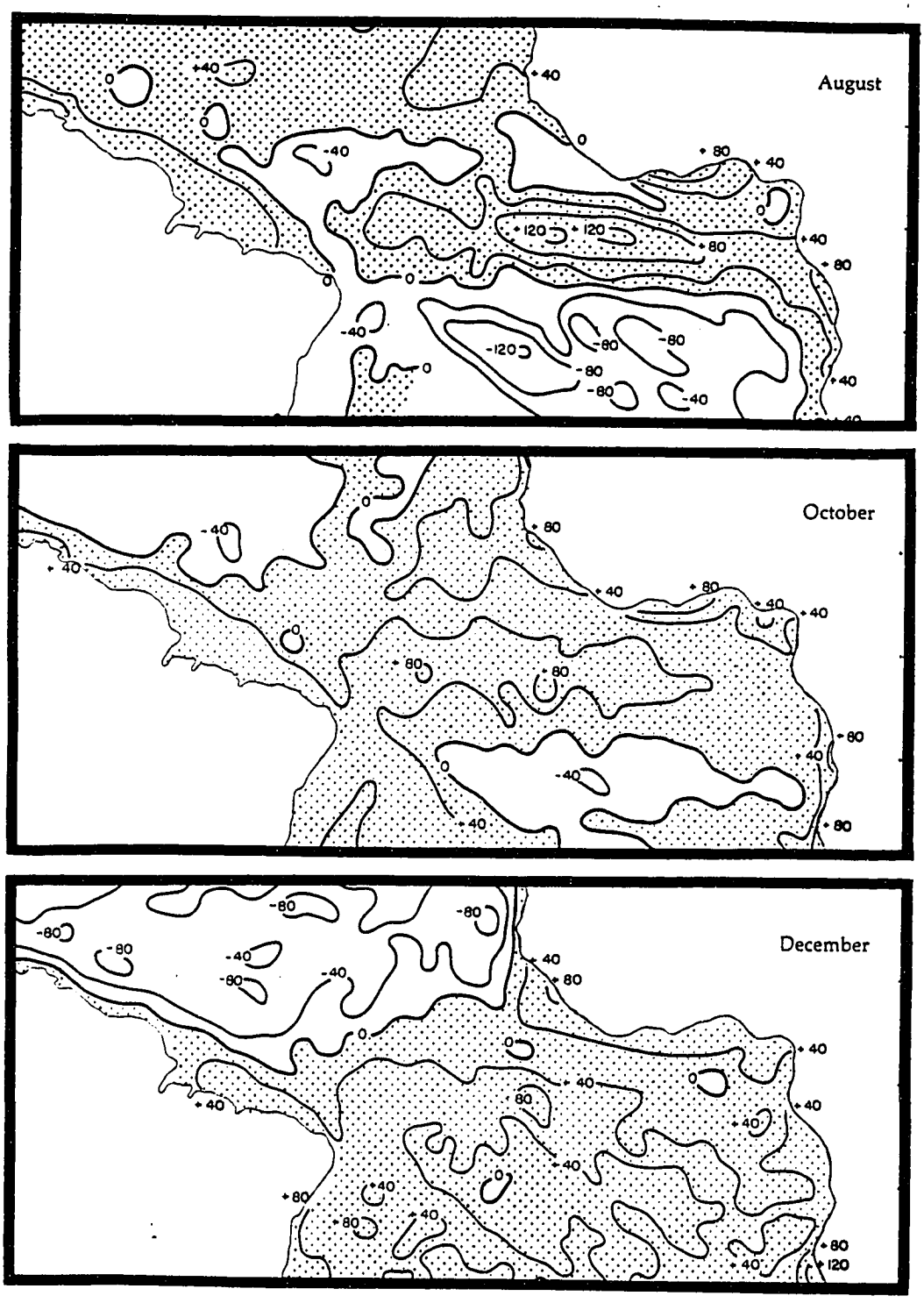

Figure 41: continues.

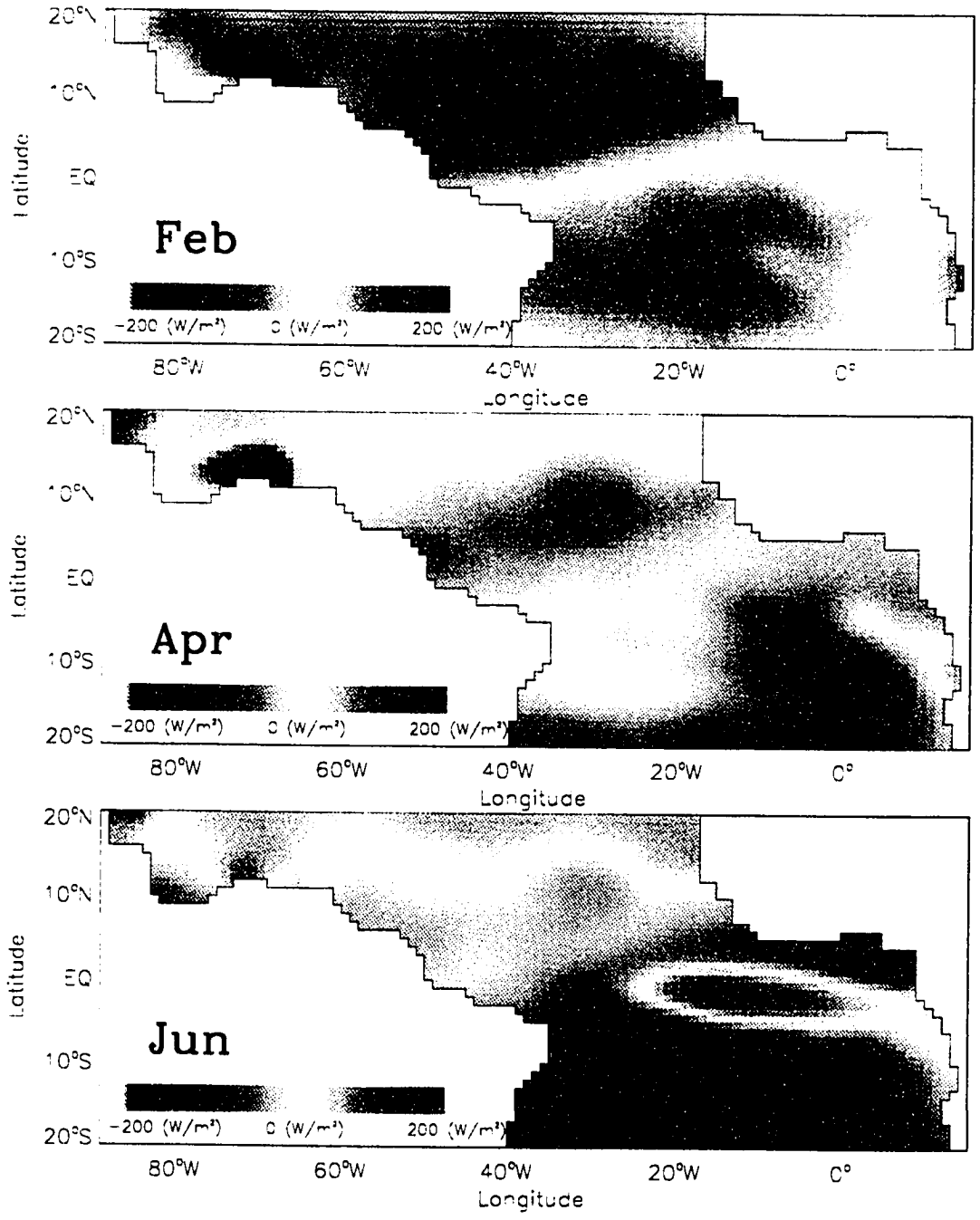

Figure 12: Monthly averaged net oceanic heat gain from February to December inferred from model results. The unit is W/m^2

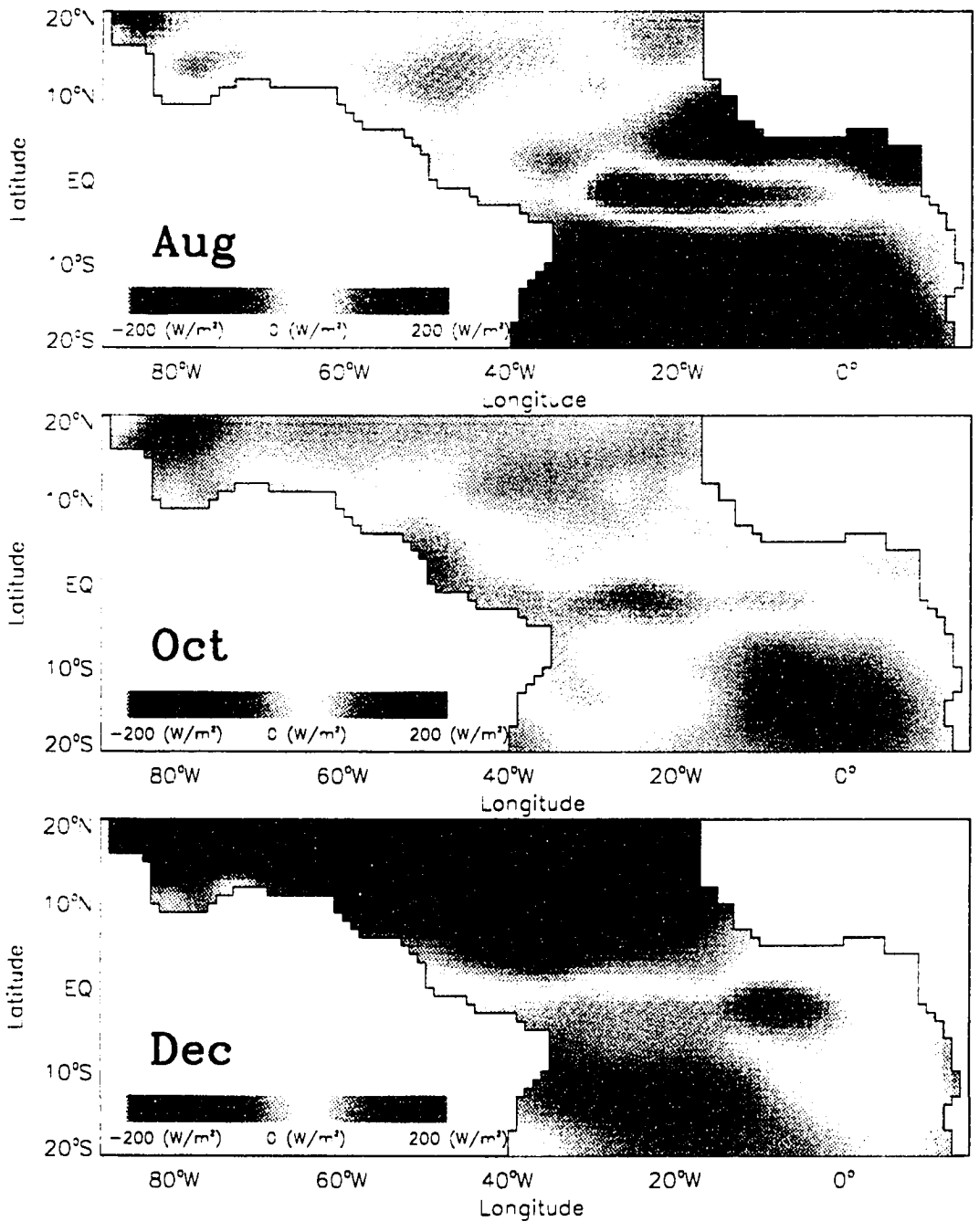

Figure 42: continues.

8 Summary and Conclusions

The primary objective of this work was to study the heat and mass transports in the upper tropical Atlantic Ocean, in response to the ITCZ movement. A simple 2.5 layer model was forced by seasonally varying climatological wind and heat flux fields. The entrainment at the base of mixed layer was scaled by the stress exerted at both top and bottom of the mixed layer, namely the wind stress and the mean shear. Important components of heat transport variability were identified and further quantified. If possible, the seasonal variations of key features were examined and physical explanations were attempted. Available observations of the seasonal cycle in the tropical Atlantic were compared with the model results to validate the physical assumptions of the model and the results.

On an annual average, the northward transport of the tropical WWM is about 11 Sv, with roughly 10 Sv associated with entrainment of upper thermocline water and the other 1 Sv executing a cross-equatorial path continuously from the South Atlantic. Out of total 10 Sv of the needed upper thermocline water, 9 Sv enters the equatorial belt from the South Atlantic. The principal pathways for the cross equatorial transport is found to be (1) the Benguela Current, (2) the SEC, (3) the EUC, (4) the equatorial entrainment, (5) the NBC, (6) the Guiana Current plus the NECC-NEC and (7) Caribbean Current, where (1) and (2) take place in the thermocline layer. The estimate of the transport scale and its pathway are consistent with observations (Roemmich, 1983; Gouriou and Reverdin, 1992).

The seasonal response to the ITCZ movement was most striking in the entrain-

ment rate and the warm water escape rate across the northern edge of the equatorial cell. The entrainment rate was found to be significant only during May/December and ceased completely between January and April. The locally forced equilibrium response between the interfacial shear and the zonal wind stress east of 30°W appears to be responsible for this cycle. The warm water escape rate across 8°N is determined by the three individual mechanisms, namely the NBC, the eastern leg of the cyclonic gyre and the Ekman transport. Further analysis suggests that these three are all strongly related to the seasonal intensification of the NECC: during December/May, the NBC flows continuously northwestward as the Guiana Current. The cyclonic gyre, located below the NEC, transports the warm water mass to the NEC via its eastern leg. The Ekman transport is poleward north of equator during these months. During July/September, on the other hand, the strong negative wind stress curl north of the equator intensifies the NECC, which requires a source of mass at its origin in the west. Therefore, the NBC veers offshore completely and provides the mass, thereby terminating the NBC-Guiana Current system. At the same time, a sudden increase in the wind stress curl causes a deepening (shallowing) of the mixed layer depth south (north) of the NECC, forming a strong potential vorticity front along the northern edge of the NECC. The northward transport via the eastern leg of the cyclonic gyre is therefore limited. In addition, the Ekman transport is slightly southward during these months. As a result of seasonal variations of the two key processes, namely the entrainment and the transport across the northern edge of the equatorial cell, the tropical warm water pool experiences heat storage during May/October and heat escape in November/April.

Of interest were the warm water formation and the SST change in response to the entrainment and the surface heat flux. The warm water formation is a two step process which involves with entrainment of the cold thermocline water followed by heating at the sea surface. On an annual average, heat gain at the sea surface

between 8°S and 8°N is about 0.35 PW and is used exclusively to warm up the cold entrained water. The heat-anomaly fluxes across the zonal boundaries are negligibly small. The seasonal cycle of SST in the equatorial cell consists of a warm season in January/June and a cold season thereafter. The heat budget analysis showed that the cooling of this region from April to August is associated with low solar radiation and intense entrainment cooling. The entrainment cooling is most intense in late-June and decreases thereafter. This reduction of entrainment cooling and increasing atmospheric heating result in net heat gain from mid-August to April. The minimum SST occurs in mid-August when the entrainment cooling and the atmospheric heating cancel each other allowing no diabatic heat storage.

The model results and further analysis suggested that the ITCZ movement is the primary cause of the net northward heat transport observed in the upper tropical Atlantic Ocean. It must be pointed out, however, that there are a couple of other process lacking in the formulation of our model. Broeker (1991) has pointed out that the net cross-equatorial transport in the upper tropical Atlantic is linked to the interbasin scale thermohaline circulation. According to the recent review by Schmitz (1995), there are 14 Sv of net cross-equatorial transport in the upper tropical Atlantic Ocean, with 10 Sv coming from Pacific and the rest 4 Sv from Indian Ocean. Furthermore, Pedlosky (1991), Liu *et al.* (1994) and McCreary and Lu (1994) have suggested that a significant portion of the Equatorial Undercurrent may originate from the subduction of subtropical water. These are basically extratropical processes which can be incorporated into our tropical model as boundary forcings. However, the seasonal variations of these remote forcings are not yet clearly understood. Therefore, for the sake of simplicity, we slowly readjusted the thickness of each layer toward the observed profile at the open boundaries. The application of more improved boundary flux conditions would provide a better understanding of the role of these additional physics.

In general, there was good agreement between observations and the results of the model. This lead us to believe that if required physics are properly implemented, even a simple model can simulate realistic dynamics. Therefore, continuous research on this line of work will help our understanding of the tropical ocean dynamics. A logical extension of the present work may use simplified forcing and model geometry for further investigations of each individual key dynamic features.

9 References

Adamec, D. and J. J. O'Brien. 1978. The seasonal upwelling in the Gulf of Guinea due to remote forcing. J. Phys. Oceanogr., *8*, 1050-1060.

Broecker, W. S., T. H. Peng and M. Stuiver. 1978. An estimate of the upwelling rate in the equatorial Atlantic based on the distribution of bomb radiocarbon. J. Geophys. Res., *83*, 6179-6186.

Broecker, W. S. 1991. The great oceanic conveyor. Oceanography., *4*, 79-82.

Bryan, K. 1969. A numerical method for the study of the circulation of the world ocean. J. Comput. Phys., *4*, 347-376.

———— and L. J. Lewis. 1979. A water mass model of the world ocean. J. Geophys. Res., *84*, 2503-2517.

Bryden, H. L. and M. M. Hall. 1980. Heat transport by currents across $25^{o}N$ latitude by the Atlantic ocean, Science, *207*, 884-885.

Busalacchi, A. J. and J. Picaut. 1983. Seasonal variability from a model of the tropical Atlantic Ocean. J. Phys. Oceanogr., *13*, 1564-1588.

Cane, M. A. 1979. The response of an equatorial ocean to simple wind stress pattern: II. Numerical results. J. Mar. Res. *37*, 253-299.

Cessi, P. 1990. Recirculation and separation of boundary currents. J. Mar. Res. *48*, 1-35.

Chen, D., L. M. Rothstein and A. J. Busalacchi. 1994. A hybrid vertical scheme and its application to tropical ocean model. J. Phys. Oceanogr., *24*, 2156-2179.

Chapman, D. C. 1985. Numerical treatment of cross-shelf open boundaries in a barotropic coastal ocean model. J. Phys. Oceanogr., *15*, 1060-1075.

Christodoulou, G. C. 1986. Interfacial mixing in stratified flows. J. Hydraul. Res. *24*, 77-92.

Condie, S. A. 1991. Separation and recirculation of the North Brazil Current. J. Mar. Res., *49*, 1-19.

Csanady G. T. 1984. Warm water mass formation. J. Phys. Oceanogr., *14*, 264-275.

———— 1985. A zero potential vorticity model of the North Brazilian Coastal Current. J. Mar. Res. *43*, 553-579.

———— 1987. What controls the rate of equatorial warm water mass formation? J. Mar. Res. *45*, 513-532.

———— 1990. Retroflection and leakage in the North Brazil Current: Critical point analysis. J. Mar. Res. *48*, 701-728.

———— 1995. Equatorial upwelling under southeasterly winds. (unpubl. ms.).

Cushman-Roisin, B. 1994. Introduction to geophysical fluid dynamics. Prentice Hall., 320pp.

Didden, N. and F. Schott. 1993. Eddies in the North Brazil Current retroflection region observed by Geosat altimetry. J. Geophys. Res., *98*, 20121-20131.

Esbensen, S. K. and Y. Kushnir. 1981. The heat budget of the global ocean: An atlas based on estimate from surface marine observations. Climate Research Institute Report 29, Oregon State University, Corvallis, OR, 27pp.

Fernando, H. J. S. 1991. Turbulent mixing in stratified fluid. Ann. Rev. Fluid Mech., *23*, 455-493.

Flagg, C. N, R. N. Gordon and S. McDowell. 1986. Hydrographic and current observations on the continental slope and shelf of the western Equatorial Atlantic. J. Phys. Oceanogr., *16*, 1412 -1429.

Fleagle R. G. and A. B. Businger. 1980. An Introduction to Atmospheric Physics. Academic Press., New York., 432pp.

Fu, L. L. 1981. The general circulation and meridional heat transport of the subtropical south Atlantic determined by inverse methods. J. Phys. Oceanogr., *11*, 1171-1193.

Garzoli, S. L. and E. J. Katz. 1983. The forced annual reversal of the Atlantic North Equatorial Countercurrent. J. Phys. Oceanogr., *19*, 2082-2090.

Gent, P. R. and M. A. Cane. 1989. A reduced gravity, primitive equation model of

the upper equatorial ocean. J. Comput. Phys. *81*, 444-480.

Gent, P. R. 1991. The heat budget of the TOGA-COARE domain in an ocean model. J. Geophys. Res., *96*, 3323-3330.

Gill A. E. 1982. Atmosphere-Ocean dynamics. Academic Press., 662pp.

Gouriou, Y. and G. Reverdin. 1992. Isopycnal and diapycnal circulation of the upper equatorial Atlantic ocean in 1983-1984. J. Geophys. Res., *97*, 3543-3572.

Grammeltvedt, A. 1969. A survey of finite-difference schemes for the primitive equations for a barotropic fluid. Mon. Wea. Rev., *97*, 384-404.

Haney R. L. 1971. Surface thermal boundary condition for ocean circulation models. J. Phys. Oceanogr., *1*, 241-248.

Hastenrath S. and P. J. Lamb. 1977. Climatic atlas of the tropical Atlantic and eastern Pacific oceans. University of Wisconsin Press., Madison, 97 charts.

Hastenrath, S. 1980. Heat budget of tropical ocean and atmosphere. J. Phys. Oceanogr., *10*, 159-170.

———— 1982. On meridional heat transports in the world ocean. J. Phys. Oceanogr., *12*, 922-927.

———— and J. Merle. 1985. The annual march of heat storage and export in the tropical Atlantic ocean. J. Phys. Oceanogr., *16*, 694-708.

Hellerman, S. 1980. Charts of the variability of the wind stress over the tropical Atlantic. Deep-Sea Res., *26*, GATE suppl.2, 63-75.

———— and M. Rosenstein. 1983. Normal monthly wind stress over the world ocean with error estimates. J. Phys. Oceanogr., *13*, 1093-1104.

Hensen, W. 1962. Hydrodynamic methods applied to oceanographic problems. Proc. Symp. Mathem. Hydrodyn. Methods for Phys. Oceanogr., Inst. Meeresjunde Univ. Hamburg, 25-34.

Holland, W. R. and L. B. Lin. 1975. On the generation of mesoscale eddies and their contribution to the oceanic general circulation. I. A preliminary numerical experiment. J. Phys. Oceanogr., *5*, 642-657.

Houghton, R. W. 1976. Circulation and hydrographie structure over the Guiana continental shelf during the 1974 upwelling. J. Phys. Oceanogr., *6*, 909-924.

Hsiung, J. 1985. Estimates global oceanic meridional heat transport. J. Phys. Oceanogr., *15*, 1405-1413.

———— 1989. The annual cycle of oceanic heat storage and oceanic meridional heat transport. Q. J. R. Meteorol. Soc., *115*, 1-28.

Jensen, R. G. 1990. A numerical study of the seasonal variability of the Somali current. Ph.D. dissertation, Florida State University, Tallahassee, 118pp.

Johns, W. E., T. N. Lee, F. Schott, R. J. Zantopp and R. H. Evans. 1990. The North Brazil Current retroflection: Seasonal structure and eddy variability. J. Geophys. Res., *95*, 22103-22120.

Jones, I. S. F. and P. J. Mulhearn. 1983. The influence of external turbulence on sheared interface. Geophys. Astrophys. Fluid Dyn., *24*, 49-62.

Kato, H. and O. M. Phillips. 1969. On the penetration of a turbulent layer into stratified fluid. J. Fluid Mech., *79*, 645-665.

Katz, E. J and Collaborators. 1977. Zonal pressure gradient along the equatorial Atlantic. J. Mar. Res., *35*, 293-307.

Katz, E. J and S. L. Garzoli. 1984. Thermocline displacement across the Atlantic North Equatorial Countercurrent during 1983. Geophys. Res. Lett., *11*, 737-740.

Kim, J. W. 1976. A generalized bulk model of the oceanic mixed layer. J. Phys. Oceanogr., *6*, 686-695.

Koop, G. and F. K. Browand. 1979. Instability and turbulence in stratified fluids with shear. J. Fluid Mech., *93*, 125-159.

Killworth, P. D. 1984. A note on smoothing techniques for leapfrog time -integration schemes. Ocean Modelling, *60*, 5-8.

Kraus E. B. and J. S. Turner. 1967. A one-dimensional model of the seasonal thermocline. II. The general theory and its consequences. Tellus, *XIX*, 98-105.

Lamb, P. J. 1981. Estimate of annual variation of Atlantic ocean heat transport. Nature, *290*, 766-768.

———— 1984. On the mixed-layer climatology of the north and tropical Atlantic. Tellus, *36A*, 292-305.

Levitus, S. 1982. Climatological atlas of the world ocean. NOAA prof. Pap., *13*, U.S.

Government Printing Office, Washington, D.C., 173pp

———— 1984. Annual cycle of temerature and heat storage in the world ocean. J. Phys. Oceanogr., *14*, 727-746.

Lilly, D. K. 1965. On the computational stability of numerical solutions of time-dependent non-linear geophysical fluid dynamic problems. Mon. Wea. Rev., *93*, 76-84.

Liu, Z., S. G. H. Philander and R. C. Pacanowski. 1994. A GCM study of tropical-subtropical upper ocean water exchange. J. Phys. Oceanogr., *24*, 2606-2623.

Merle, J. 1980. Seasonal heat budget in the equatorial Atlantic ocean. J. Phys. Oceanogr., *10*, 464-469.

———— and S. Arnault. 1985. Seasonal variability of the surface dynamic topography in the tropical Atlantic Ocean. J. Mar. Res., *43*, 267-288.

Metcalf, W. G. and M. C. Stalcup. 1967. Origin of the Atlantic equatorial undercurrent. J. Geophys. Res., *72*, 4959-4975.

McCreary, J. P. and P. K. Kundu. 1988. A numerical investigation of the Somali Current during the southwest Monsoon. J. Mar. Res., *46*, 25-58.

McCreary, J. P. and Z. Yu. 1992. Equatorial dynamics in a 2.5 layer model. Prog. Oceanogr., *29*, 61-132.

McCreary, J. P. , P. K. Kundu and R. L. Molinari. 1993. A numerical investigation of dynamics, thermodynamics and mixed-layer processes in the Indian ocean. Prog. Oceanogr., *31*, 181-244.

McCreary, J. P. and P. Lu. 1994. On the interration between the subtropical and equatorial ocean circulations: The subtropical cell. J. Phys. Oceanogr., *24*, 466-497.

Moore, D. W., P. Hisard, J. P. McCreary, J. Merle, J. J. O'Brien, J. Picaut, J. M. Verstraete and C. Wunch. 1978. Equatorial Adjustment in the eastern Atlantic. Geophys. Res. Lett., *5*, 637-640.

Narimousa, S. and H. J. S. Fernando. 1987. On sheared density interface of an entraining stratified fluid. J. Fluid Mech., *174*, 1-22.

Niiler, P. and J. Stevenson. 1982. The heat budget of tropical ocean warm-water pools. J. Mar. Res., *40*, suppl., 465-480.

Orlanski, I. 1976. A simple boundary condition for unbounded hyperbolic flow. J. Comput. Phys., *21*, 251-269.

Pacanowski, R. C. and S. G. H. Philander. 1981. Parameterization of vertical mixing in numerical models of tropical oceans. J. Phys. Oceanogr., *11*, 1443-1451.

Parsons, A. T. 1969. A two layer model of Gulf Stream separation. J. Fluid Mech., *39*, 511-528.

Pedlosky, J. 1991. The link between western boundary current and equatorial undercurrent. J. Phys. Oceanogr., *21*, 1553-1558.

Philander, S. G. H. and R. C. Pacanowski. 1986. A model of the seasonal cycle in the tropical Atlantic ocean. J. Geophys. Res., *91*, 14192-14206.

Picaut, T. 1983. Propagation of the seasonal upwelling in the eastern Equatorial Atlantic. J. Phys. Oceanogr., *13*, 18-37.

Pollard, R. T., P. B. Rhine and R. O. R. Y. Thompson. 1973. The deepening of the wind mixed layer. Geophys. Fluid Dyn., *3*, 381-404.

Price, J. F. 1979. On the scaling of stress-driven entrainment experiments. J. Fluid Mech., *90*, 509-529.

Price, J. F. 1981. Upper ocean response to a Hurricane. J. Phys. Oceanogr., *11*, 153-175.

Reverdin, G. 1985. Heat budget of the tropical Atlantic ocean - seasonal upwelling. Deep-Sea Res., *32*, 363-368.

Richardson, P. L. and T. K. McKee. 1984. Average seasonal variation of the Atlantic Equatorial Currents from historical ship drifts. J. Phys. Oceanogr, *14*, 1226-1238.

Richardson, P. L. and D. Walsh. 1986. Mapping climatological seasonal variations of surface currents in the Tropical Atlantic using ship drifts. J. Geophys. Res., *91*, 10537-10550.

Richardson, P. L., G. E. Hufford, R. Limeburner and W. S. Brown. 1994. North Brazil Current retroflection eddies. J. Geophys. Res., *99*, 5081-5093.

Roemmich, D. 1980. Estimation of meridional heat flux in the north Atlantic by inverse methods. J. Phys. Oceanogr, *10*, 1972-1983.

——— 1983. The balance of geostrophic and Ekman transports in tropical Atlantic ocean. J. Phys. Oceanogr., *13*, 1534-1539.

Sarmiento, J. L. 1986. On the north and tropical Atlantic heat balance. J. Geophys. Res., *91*, 11677-11689.

Schmitz, W. J. and P. L. Richardson. 1991. On the source of the Florida current. Deep-Sea Res., *38*, 389-409.

Schmitz, W. J. 1995. On the interbasin-scale thermohaline circulation. Oceanography., *33*, 151-173.

Schopf P. S. 1980. The role of Ekman flow and planetary waves in the oceanic cross-equatorial heat transport. J. Phys. Oceanogr., *10*, 330-341.

——— and M. A. Cane. 1983. On equatorial dynamics, mixed layer physics and sea surface temperature. J. Phys. Oceanogr., *13*, 917-935.

Schott, F. A. and C. W. Boning. 1991. The WOCE model in the western equatorial Atlantic: upper layer circulation J. Geophys. Res., *96*, 6993-7004.

Servain, J., J. Picaut and J. Merle. 1982. Evidence of remote forcing in the equatorial Atlantic Ocean. J. Phys. Oceanogr., *2*, 457-463.

Servain, J., D. M. Legler. 1986. Empirical orthogonal function analysis of tropical Atlantic sea surface temperature and wind stress: 1964-1979. J. Geophys. Res., *91*, 14181-14191.

Shuman, F. G. 1957. Numerical methods in weather prediction: II-smoothing and filtering. Mon. Wea. Rev., *85*, 357-361.

Stommel, H. 1968. The Gulf Stream: A physical and dynamical description. University of California Press, California, 248pp.

Sverdrup, H. L. 1947. Wind-driven currents in a baroclinic ocean: with application to the equatorial currents of the eastern Pacific. Proc. Nat. Acad. Wash., *33*, 318-326.

Thorpe, S. A. 1987. Transitional phenomena and development of turbulence in stratified fluids: A review. J. Geophys. Res., *92*, 5231-5248.

Veronis, G. 1981. Dynamics of large scale ocean circulation in Evolution of Physical Oceanography, B. A. Warren and C. Wunch, eds., MIT press, 140-183.

Voituriez, B. 1981. The equatorial upwelling in the eastern Atlanic Ocean. Report of the final meeting of SCOR WG 47. Nova University Press., 229-247.

——— and A. Herbland. 1979. The use of the salinity maximum of the equatorial undercurrent for estimating nutrient enrichment and primary production in the Gulf of Guinea. Deep-Sea Res., *26*, 77-83.

Wunsch, C. 1978. The north Atlantic circulation west of $50°W$ determined by inverse methods. Rev. Geophys. Space Phys., *16*, 583-620.

——— 1980. Meridional heat flux of the North Atlantic Ocean. Proc. Natl. Acad. Sci., U.S.A., *77*, 5043-5047.

——— 1984. An estimate of the upwelling rate in the equatorial Atlantic based on the distribution of bomb radiocarbon and quasi-geostrophic dynamics. J. Geophys. Res., *89*, 7977-7988.

Wyrtki, K. 1981. An estimate of equatorial upwelling in the Pacific. J. Phys. Oceanogr., *11*, 12205-1214.

Autobiograhical Statement

Sang-Ki Lee

Personal Data

I was born on August 17, 1968, in Seoul, Korea. My parents are Cheol-Soo Lee and Hae-Ok Yang and I have one brother, Sang-Heon. I am a citizen of the Republic of Korea.

Education

M.Sc. Oceanography, December 1993, Old Dominion University, Norfolk, Va, USA
B.Sc. Oceanography, February 1991, Inha University, Incheon, Korea

Memberships

American Meteorological Society
American Geophysical Union

Publications

Lee, S. K. and G. T. Csanady. 1994. Instability waves in the Gulf Stream front and its thermocline layer. J. Mar. Res., *52*, 837-863.
Lee, S. K. 1993. Instability waves in the Gulf Stream front and its thermocline layer. M.Sc. Thesis, Old Dominion University, 64pp.